5-14-2015

Study the Mechanism of the Prompt Emission of Gamma-Ray Bursts

Wei Deng
University of Nevada, Las Vegas

STUDY THE MECHANISM OF THE PROMPT EMISSION OF GAMMA-RAY BURSTS

by

Wei Deng

Bachelor of Science
Nanjing University
2007

Master of Science
Nanjing University
2010

A dissertation submitted in partial fulfillment
of the requirements for the

Doctor of Philosophy - Astronomy

Department of Physics and Astronomy
College of Science
The Graduate College

University of Nevada, Las Vegas
August 2015

UNLV | GRADUATE COLLEGE

Dissertation Approval

The Graduate College
The University of Nevada, Las Vegas

May 14, 2015

This dissertation prepared by

Wei Deng

entitled

Study the Mechanism of the Prompt Emission of Gamma-Ray Bursts

is approved in partial fulfillment of the requirements for the degree of

Doctor of Philosophy – Astronomy
Department of Physics and Astronomy

Bing Zhang, Ph.D.
Examination Committee Chair

Kathryn Hausbeck Korgan, Ph.D.
Graduate College Interim Dean

Daniel Proga, Ph.D.
Examination Committee Member

Stephen Lepp, Ph.D.
Examination Committee Member

Pengtao Sun, Ph.D.
Graduate College Faculty Representative

ABSTRACT

Study the Mechanism of the Prompt Emission of Gamma-Ray Bursts

by

Wei Deng

Dr. Bing Zhang, Examination Committee Chair
Professor of Physics
University of Nevada, Las Vegas

The prompt emission of Gamma-Ray Bursts (GRBs) has been detected over 40 years, but the mechanism of the prompt emission is still a mystery. The problem can be summarized as several debatable questions: What is the energy composition of the jets/outflows? What is the energy dissipation mechanism? How are the particles accelerated during the energy dissipation process? What is the radiation mechanism to produce the observed prompt emission? In order to solve these problems, several theoretical models have been proposed, including the classical "internal shock (IS)" model, the "dissipative photosphere" model, the "magnetic dissipation" model, and so on. Different models have different strengths and weaknesses. Observations also show a diversity of GRB emission properties, and different GRBs may favor different models. Statistically, a small fraction of GRBs, show an obvious feature of the thermal origin; in contrast, the majority of GRBs, with the so called "Band-function" spectra, favor the non-thermal origin. A promising magnetic dissipation model proposed by Zhang & Yan (2011) dubbed "the Internal-Collision-induced MAgnetic Reconnection and Turbulence (ICMART)" model shows great potential to overcome the weaknesses in other models and interpret the observations of the majority of GRBs. However, since some important ingredients of this model are still of a speculative nature, the follow-up detailed numerical simulation works are definitely needed to give a solid footing to this model.

This dissertation includes two parts. The first part (Chapter 2) is related to

the photosphere model of prompt emission. We performed a detailed study of the photosphere emission spectrum by progressively introducing several physical ingredients previously not fully incorporated, including the probability distribution of the location of a dynamically evolving photosphere, superposition of emission from an equal-arrival-time "volume" in a continuous wind, the evolution of optical depth of a wind with finite but evolving outer boundary, as well as the effect of different top-hat wind luminosity(L_w) profiles. We found that the low-energy spectrum below the peak energy(E_p) can only be modified to $F_\nu \sim \nu^{1.5}$ ($\alpha \sim +0.5$) except the steep decaying phase of the pulse of lightcurve. This spectrum is much harder than the typical Band-function ($\alpha \sim -1$) as observed. In addition, we found that the photosphere model can not interpret the observed "hard-to-soft" pattern of the peak energy (E_p) evolution.

The second part (Chapter 3) presents a global special relativistic MHD simulations based on the ICAMRT scenario, which discovered significant electromagnetic field (EMF) energy dissipation with the efficiency around 35% due to the collision-induced magnetic reconnection. The reconnection outflows in our simulations can potentially form multi-orientation relativistic mini-jets as needed for several analytical models. We also found a linear relationship between the σ values before and after the major EMF energy dissipation process. This work gives good support to the ICMART model and can be also applied to other relevant astrophysical systems, such as the reconnection triggered mini-jets model for AGNs.

ACKNOWLEDGMENTS

At the beginning, I would like to express my sincere thanks to all the people who helped me a lot in my working, studying, and living in these years.

First of all, I would like to express my sincerely appreciation from the bottom of my heart for the tons of help from my Ph.D. advisor, Prof. Bing Zhang. In terms of research, his great enthusiasm towards the science deeply influenced me and made me not only treat the study as a mission but also enjoy the fulfillment of research. In addition, his excellent insight towards the cutting edge of science gave me excellent guide to spend the limited time on the most important unsolved problems, which provided me a leading start point of my academic career. Furthermore, his great patience to all of my questions made me build up a solid base of my research career. Besides academic life, Bing also gave me strong support and concern for my daily life. He frequently organized group gatherings to make us relax after intense study and work. The amazing singing and playing of the guitar and piano from him and his family members deeply impressed me. All in all, it is my great honor to be a student of Bing! And as Newton said, "If I can see farther, it is because I stand on the shoulder of giants!"

Another special acknowledgment definitely goes to my host/advisor in Los Alamos National Laboratory (LANL), Dr. Hui Li. He gave me an irreplaceable opportunity to start my numerical simulation career, which deeply interests me. With his help, I can study science like a director directing a movie. He also influenced me on scientific methodology. He showed me how to consider a scientific problem from the first

principles and quickly get to the key of the problem. Besides research, he also gave me extra support in both daily life and my financial situation to make my visit to LANL smooth and comfortable. It is really a great experience here!

Our collaborator, Dr. Shengtai, Li at LANL, is another important mentor to help me to use the code from the first sentence of the command. I still remember my tons of emails/visits blasted to him at the beginning months. I am so grateful for Shengtai's help!

I would also like to express my sincere thanks to Dr. Ken-Ichi Nishikawa for his kind instructions for the usage of their Particle-In-Cell simulation code.

In addition, I take this opportunity to express my acknowledgments to many people in the Department of Physics & Astronomy of UNLV. I would like to thank Dr. Daniel Proga, Dr. Kentaro Nagamine, Dr. George Rhee, Dr. Stephen Lepp, Dr. Bernard Zygelman, Dr. Lon Spight and Dr. Thomas Hurst for their excellent teaching, which enhanced my knowledge from the diverse areas of astronomy and physics. I would also like to thank Ms. Gail Michel-Parsons, Ms. Natasa Korceba, Ms. Cara Loomis, Ms. Simonne Purdy, Mr. Jay Nietling and Dr. Victor H.S. Kwong for their technical assistance and kind help.

My thanks also go to all my research group members and classmates in both UNLV and LANL. I sincerely thank Dr. Xue-Feng Wu, Dr. Bin-Bin Zhang, Dr. He Gao, Dr. Hou-Jun Lv, Dr. Fan Guo and Dr. Xiao-Yue Guan for their very helpful discussion and suggestions. I also thank Dr. En-Wei Liang, Dr. Wei-Hua Lei, Dr. Qiang Yuan, Dr. Francisco Virgili, Dr. Amanda Maxham, Dr. Z. Lucas

Uhm, Dr. Massimiliano De Pasquale, Dr. Haocheng Zhang, Dr. Xiang-Gao Wang, Dr. Bo Zhang, Dr. Yi-Hsin Liu, Ye Li, Shuang-Xi Yi, Robert Gex, Tesla Birnbaum, Timothy Water, Robert Thompson, Keita Todoroki, Gabriel Gobeli and Sandamali Weerasooriya for their useful discussion and help.

I would like to sincerely thank Dr. Daniel Proga, Dr. Stephen Lepp, Dr. Pengtao Sun for serving in my committee and their great suggestions and discussion for my dissertation.

Furthermore, I express my sincere appreciation to my former advisor, Dr. Yongfeng Huang, who gave me the first opportunity to study our amazing universe!

I also take this opportunity to express my sincere appreciation to my wife, Yuting Shi, who unwaveringly follows me, and wholeheartedly takes care of our little cute boy and the home business all the time to support me to concentrate on my work!

In addition, I sincerely appreciate my parents who wholeheartedly care and encourage me from the first day of my birth!

TABLE OF CONTENTS

LIST OF TABLES

LIST OF FIGURES

CHAPTER 1

INTRODUCTION

Gamma-Ray Bursts (GRBs), which are the most energetic explosive events in our universe, were first detected by the Vela satellites in the late 1960s (Klebesadel et al., 1973). Generally speaking, the emission of GRBs can be separated as early short-lived prompt emission phase and the following long-lived afterglow emission phase. The multi-wavelength afterglow can be well interpreted as the emission from the relativistic external shock produced by the interaction between the ejecta of GRBs and the surrounding interstellar medium (Blandford and McKee, 1976; Mészáros and Rees, 1997a; Costa et al., 1997; van Paradijs et al., 1997; Frail et al., 1997; Sari et al., 1998; Gao et al., 2013b). However, the physical mechanism of prompt emission is still subject to debate, even though it was detected tens of years earlier than the afterglow emission. The major work of my dissertation is motivated by several unsolved questions of GRB prompt emission: What is the energy composition of the jets/outflows? What is the energy dissipation mechanism? How are the particles accelerated during the energy dissipation process? What is the radiation mechanism to produce the observed radiation features? In the following, I will first introduce the main observational features of GRB prompt emission, and then summarize the various prompt emission models along with their strengths and weaknesses.

Part of this Chapter is referenced to the textbook (Cambridge University Press in preparation) being written by Bing Zhang (Zhang, 2015) and the review articles by Kumar & Zhang (2014); Zhang (2014).

1.1 Main Observational Features of GRB Prompt Emission

1.1.1 Lightcurve Properties

- Duration:

The traditional way to define the duration of GRB prompt emission is called

T_{90} which is the duration from the 5% to the 95% of the total fluence above the background level received by the detectors in the sub-MeV γ-ray energy band[1]. We need to notice that, based on this definition, the duration not only depends on the bursts but also depends on the detectors, since different detectors have different sensitivities corresponding to different background levels. For the same burst, a more sensitive detector would measure a longer duration. Another effect from the detector is that different instruments have more or less different band-passes in the sub-MeV energy band. This will also affect the observed T_{90} due to the energy dependent fluence level.

The distribution of T_{90} has two distinct peaks at 0.3 s and 30 s respectively, and there is a separation trough around 2 s between these two peaks (Fig.1) (Kouveliotou, C.). Based on this separation, the bursts are classified as two groups: short GRBs (T_{90} smaller than 2 s) and long GRBs (T_{90} larger than 2 s).

- Shape:

  The lightcurves of GRBs are very irregular, from extreme millisecond variability to relatively smooth and simple temporal evolution; from single pulse to multiple pulses (Fishman and Meegan, 1995); from continuous emission to significantly distinct emission episodes with long quiescent separations between them. Figure 2 gives some example lightcurves of GRBs.

- Period properties:

  The traditional power density spectrum (PDS) analyses for individual bursts did not show any periodicity (Beloborodov et al., 1998; Beloborodov, 2000; Guidorzi et al., 2012), while the average PDS for many GRBs showed a power

[1]Another less frequently used definition of the duration is called T_{50} which is the duration between the 25% and the 75% of the total fluence above the background level received in the sub-MeV energy band.

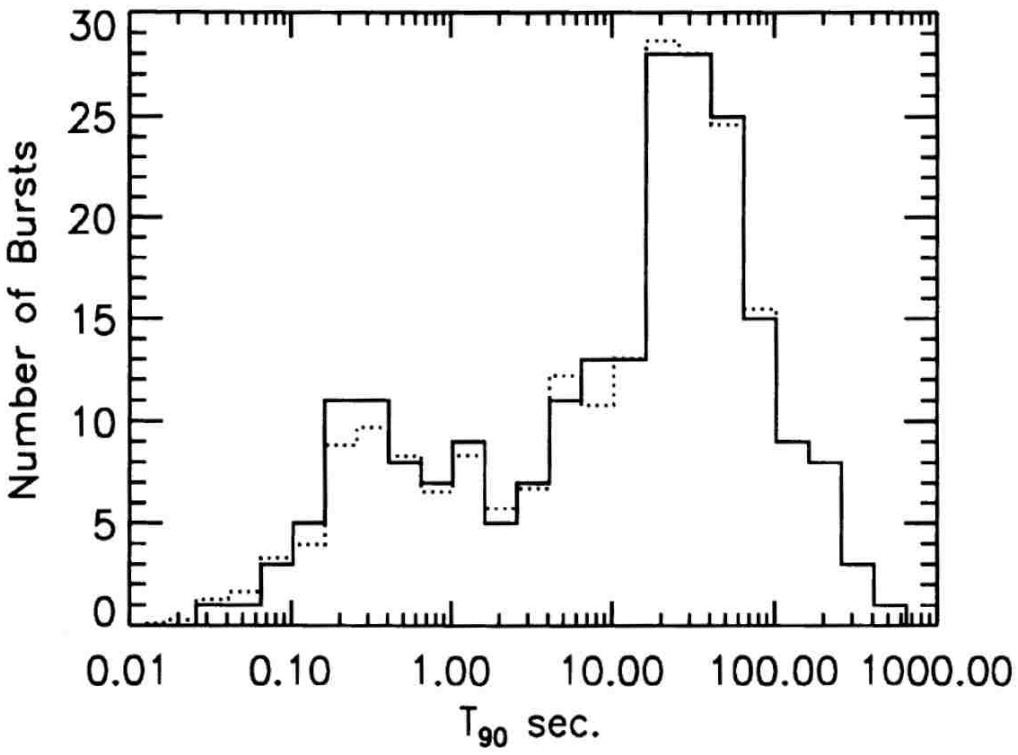

Figure 1 . The statistics of the T_{90} distribution of 222 BATSE GRBs (from Kouveliotou, C., Meegan, C. A., Fishman, G. J., Bhat, N. P., Briggs, M. S., Koshut, T. M., Paciesas, W. S., Pendleton, G. N., Aug. 1993. Identification of two classes of gamma-ray bursts. ApJ413, L101–L104) (© AAS. Reproduced with permission).

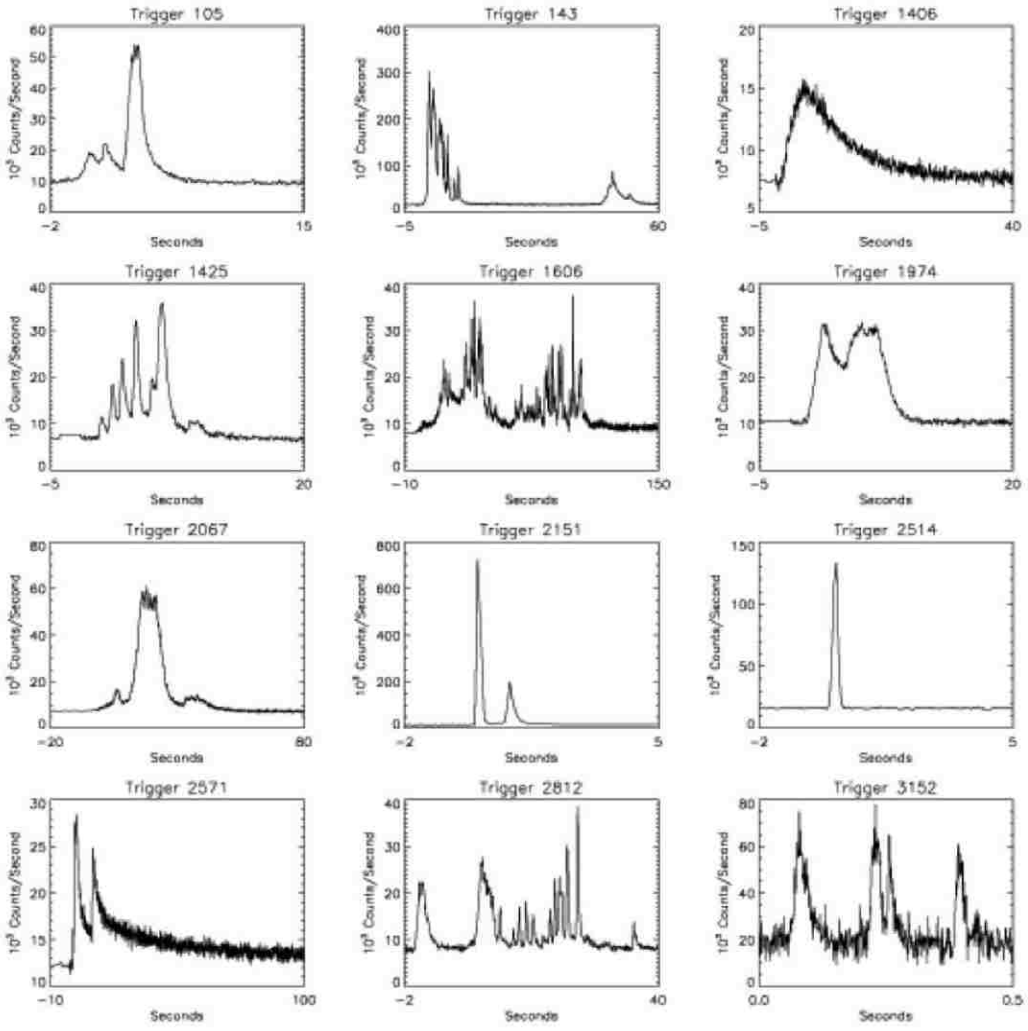

Figure 2 . Some example lightcurves of GRBs (from Fishman, G. J., Meegan, C. A., 1995. Gamma-Ray Bursts. Annual Review of Astronomy and Astrophysics33, 415–458) (reprinted with permission from AAAS).

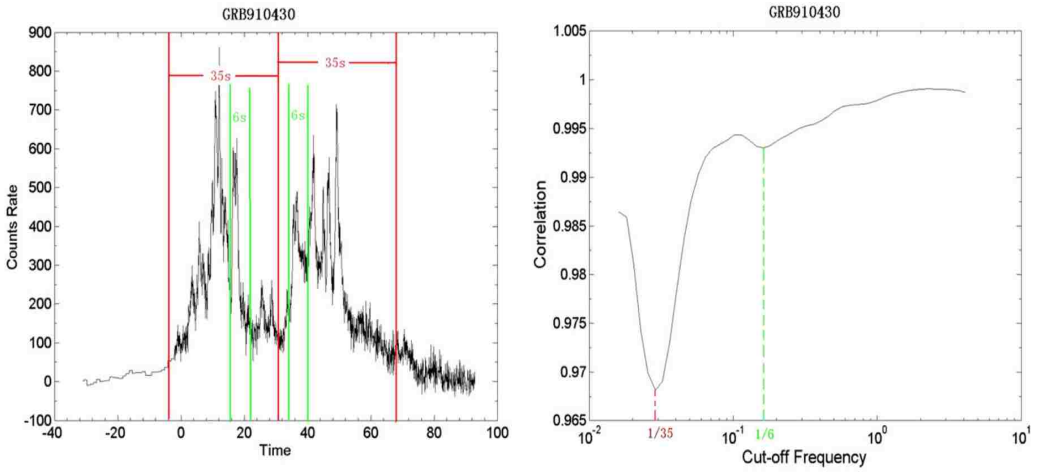

Figure 3 An example of the fast and slow variability components from (Gao, H., Zhang, B.-B., Zhang, B. 2012. Stepwise Filter Correlation Method and Evidence of Superposed Variability Components in Gamma-Ray Burst Prompt Emission Light Curves. The Astrophysical Journal 748, 134, © AAS. Reproduced with permission) using the stepwise low-pass filter correlation (SFC) statistical method. The two dips on the right panel show the possible two variability components of GRB 910430.

law distribution with an index -5/3 for BATSE GRBs (Beloborodov, 2000) and -1.7 to -2.0 for Swift GRBs (Guidorzi et al., 2012). More recently, by introducing a stepwise low-pass filter correlation (SFC) statistical method, Gao et. al. (2012) found that, for many individual GRBs, the lightcurves can be decoupled into two components: a long duration slow component superposed by a short duration fast component (Fig.3).

- Broad-band prompt emission:

  Before the Swift era, we can only detect the prompt emission in a relatively narrow band-pass (around sub-MeV γ-ray band). After Swift operating in orbit, thanks to its fast slewing capability and (in some cases) the received signal from a precursor, people successfully simultaneously detected the prompt emission from optical to sub-MeV γ-ray band for some bursts (Romano et al., 2006; Campana et al., 2006; Page et al., 2007). On the other hand, thanks to the GeV detecting capability of the *Fermi*/LAT, The high energy GeV emission

of several bursts were also detected. Some of their spectra are consistent with the Band-function fitting extending to the GeV energy range, while some other cases have an additional GeV emission component with a rising slope above the Band spectrum. These suggest the potential existence of emission in an even higher energy band (e.g. TeV).

Comparing the arriving time of the lightcurve pulses in different energy bands below 10 MeV, people found that the arriving time of a pulse in a softer energy band is systematically later than the pulse in a harder energy band in many long GRBs (Norris et al., 2000; Norris, 2002; Norris et al., 2005). This phenomenon is called "spectral lag". However, in the even higher energy range ($>$ 100 MeV), several cases show the delay of the GeV emission with respect to the MeV emission (Abdo et al., 2009c; Abdo et al., 2009a; Zhang et al., 2011). Figure 4 (Axelsson et al., 2012) shows an example of this phenomenon from the observations of GRB 110721A.

1.1.2 Spectral properties

From the analyses of many bursts, the spectra of prompt emission can be mainly decoupled into three components (Fig.5) (Zhang et al., 2011): I. a smoothly-joint broken power law spectral component named as "Band-function" (Band et al., 1993); II. a quasi-thermal spectral component; III. a single power law spectral component extending to both low and high energy regimes. For an individual burst, it does not definitely include all the three components in its observed spectrum. Actually most of the GRB prompt emission spectra can be well fitted only with the "Band-function" component. In the following, I will introduce the details of these three components.

- I. "Band-function" spectral component:

  This is the most widely found spectral component during prompt emission phase. Originally, the "Band-function" is generated from the data fitting point

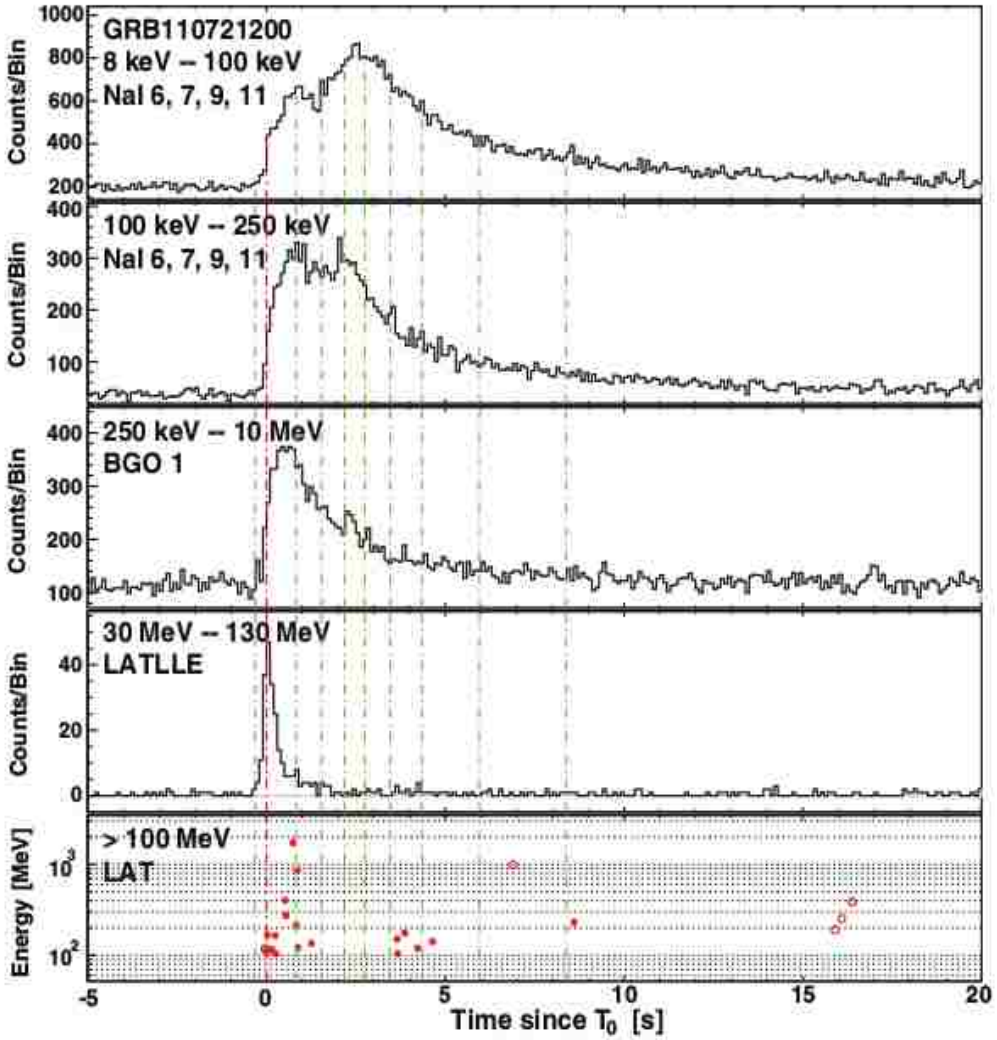

Figure 4 . An example (GRB 110721A) to show the spectrum lag (from Axelsson, M., and 110 colleagues 2012. GRB110721A: An Extreme Peak Energy and Signatures of the Photosphere. The Astrophysical Journal 757, L31) (© AAS. Reproduced with permission).

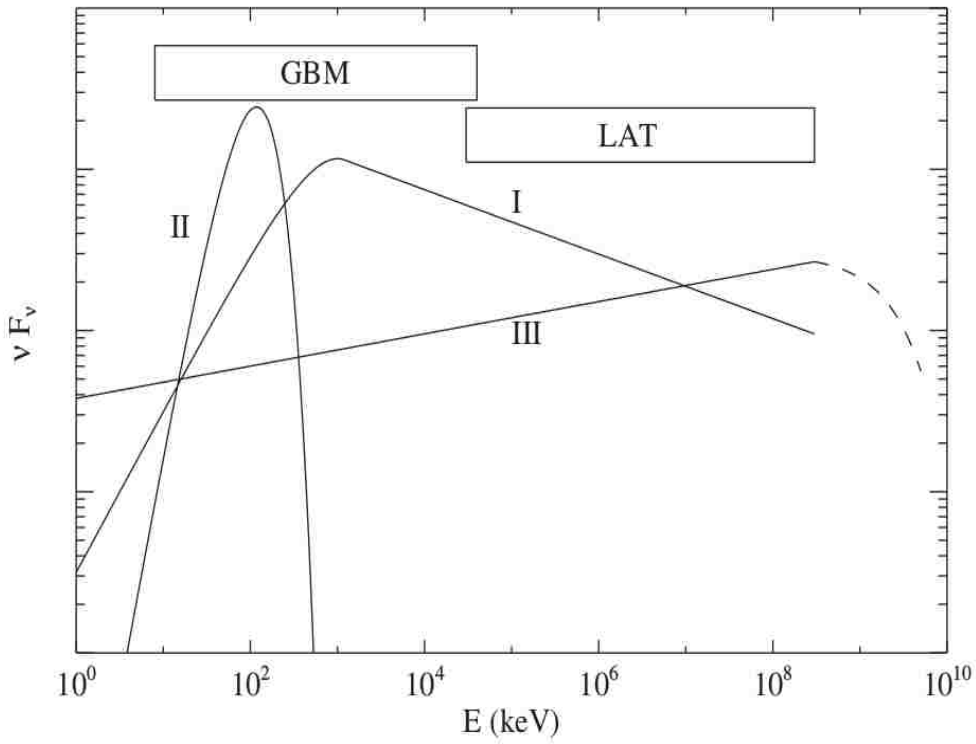

Figure 5 . Schematic diagram to show the three possible spectral components of GRB prompt emission. Different GRBs have different compositions of them. Adapted from (Zhang, B.-B., Zhang, B., Liang, E.-W., Fan, Y.-Z., Wu, X.-F., Pe'er, A., Maxham, A., Gao, H., Dong, Y.-M. 2011. A Comprehensive Analysis of Fermi Gamma-ray Burst Data. I. Spectral Components and the Possible Physical Origins of LAT/GBM GRBs. The Astrophysical Journal 730, 141, © AAS. Reproduced with permission).

of view and does not have a clear physical motivation. It is a smoothly-joint broken power law with a form shown in equation 1.1

$$N(E) = \begin{cases} A\left(\frac{E}{100\ \mathrm{keV}}\right)^{\alpha} \exp\left(-\frac{E}{E_0}\right) , & E < (\alpha-\beta)E_0 , \\ A\left[\frac{(\alpha-\beta)E_0}{100\ \mathrm{keV}}\right]^{\alpha-\beta} \exp(\beta-\alpha)\left(\frac{E}{100\ \mathrm{keV}}\right)^{\beta} , & E \geq (\alpha-\beta)E_0 , \end{cases} \tag{1.1}$$

where $N(E)$ ($photon\ counts \cdot cm^{-2} \cdot s^{-1} \cdot KeV^{-1}$) is the number of photons received in a certain energy band; A is a flux normalization factor; α and β are the power low spectral indices for the low-energy and high-energy segments, respectively; E_0 is the break energy between the two power law segments. Besides the "photon number" spectrum ($N(E)$ versus E), there are also two other forms to express the spectrum: 1. "specific flux density" spectrum ($E \cdot N(E)$ versus E, or F_ν versus ν, where ν is the photon frequency); 2. "spectral energy distribution (SED)" spectrum ($E^2 \cdot N(E)$ versus E, or νF_ν versus ν). The specific energy (E) corresponding to the maximum energy flux in the SED spectrum is called the peak energy (E_p). So the relationship between E_p and E_0 is

$$E_p = (2+\alpha)E_0. \tag{1.2}$$

An example of Band-function fitting done by Briggs et al. (1999) for GRB 990123 is shown in Figure 6. The value of the two spectral indices, constrained by the bright BATSE sample, are $\alpha \sim -1 \pm 1$ and $\beta \sim -2^{+1}_{-2}$ (Preece et al., 2000), which are also confirmed with the $Fermi$ and INTEGRAL samples (Zhang et al., 2011; Nava et al., 2011; Bošnjak et al., 2013). In the BATSE era, the E_p of the bright BATSE sample is distributed around 200-300 KeV (Preece et al., 2000). However, the softer detectors $HETE-2$ and $Swift$ observed some cases with a much lower E_p, which makes the peak energy distribution much wider from several keV to tens of MeV (Gruber et al., 2014; Bošnjak et al., 2014).

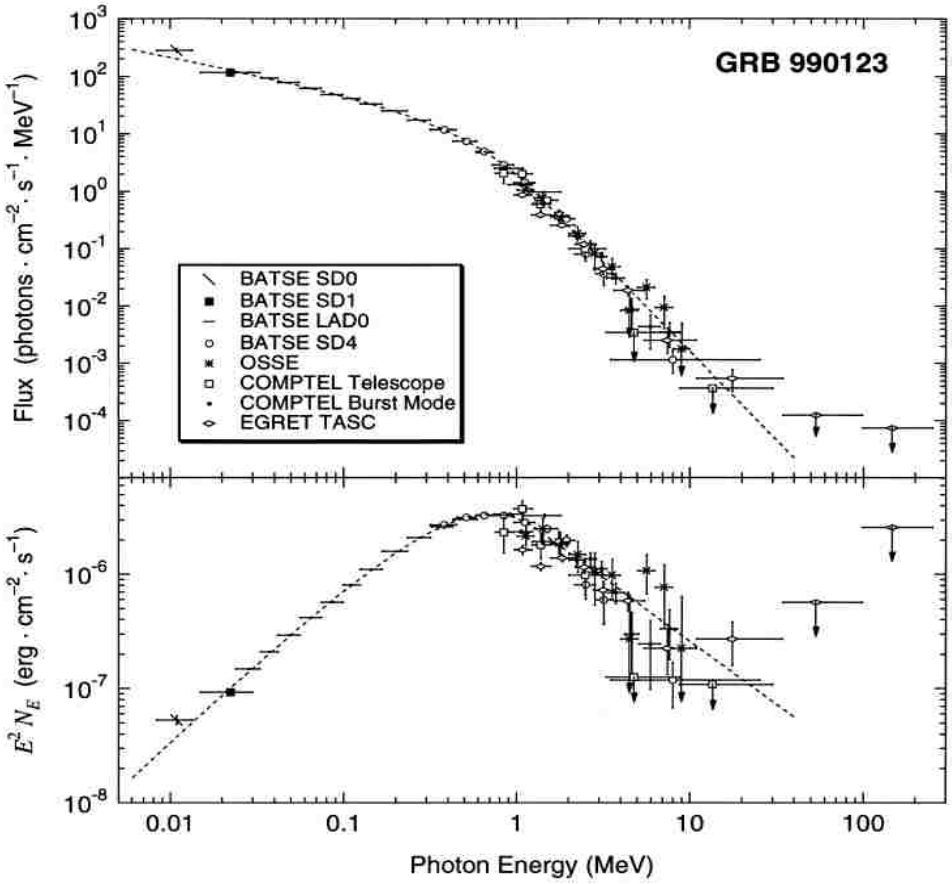

Figure 6 . An example case (GRB 990123) of the Band-function spectrum (from Briggs, M. S., and 17 colleagues 1999. Observations of GRB 990123 by the Compton Gamma Ray Observatory. The Astrophysical Journal 524, 82-91) (© AAS. Reproduced with permission).

Before the *Fermi* era, Ryde (2005); Ryde & Pe'er (2009) suggested that the observed Band spectra of many BATSE GRBs is the superposition of a thermal component and a non-thermal power law component, which means the Band spectrum may not be an independent spectral component for these samples. Although this "hybrid" model fitted observations well in the narrow BATSE band-pass, it actually over-predicted the X-ray flux from the associated Beppos-SAX observations for most of the bursts (Ghirlanda et al., 2007; Frontera et al., 2013). These results hint that, for most of the cases, the Band spectrum still does a better job than the "hybrid" model in a wider energy band. Entering into the *Fermi* era, thanks to its much wider band-pass than previous instruments, in spite of several special cases, most of the GRB spectra show a significant Band-function component within a wide energy band. A famous example is GRB 080916C whose time resolved spectra are shown in the top left panel of Figure 7 (Abdo et al., 2009b) with clear Band spectrum spreading in six orders of magnitude in energy range.

- II. Quasi-thermal spectral component:

  Besides the widely existent Band spectral component, several cases were found with a clear quasi-thermal spectral component. A famous case is GRB 090902B (bottom left panel of Figure 7) (Abdo et al., 2009b). The spectrum of it consists of the superposition of a quasi-thermal component and an underlying power law component (Ryde et al., 2010; Zhang et al., 2011). In addition, Zhang et al. (2011) did a detailed analysis for the time resolved spectra and found that with the smaller time bin, the quasi-thermal component becomes close to the blackbody spectrum, which supports that for this particular case the emission is dominated by the thermal component.

  From the statistics point of view, Zhang et al. (2011) did detailed time resolved

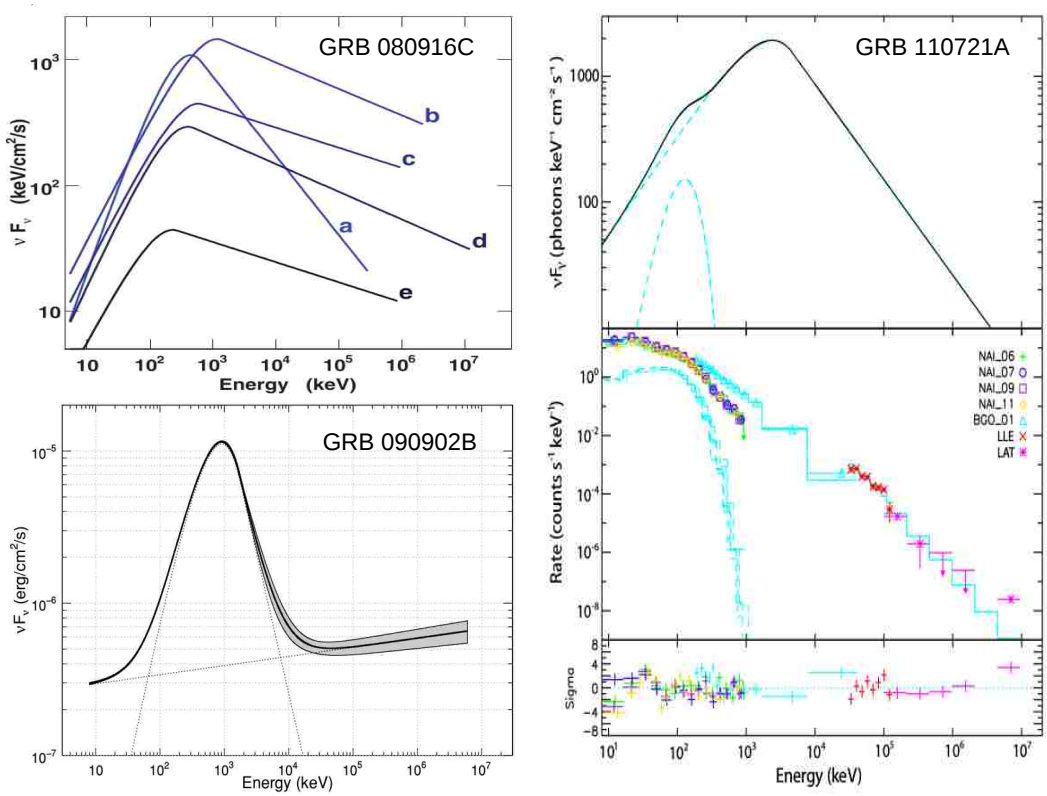

Figure 7 . The typical spectral samples for different types of spectral components from *Fermi* observations. Top left panel: The time resolved spectra of GRB 080916C which show significant Band-function component within wide energy band (from Abdo, A. A., and 253 colleagues 2009. Fermi Observations of High-Energy Gamma-Ray Emission from GRB 080916C. Science 323, 1688, reprinted with permission from AAAS). Bottom left panel: A time resolved spectrum of GRB 090902B (time bin: 4.6 s to 9.6 s) which shows clear thermal plus power law spectral components (from Abdo, A. A., and 205 colleagues 2009. Fermi Observations of GRB 090902B: A Distinct Spectral Component in the Prompt and Delayed Emission. The Astrophysical Journal 706, L138-L144, © AAS. Reproduced with permission). Right two panels: Time integral spectra of GRB 110721A which show the superposition between thermal and Band-function spectral components (from Axelsson, M., and 110 colleagues 2012. GRB110721A: An Extreme Peak Energy and Signatures of the Photosphere. The Astrophysical Journal 757, L31, © AAS. Reproduced with permission).

spectra analyses for 17 *Fermi*/LAT GRBs. The results showed that, most of them (14/17) have a Band-dominant spectrum, while only 2/17 have a thermal-dominant spectrum[2].

From *Fermi* observations, there are also some GRBs that have both Band and thermal spectral components co-existent at the same time. The right two panels of Figure 7 (Axelsson et al., 2012) show the time integrated spectra of GRB 110721A which is an example for the co-existence of both spectral components I and II.

- III. Power law spectral component:

  Besides the above two components, for some GRBs, there also exists a power law spectral component extending to high energy band or both high and low energy bands. In the high energy part (> 100 MeV), several cases[3] show an obvious rising power law component in the νF_ν spectrum. Since the total emission energy should be a finite value, the high energy power law spectrum should have a turnover or cut-off in certain high energy range. Such a feature has already been observed in GRB 090926A (Ackermann et al., 2011).

- Spectral evolution – E_p:

  From the detailed time resolved spectra studies, people found that the value of E_p actually evolves with time. Combining the evolution of the prompt emission lightcurve, two different patterns were found. The first pattern is that the value of E_p increases when the flux of the lightcurve increases (rising phase of the pulse), and then E_p decreases with the decreasing of the flux (decaying phase of the pulse). This is called "tracking" behavior (Golenetskii et al., 1983). Another type of pattern is that the value of E_p decreases all the way to a lower

[2]They are GRB 090902B and GRB 090510.

[3]E.g. GRB 090510 (Abdo et al., 2009a), GRB 090902B and GRB 090926A (Ackermann et al., 2010; Ackermann et al., 2011).

value during both the rising and decaying phases of the lightcurve pulse. This is called "hard-to-soft" behavior (Norris et al., 1986). Figure 8 shows some examples of the two types of E_p evolution (Lu et al., 2012). For the GRBs with multiple pulses, both of the two patterns can co-exist in a same burst for different pulses (Lu et al., 2010, 2012). Statistically, the "hard-to-soft" behavior is more common in the first pulse, while the "tracking" behavior is more popular in the later pulses. Simulations done by Lu et al. (2012) showed that, for some cases, the "tracking" pattern in the later pulses could be formed by the superposition of several "hard-to-soft" patterns, and furthermore, Hakkila & Preece (2011) argued that the "hard-to-soft" evolution pattern may be ubiquitous among long GRBs. However, the existence of the "tracking" behavior in the first pulse or solo pulse of the lightcurve suggests that the "tracking" behavior of E_p evolution is likely intrinsic.

- Spectral evolution – delayed onset of the high energy power law spectral component:

  The time resolved spectra of some *Fermi*/LAT GRBs show that the high energy power law spectral component emerges in relatively later time bins. For example, the time resolved spectra of GRB 090926A shown in Figure 9 (Ackermann et al., 2011) show that there is no obvious high energy power law spectral component until 9.7 s. This is probably related to the delayed onset of the GeV emission.

1.1.3 Polarization

Besides the lightcurve and spectrum information of the prompt emission, the polarization measurement provides another important channel to investigate the mechanism of GRB prompt emission. Significant linear polarization of several cases have been claimed. Using the RHESSI data of GRB 021206, Coburn and Boggs (2003)

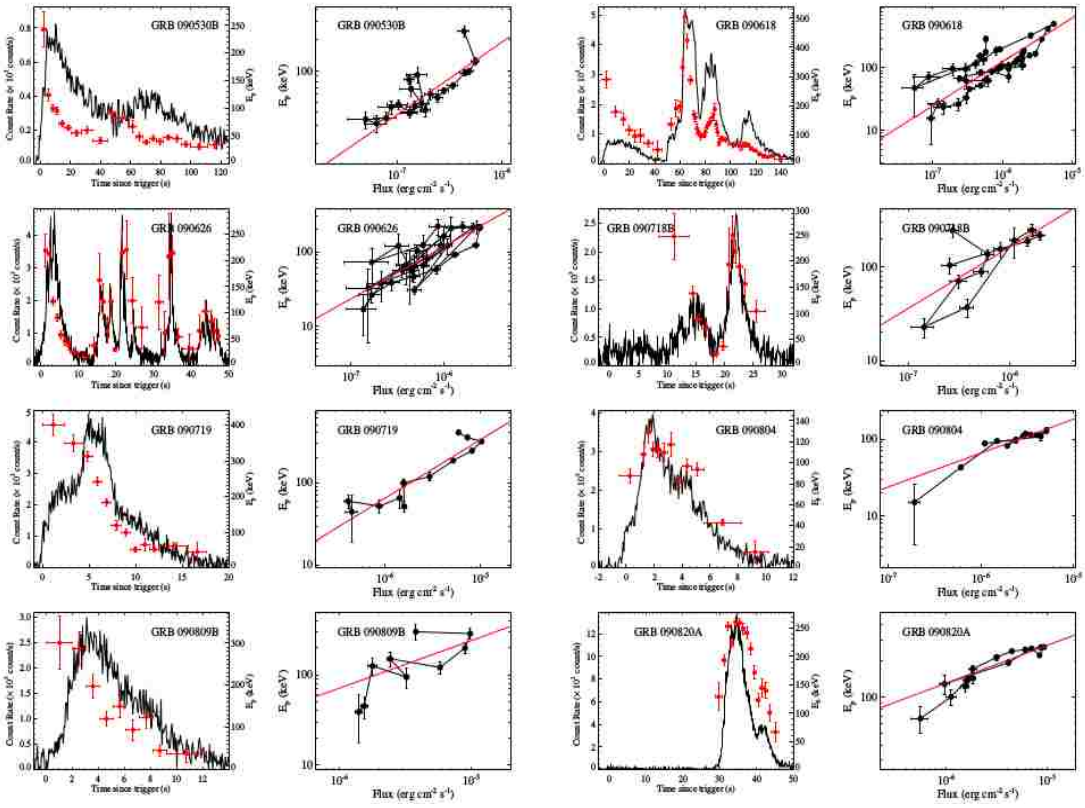

Figure 8 . Some examples of the two types ("hard-to-soft" and "tracking") of E_p evolution (from Lu, R.-J., Wei, J.-J., Liang, E.-W., Zhang, B.-B., Lü, H.-J., Lü, L.-Z., Lei, W.-H., Zhang, B. 2012. A Comprehensive Analysis of Fermi Gamma-Ray Burst Data. II. E $_p$ Evolution Patterns and Implications for the Observed Spectrum-Luminosity Relations. The Astrophysical Journal 756, 112) (© AAS. Reproduced with permission).

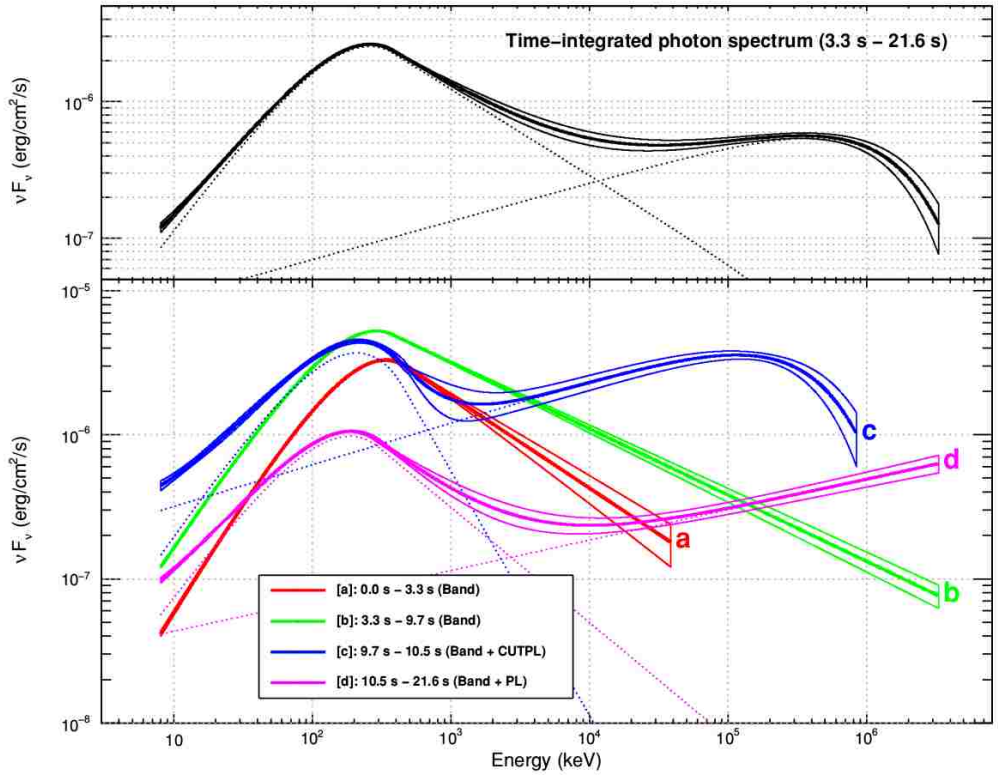

Figure 9 . The time resolved spectra of GRB 090926A to show the delay onset of high energy power law spectral component. (from Ackermann, M., and 198 colleagues 2011. Detection of a Spectral Break in the Extra Hard Component of GRB 090926A. The Astrophysical Journal 729, 114) (© AAS. Reproduced with permission)

claimed a very high linear polarization degree (PD) = $(80 \pm 20)\%$, but the following independent study carried by (Rutledge and Fox, 2004) did not confirm that result. Then Willis et al. (2005) found another two high linear PD cases which are GRB 930131 with PD $> 35\%$ and GRB 960924 with PD $> 50\%$, using the data from BATSE Albedo Polarimetry System (BAPS). Using the data from SPI instrument on INTEGRAL, although the result was not significant enough to be confirmed, Kalemci et al. (2007); McGlynn et al. (2007) found some possible high linear PD about $(98 \pm 33)\%$. Recently, more clear polarization results have been obtained using the data coming from GAmma-ray burst Polarimeter (GAP) on board of IKAROS. They are GRB 100826A with linear PD = $(27 \pm 11)\%$ at 2.9σ significance level (Yonetoku et al., 2011), GRB 110301A with linear PD = $(70 \pm 22)\%$ at 3.7σ significance level and GRB 110721A with linear PD = $(84^{+16}_{-28})\%$ at 3.3σ significance level (Yonetoku et al., 2012). Besides the PD information, the associated polarization angle (PA) evolution is an additional important information to study the prompt emission mechanism. For example, Yonetoku et al. (2011) reported a significant PA change (about 90 degrees) between the two pulses of GRB 100826A. Although, right now, the polarization sample is not as much as the GRB sample itself, it still gives important supplement information to constrain the theoretical models. In the future, with more powerful high-energy polarimeters launched, the polarization information will do a better job to constrain the models together with the spectrum and lightcurve.

In this section, I introduce the main observational features of the GRB prompt emission. In order to interpret them and understand the mechanism of prompt emission, many theoretical models have been proposed. In the next section, I will introduce several widely discussed models.

1.2 Main Theoretical Models of GRB Prompt Emission

Different leptonic prompt emission models[4] can be separated as three types from the point of view of their basic physical considerations. They are "internal shock (IS)" model, "dissipative photosphere" model, and "magnetic dissipation" model. The common feature of the IS model and photosphere model is that, regardless of the initial energy composition of the outflows, they all become matter-flux-dominated (MFD) ($\sigma < 1$) at the radius ($R_{\rm GRB}$) in which the main prompt emission is produced, where σ is the magnetization parameter defined as the ratio between the electromagnetic field (EMF) energy flux to the plasma matter energy flux. Contrarily, the magnetic dissipation model suggests that the outflow is still in the Poynting-flux-dominated (PFD) ($\sigma > 1$) regime at the site of $R_{\rm GRB}$. The different energy composition will lead to significant differences for the subsequent energy dissipation process, particle acceleration mechanism, radiation spectrum and lightcurve, polarization behavior, and so on. In the following, I will summarize the main features, advantages, and disadvantages of them. Figure 10 is a carton picture to show the different emission sites for different models, which can be used as a reference figure in the following discussions.

1.2.1 IS model

There are two types of IS models. The first one is the classic "Fireball internal shock (FIS)" model (Mészáros & Rees, 2000; Rees and Mészáros, 1994; Kobayashi et al., 1997; Daigne & Mochkovitch, 1998). Another one is the "Magnetized engine internal shock (MIS)" model (Bošnjak et al., 2009; Daigne et al., 2011).

- FIS model:

  The fireball internal shock model is assumed that the central engine initially

[4]There also have some hadronic prompt emission models discussed by several literatures. In my dissertation, I mainly focus on the leptonic models.

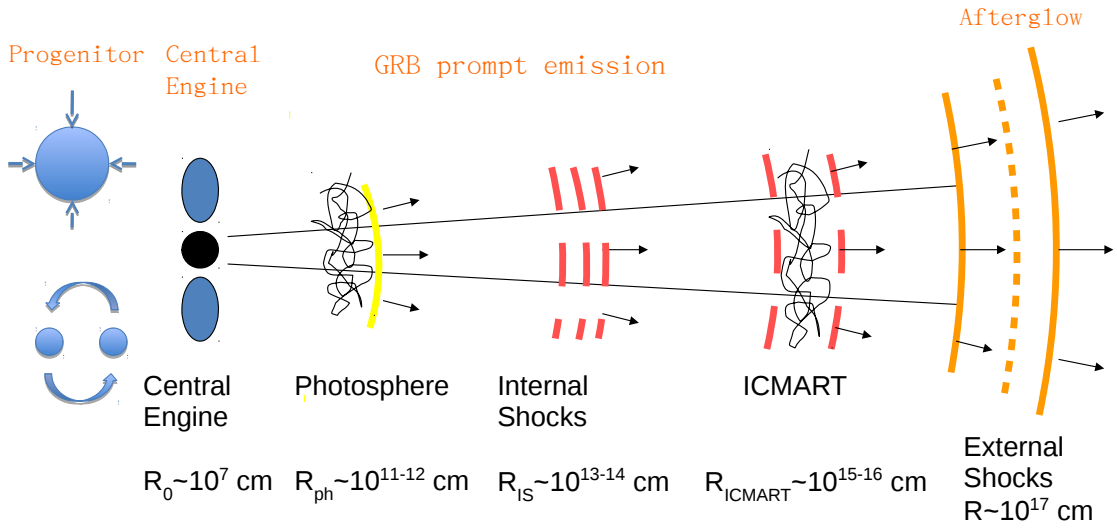

Figure 10 . The carton picture to show the prompt emission sites for different models (adapted from Fig.1 of Zhang, B., Yan, H. 2011. The Internal-collision-induced Magnetic Reconnection and Turbulence (ICMART) Model of Gamma-ray Bursts. The Astrophysical Journal 726, 90, © AAS. Reproduced with permission).

launches MFD jet/outflow which forms very high temperature fireball mainly consisted by photons, $e^{\pm}$ pairs, neutrinos and a little protons. Then the hot fireball will undergo adiabatic expansion and transfer the thermal energy to the kinetic energy of the outflow to accelerate the outflow to ultra-relativistic speed (Shemi and Piran, 1990). Meanwhile, the optical depth of the ejecta continuously decreases during the expansion process and becomes optically thin at a certain radius which is called the photosphere radius $R_{\rm ph}$, then the thermal emission is released to the observer from the photosphere. In addition, due to the high variability of the central engine, the ejected outflow is very likely episodic and forms many ultra-relativistic shells with more or less different bulk Lorentz factors. The later faster shells will catch up and collide with the earlier slower shells to form shocks which are called internal shocks. The particles will be accelerated to a non-thermal distribution by the shocks and radiate non-thermal emission mainly by synchrotron mechanism. So the FIS model potentially has two spectral components: thermal emission from the photosphere and non-thermal emission form the internal shocks. The non-thermal emission generates the main Band spectral component and decides the position of E_p, and the thermal emission will give more or less modification to the observed spectrum from the thermal spectral component[5]. The merits and issues of this model are summarized in below:

Main merits:

1. The studies of the X-ray flares (e.g. Liang et al. (2006a)) showed strong evidence that the central engine is fast variable and likely restarts many times to produce the X-ray flares. Since the prompt γ-ray emission very likely shares the

[5]Ryde (2005); Ryde & Pe'er (2009) suggested that the Band spectrum can be the superposition of the dominant thermal emission from the photosphere and the sub-dominant non-thermal power low emission from the internal shocks. As we discussed in the above observation section, this model, except some special cases, is disfavored when new observations with wider energy band are got by *Fermi*.

same origin with the X-ray flares (Krimm et al., 2007), the observed variability of prompt emission is probability also driven by the central engine variability directly. So the multiple ejected shells, as required by the IS model, are natural products of the episodic emission to interpret the fast variability of the prompt emission.

2. Shocks widely exist in many astrophysical systems, such as AGNs, planetary nebulae, solar system, and so on. And after tens of years studies from both theoretical and numerical works, shock acceleration mechanism is well understood to produce the non-thermal emission. So it is natural to introduce the shock process into the GRB models to see if it works, moreover, it does interpret some observations to a certain extent.

Main issues:

1. *Low efficiency problem:* In the internal shock scenario, the shock energy comes from the kinetic energy loss during the collisions between different shells, and then particles gain energy from the shocks and produce non-thermal emission. Detailed calculations, considering a random distribution of mass and Lorentz factor of many shells, showed that the radiative efficiency in the observed band is only about 1 to 10 percent (Kobayashi et al., 1997; Kumar, 1999; Panaitescu et al., 1999; Kobayashi and Sari, 2001; Maxham & Zhang, 2009). This value is much smaller than the observation constrained efficiency which is about or above 50 percent (Zhang et al., 2007; Fan and Piran, 2006b).

2. *The electron number excess problem:* Due to the low kinetic energy conversion efficiency mentioned above and the MFD outflow which provides so many particles, if all the electrons share the dissipated energy equally, they can't be accelerated to high enough energy to produce the observed spectral parameters. So it should be assumed that only 1% of the total electrons get about 10% of

the energy in the shocked fluid to match the observations (Daigne et al., 2011).

3. *Missing bright photosphere problem:* Based on the FIS model, the energy of the internal shock, which produces the observed emission, comes from the initial hot fireball, so people can constrain the thermal emission flux associated with the non-thermal emission. Several studies (Mészáros & Rees, 2000; Mészáros et al., 2002; Pe'er, 2008) found that this thermal emission should be bright enough to be detected as a common significant spectral component besides the Band spectral component. However, recent wide band observations taken by *Fermi* found that the thermal emission is actually not so significant or completely non-detectable in most of the observed GRB spectra (Zhang et al., 2011). Furthermore, Zhang & Pe'er (2009) took detailed calculations for the GRB 080916C which has great observational data, and found that the predicted thermal emission flux should be more than one order higher than the non-thermal companion. However the observation of this event shows no thermal component at all. This "missing bright photosphere" issue becomes a big challenge to the FIS model.

- MIS model:

  The "Magnetized engine internal shock" model suggests that the central engine initially launches PFD jet/outflow which will accelerate the outflow to ultra-relativistic speed due to the strong magnetic pressure. During this process, the magnetic energy is mainly converted to the bulk kinetic energy of the outflow. Then, similar to the FIS model, multiple internal collisions will happen and generate the internal shocks to produce the observed non-thermal emission. The main differences between the MIS model and the FIS model are the different jet composition and the different acceleration mechanism to produce the ultra-relativistic outflow. So from the advantage point of view, the merits 1 &

2 of FIS model are also suitable for the MIS model. Besides those two points, since there is no initial hot fireball, this model can potentially avoid the "missing bright photosphere" issue within the FIS scenario. From the disadvantage point of view, the first two issues from the IS scenario still exist. In addition, detailed calculations showed that the magnetic acceleration is not as efficient as the fireball (Granot et al., 2011). The outflow needs much longer time to be accelerated to the ultra-relativistic speed, which means a much larger emission radius that is inconsistent with the IS model. Gao & Zhang (2015) studies in detail and showed that contrived parameters are required for such a model.

1.2.2 Dissipative photosphere model

The dissipative photosphere model suggests that the Band spectrum is actually generated by the modified thermal emission from the dissipative photosphere, and the E_p is decided by the photosphere temperature. After introducing the energy dissipation around the photosphere, some non-thermal particles can be produced and then generate the power law spectrum above the E_p from the Compton up-scattering process (Beloborodov, 2010; Lazzati & Begelman, 2010).

Main merits:

1. Before the $Swift$ era, the E_p distribution is relatively narrow around MeV range. This is consistent with the referred photosphere temperature to produce the observed E_p which is not sensitive with the change of luminosity (Beloborodov, 2013). However, as discussed in the following issue part, with the new samples collected by $Swift$ and $Fermi$, this support becomes much weaker.

2. The efficiency from the photosphere emission is high enough to avoid the low efficiency problem existing in IS model (Lazzati et al., 2009).

3. This model naturally avoids the "missing bright photosphere" problem, since the main spectrum comes from the photosphere itself.

Main issues:

1. *E_p problem:* After the launched of *Swift* and *Fermi*, thanks to their more advanced capabilities, more and more cases show that the observed E_p no longer so concentrate around MeV. It can actually spread in a wide energy range from several KeV to above MeV, when X-ray flashes are included. This becomes a challenge for the photosphere model which predicts that the E_p is insensitive with the change of luminosity ($\propto L^{1/4}$) and clusters around MeV. More specifically, Zhang et al. (2012) calculated the maximum allowable E_p for different luminosity based on the photosphere model, and got a "death line" in the luminosity-E_p domain. They found that the E_p of GRB 110721A ($\sim$ 15 MeV early on) is significantly higher than the "death line", which means that, at least for this case, the photosphere model is not favored. In addition, since the spectrum of this burst is just the common Band spectrum with typical spectral parameters which are similar to most of the other GRBs, it hints that the photosphere emission may not be the origin of the dominant Band spectral component. On the other hand, the "hard-to-soft" patten of the E_p evolution, introduced in the above observation section, is another challenge for the photosphere model (Deng & Zhang, 2014). I did a detailed study for this problem and will introduce this work in Chapter 2.

2. *GeV emission problem:* Since the photosphere radius ($R_{\rm ph} \sim 10^{11}$ cm) is relatively small and the opacity of pair production is high enough to prevent the release of GeV photons. However, the *Ferimi* LAT observations revealed that the Band spectrum can extend to larger than 10 GeV range (e.g. GRB 080916C), which gives another big challenge for the photosphere model. Some authors proposed "two emission zones" model to overcome this issue, which considers that the GeV emission is produced by other emission region in larger radius, e.g. external shock (Kumar and Barniol Duran, 2009; Ghisellini et al., 2010). However, during the prompt emission phase, the GeV emission shows good tracking behavior with the prompt sub-MeV

emission. This phenomenon means that the GeV emission should be produced in the same emission site which is inconsistent with the "two emission zones" model.

3. *Low energy spectrum problem:* Another major issue of the photosphere model is that it is hard to produce the correct spectral index (α) below the E_p. Observationally, α is around -1, while the theoretical calculation (Beloborodov, 2010; Deng & Zhang, 2014) got $+0.4/0.5$ considering the superposition of multiple photosphere emissions due to the episodic outflow. Deng & Zhang (2014) also found that the spectrum will probably be softened to make α close to -1 during the decaying phase of the pulse of lightcurve with steep decaying index. However, the time resolved spectra from observations do not show this kind of transition feature. I will give more details of our work for these calculations in Chapter 2. Lundman et al. (2013) introduced a special structure jet model with Lorentz factor decaying with latitude but keeping the luminosity uniform. In this situation, the high latitude emission is enhanced which can modify the spectral index close to -1. However, there is no evidence to directly prove this kind of jet structure. If the luminosity is also decaying with latitude following with the change of Lorentz factor, which is a more self-consistent situation, the predicted spectral index will become much different from the observations again.

4. An independent quasi-thermal spectral component accompanying with the Band spectrum has already been observed for some GRBs (e.g. GRB 110721A shown in Fig.7). This thermal component is likely produced by the photosphere emission (Ryde & Pe'er, 2009). If this thermal component is of the photosphere origin, the main Band component should likely be of a different origin.

1.2.3 Magnetic dissipation model

As I mentioned at the beginning of this chapter, the magnetic dissipation model suggests that the outflow is still in PFD ($\sigma > 1$) status at the prompt emission radius $R_{\rm GRB}$. There are several magnetic dissipation models (Lyutikov & Blandford,

2003; Zhang & Yan, 2011; McKinney and Uzdensky, 2012). In my dissertation, I mainly focus on the "Internal-Collision-induced MAgnetic Reconnection and Turbulence (ICMART)" model proposed by Zhang & Yan (2011). The main idea of the ICMART model is that the central engine initially launches episodic PFD outflow. Then the magnetic pressure accelerates the outflow to become ultra-relativistic jet. Due to the velocity difference between the different magnetized shells, the multiple collisions will likely occur similar to the internal shock scenario. However, since the σ value remains high, there is no strong shock produced during the internal collisions. The main effect of the collisions is distorting the magnetic field and finally triggering multiple cascade fast reconnections and turbulence at larger radius $R_{\rm ICMART} \sim 10^{15}$ cm. The particles are accelerated to non-thermal population by the fast reconnections and/or turbulence, and then generate the prompt emission mainly from the synchrotron radiation.

Main merits:

1. The magnetic reconnection potentially has a very high efficiency to convert the magnetic energy to the internal and kinetic energy of the fluid (Deng et al., 2015). And the electron excess problem is also avoided, since the PFD jet has much less electrons than the MFD jet.

2. This model naturally avoids the missing bright photosphere problem, since the photosphere emission is easily suppressed due to the small fraction of the matter flux in the outflow.

3. The large emission radius favors moderately fast cooling of electrons, and meanwhile, the reconnection process gives another way to continuously decrease the strength of magnetic field, which can account for the right low-energy spectral index observed in GRBs (Uhm & Zhang, 2014).

4. The large emission radius also ensures that the optical depth of pair production is low enough to release the GeV photons from the same emission site as the sub-MeV

prompt emission.

5. It also gives a natural explanation of the two components observed in many GRBs (Gao et. al., 2012). The seconds-duration of the "slow variability component" can be interpreted as the variability of the central engine activity. The rapid "fast variability component" can be interpreted within this scenario as mini-jets due to locally Lorentz boosted regions (see also Lyutikov & Blandford 2003; Narayan & Kumar 2009[6]). It is speculated that turbulent reconnection in a moderately high-σ flow can give rise to relativistic motion of mini-jets within the bulk relativistic motion of the jets.

6. The recent magnetic reconnection simulations using Particle-in-cell (PIC) method showed that the magnetic reconnection in high-σ regime can efficiently accelerate particles to non-thermal power law distribution with even harder particle spectrum ($dN/d\gamma \propto \gamma^{-1}$) than the simple shock acceleration mechanism (Sironi & Spitkovsky, 2014; Guo et al., 2014). This gives a good support for the ICMART model from the particle acceleration point of view.

The ICMART model provides several encouraging ideas and theoretical estimations to potentially solve several main issues existing in other types of models, however, since some important ingredients of this model are still of a speculative nature, the follow-up detailed numerical simulation works are definitely needed to give a solid footing to this model. This is the main focus of the second part of my dissertation (Chapter 3).

[6]Lyutikov & Blandford (2003) and Narayan & Kumar (2009) proposed that GRB variability is a consequence of mini-jets due to relativistic outflow from reconnection or relativistic turbulence. There is no simple explanation to the observed slow variability component in these models. Zhang & Yan (2011) attributed the two variability components (slow and fast) as due to central engine activity and mini-jets, respectively. Monte Carlo simulations by Zhang & Zhang (2014) showed that the ICMART model can indeed reproduce the observed GRB light curves.

CHAPTER 2

LOW ENERGY SPECTRAL INDEX AND E_p EVOLUTION OF QUASI-THERMAL PHOTOSPHERE EMISSION OF GAMMA-RAY BURSTS

This chapter is based on the following published paper :

Deng, W., & Zhang, B. 2014, The Astrophysical Journal, 785, 112

2.1 Motivation and Introduction

As I mentioned in Chapter 1, despite more than 40 years of observations of gamma-ray bursts (GRBs), the radiation mechanism during the prompt emission phase is still being debated. Observationally the time-resolved spectra are usually characterized by a smoothly-joint broken power law, known as the "Band" function (Band et al., 1993). The typical value of the low-energy photon spectral index α (the one below the peak energy E_p) is around -1 (Preece et al., 2000; Zhang et al., 2011; Nava et al., 2011)[1]. This value is not straightwardly predicted in available models. In general there are two broad categories of GRB prompt emission models, one invoking a Comptonized quasi-thermal emission from the photosphere of the outflow (Thompson, 1994; Ghisellini & Celotti, 1999; Mészáros & Rees, 2000; Mészáros et al., 2002; Rees & Mészáros, 2005; Pe'er et al., 2006; Thompson et al., 2007; Pe'er, 2008; Giannios, 2008; Beloborodov, 2010; Lazzati & Begelman, 2010; Ioka, 2010; Toma et al., 2011; Pe'er & Ryde, 2011; Mizuta et al., 2011; Lundman et al., 2013; Lazzati et al., 2013; Ruffini et al., 2013), the other invoking a non-thermal (synchrotron or synchrotron-self-Compton) mechanism in the optically thin region (Mészáros et al., 1994; Tavani, 1996; Daigne & Mochkovitch, 1998; Lloyd & Petrosian, 2000; Zhang & Mészáros, 2002a; Kumar & Panaitescu, 2008; Zhang & Pe'er, 2009; Wang et al., 2009; Kumar & Narayan, 2009; Daigne et al., 2011; Zhang & Yan, 2011; Zhang et al., 2012; Veres et al., 2012; Burgess et al., 2011; Uhm & Zhang, 2014). Recent observations with

[1]Some GRBs show a harder α value in the time resolved spectra at the beginning or around the peak of the light curve (Ghirlanda et al., 2002, 2003). In some other cases, a blackbody component can play a dominant role (Ryde et al., 2010; Zhang et al., 2011; Ghirlanda et al., 2013).

Fermi (Ryde et al., 2010; Zhang et al., 2011; Guiriec et al., 2011; Axelsson et al., 2012; Guiriec et al., 2013) confirmed the pre-Fermi suggestion (Ryde, 2005; Ryde & Pe'er, 2009) that the observed GRB spectra sometimes include superposition of a quasi-thermal component with a non-thermal component[2], suggesting that the photosphere emission indeed contributes to the observed GRB spectra of at least some GRBs. The question is how much the photosphere emission contributes to the observed spectra. There are two different opinions. According to the first opinion, only the quasi-thermal component identified in some GRBs is of the photosphere origin (e.g. Ryde et al., 2010; Zhang et al., 2011; Guiriec et al., 2011; Axelsson et al., 2012; Guiriec et al., 2013), while the main "Band" component is non-thermal emission from an optically thin region. The second, more optimistic opinion suggests that the main Band component is of a photosphere origin, and the observed E_p is defined by the photosphere temperature (e.g. Rees & Mészáros, 2005; Thompson et al., 2007; Beloborodov, 2010; Lazzati & Begelman, 2010; Pe'er & Ryde, 2011; Lundman et al., 2013; Lazzati et al., 2013).

Within this second scenario, one needs to broaden the quasi-thermal spectrum to a mimic the observed "Band" function. The high-energy photon index can be easily interpreted by introducing dissipation of energy near photosphere so that non-thermal electrons are accelerated to upscatter the seed quasi-thermal photons (e.g. Lazzati & Begelman, 2010). However, the main difficulty is to account for the observed low-energy photon index $\alpha \sim -1$, since the predicted value is much harder than this value (e.g. Beloborodov, 2010). It has been speculated that geometric smearing and temporal smearing may soften the spectrum to make α closer to -1, but no thorough study has been carried out.

Another interesting observational feature is the E_p evolution in GRBs. Observtionally two patterns are identified: hard-to-soft evolution or E_p-intensity tracking

[2]Observational constraints demand that non-thermal component cannot be a single power law extending to much lower energies (Ghirlanda et al., 2007).

(Liang & Kargatis, 1996; Ford et al., 1995; Ghirlanda et al., 2010, 2011a,b; Lu et al., 2010, 2012) across a broad GRB pulse (or the "slow" variability component, Gao et. al., 2012). Various data analyses suggest that both patterns co-exist, sometimes in a same burst. For short GRBs, the tracking behavior is most common, while for long GRBs, especially for the first broad pulse, the hard-to-soft evolution is relatively more common. Simulations show that in long GRBs, tracking pulses after the first pulse could be due to a superposition of multiple hard-to-soft pulses (Lu et al., 2012), and it has been argued that the hard-to-soft evolution pattern may be ubiquitous among long GRBs (Hakkila & Preece, 2011). It is of great interest to see what E_p evolution pattern the photosphere model predicts.

In this chapter, we investigate the predictions of α values and E_p evolutions within the simplest photosphere model (a co-moving blackbody spectrum and a uniform jet) by fully treating the geometrical and temporal smearing effects. In Section §2.2, we describe our methodology, in particular, improvements upon previous work. We then present calculations of photosphere spectra and E_p evolution patterns in progressively more complicated models in Section §2.3. The conclusions are drawn in Section §2.4.

2.2 Methodology

2.2.1 Previous work on probability photosphere model

Photosphere may be roughly defined as a radius at which the Thomson scattering optical depth for a photon is $\tau = 1$. From the microscopic view, an individual photon in the outflow can be in principle last scattered by an electron at any position with a certain probability. One should introduce a probability function to describe photosphere emission (Pe'er, 2008; Pe'er & Ryde, 2011; Beloborodov, 2011). In general, for a group of photons emerging from deep inside the photosphere, they can undergo last scattering at any location (r, Ω) inside the outflow, where r is the radius from the explosion center, and $\Omega(\theta, \phi)$ defines the angular coordinates. A probability function

$P(r, \Omega)$ is introduced to describe the chance of last scattering at any location.

So far, a most detailed treatment of the probability function was presented in Pe'er (2008), Pe'er & Ryde (2011) and Beloborodov (2011). By making some simplifications in modeling, their model caught the essence of the photospheric physics. The basic physical picture of Pe'er & Ryde (2011) can be summarized as follows (see the cartoon picture Figure 11a): The central engine remains active for a while and forms a conical outflow. After some time the central engine is shut down. They assumed that the wind luminosity L_w, the initial mass loss rate $\dot{M}$, and hence, the initial bulk lorentz factor Γ, are all constant. This means that a continuous wind with a time-independent density profile is established. For simplicity, they also assumed that such a wind extends to an infinite distance. As a result, the optical depth could be directly calculated by an analytical formula, which is time-independent (Pe'er, 2008; Pe'er & Ryde, 2011). Another simplification of Pe'er & Ryde (2011) is that they only considered an instantaneous deposition of photons in one thin layer at the center of an expanding outflow plasma. In reality, photons are continuously deposited into a series of layers ejected by a long-lasting central engine. This would make calculations more complicated. A third simplification in their analytical approach is that they assumed a mono-energetic photon field, while in reality the photons have a distribution (e.g. blackbody in the co-moving frame). This assumption was removed in their numerical approach through Monte Carlo simulations. In any case, an analytical approach to handle the blackbody spectrum is welcome.

2.2.2 Improvements

In order to give a more precise treatment on more realistic situations, in this Chapter we make several critical improvements on the previous work to establish a more sophisticated photosphere model to study the instantaneous and time-integrated spectra and E_p evolution by allowing a time-varying central engine wind, and hence,

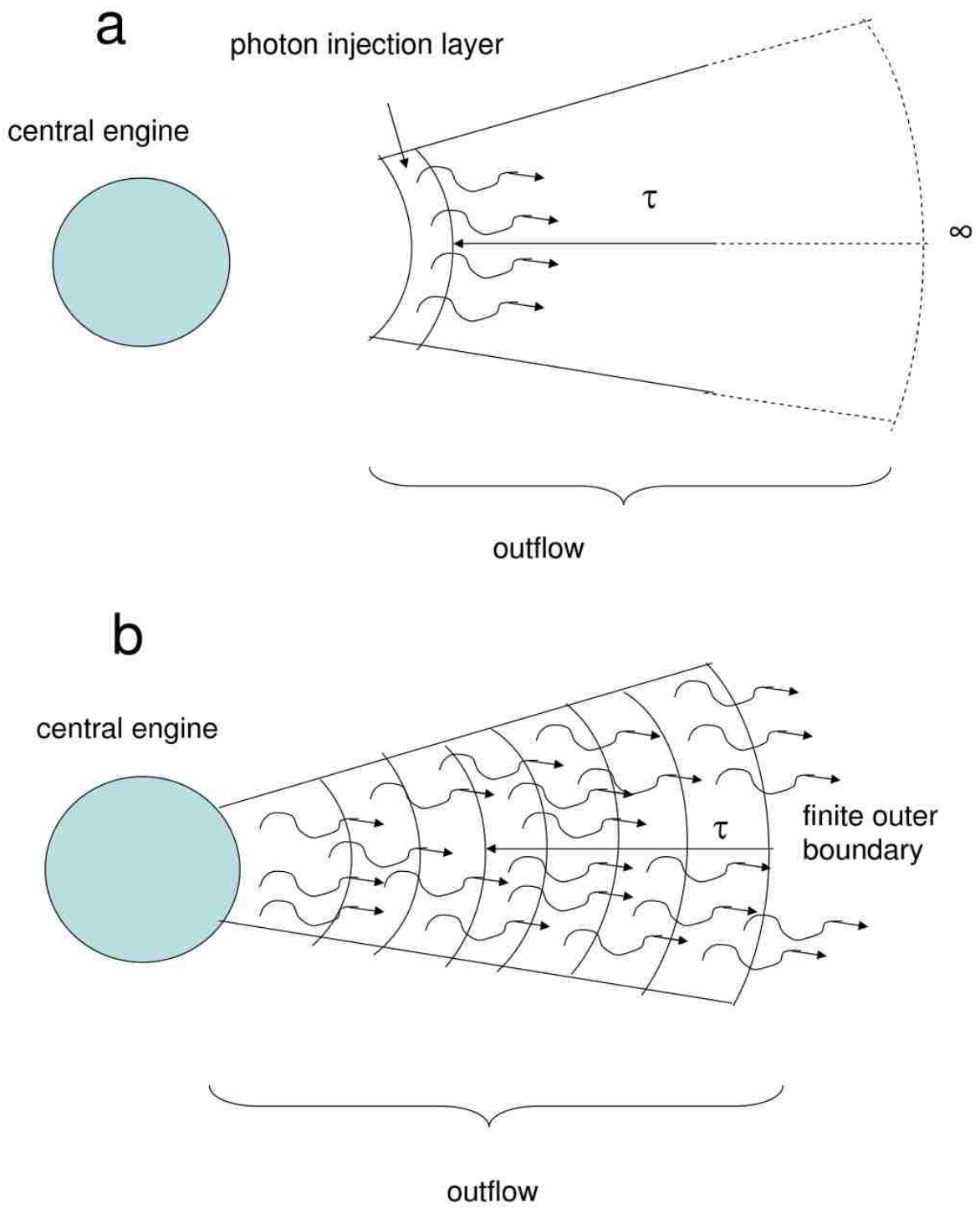

Figure 11 The carton picture for the model of Pe'er (2008); Pe'er & Ryde (2011) (a) as compared with ours (b).

the optical depth. Our improvements on the previous work include the following: 1. We introduce a blackbody distribution of the photons in the comoving frame, to replace the mono-energetic photon distribution in the analytical treatment of Pe'er (2008) and Pe'er & Ryde (2011); 2. For a wind lasting for a certain duration, at any instant, photons from different layers and latitudes, which were emitted at different epochs, are received. Instead of the traditional "equal-arrival-time-surface" effect commonly considered in an afterglow model, one needs to consider "equal-arrival-time-volume" for a more precise treatment of the photosphere emission. We separate the outflow into many thin layers, follow the last scattering of electrons from each layer individually, and calculate the sum of flux from all the layers from different latitudes and emission times, but at a same observer time; 3. We introduce a finite, dynamically evolving front of the outflow based on the assumed injection history of the outflow. This would affect the calculation of the Thomson scattering optical depth of the photons, which leads to a more precise derivation of the photosphere radius in different directions. The effect is especially important in the early phase of the outflow; 4. Since GRB lightcurves show an erratic behavior, we introduce time-dependent wind luminosity and baryon loading to allow a more realistic treatment of time-variable photosphere emission.

A cartoon picture of our improved model is shown is Fig.11b, as compared with Fig.11a. Due to the finite central engine activity time, the outflow has a finite thickness. We separate the outflow into many thin layers, each characterized by an initial wind luminosity L_w and an initial mass loading rate $\dot{M}$. To treat the equal-arrival-time volume effect, we consider two levels of integration. The first level handles the equal-arrival-time surface of each layer: photons emitted from different latitudes at different times arrive the observer at the same time; The second level handles superposition of emission from different layers: high-latitude emission from an earlier layer would arrive at the same time with low-latitude emission from a later layer.

In order to analytically treat the problem, some assumptions still need to be made. One important parameter is the Lorentz factor Γ of each layer. According to the standard fireball model (Mészáros et al., 1993; Piran et al., 1993; Kobayashi et al., 1999), Γ should initially increase with radius before coasting to a certain value. The coasting Γ depends on a comparison between the dimensionless entropy of the fireball η and a critical value η_c (Mészáros & Rees, 2000). If $\eta < \eta_c$, the photosphere radius r_{ph} is above the saturation radius $r_s = \eta r_0$ (where r_0 is the radius of the central engine), and the Lorentz factor coasts to a constant value $\Gamma_0 = \eta$. For $\eta > \eta_c$, the photosphere occurs during the fireball acceleration phase ($r_{ph} < r_s$). The Lorentz factor Γ would vary significantly across r_{ph}, which is difficult to handle analytically. In our treatment, we have made the assumption of a constant Γ_0 throughout the shell evolution (i.e. the acceleration phase is neglected). In our model, for a certain layer although all the positions have a certain probability to release the last-scattered photon, the maximum probability is concentrated around the photosphere radius r_{ph}. So our calculation of the emerging photosphere spectrum based on the assumption of a constant Γ_0 is accurate enough as long as $r_{ph} \gg r_s$, but would become progressively inaccurate as r_{ph} becomes progressively smaller. In our calculations, this constraint is considered in care, so that the presented spectra are all in the regime where this assumption is valid.

2.3 Models & Results

In this section, we calculate the photosphere spectra by progressively including the four new physical ingredients as discussed above. In §2.3.1 we introduce a blackbody spectrum in the comoving frame, while still keeping the basic assumptions of Pe'er & Ryde (2011) such as a constant wind luminosity, infinity outer boundary and single layer emission. In §2.3.2 we introduce multiple layers to study the superposed spectrum. In §2.3.3, keeping the wind luminosity constant, we introduce a time-

evolving outer boundary of the outflow. In §2.3.4 we introduce a time-dependent wind luminosity and time-evolving outer boundary of the outflow at the same time. A discussion on E_p evolution patterns are presented in §2.3.5.

2.3.1 Impulsive injection, outer boundary at infinity, blackbody distribution of photons

In this section we still keep most simplifications made by Pe'er & Ryde (2011), including instantaneous injection of photons and an outer boundary at infinity. One modification is that we relax the δ-function assumption of photon energy (Pe'er, 2008; Pe'er & Ryde, 2011), but introduce a more realistic co-moving blackbody spectrum.

We start with the formula of Pe'er & Ryde (2011) that calculates the specific flux:

$$\begin{aligned} F_\nu(\nu,t) &= \frac{N_0}{4\pi d_{\rm L}^2}\int\int P(r,\theta)k_{\rm B}T(r,u) \\ &\times \delta\left(t-\frac{ru}{\beta c}\right)\delta\left(\nu-\frac{k_{\rm B}T'(r)}{h\Gamma u}\right)dudr \end{aligned} \tag{2.1}$$

where N_0 is the impulsively injected number of photons at $t = 0$, $P(r,\theta)$ is the probability density function for the last scattering to occur at the radius r and to an angle θ, respectively, and the parameter

$$u = 1-\beta\cos\theta \tag{2.2}$$

contains the angular information.

For the probability density function $P(r,\theta)$, Pe'er & Ryde (2011) used two independent functions $P(r)$ (for the radial dimension) and $P(u)$ (for the angular dimension) to decompose $P(r,\theta)$ into $P(r,\theta) = P(r)\cdot P(r)$, where

$$P(r) = \frac{r_{\rm ph}}{r^2}e^{-\frac{r_{\rm ph}}{r}} \tag{2.3}$$

where $r_{\rm ph}$ is the classical photosphere radius ($\tau = 1$) at $\theta = 0$, and

$$P(u) = \frac{1}{2\Gamma^2 \beta u^2}. \tag{2.4}$$

On the other hand, the simulation result in Pe'er & Ryde (2011) indicated that $P(r)$ depends on angle and $P(u)$ also depends on radius. Beloborodov (2011) later introduced a two dimensional $P(r, \theta)$ function based on the assumption of outer boundary at infinity:

$$\begin{aligned} \frac{dP}{dr d\mu} &= \mathcal{D}^2 \frac{r_{\rm ph}}{4r^2} \left\{ \frac{3}{2} + \frac{1}{\pi} \arctan \left[\frac{1}{3} \left(\frac{r_{\rm ph}}{r} - \frac{r}{r_{\rm ph}} \right) \right] \right\} \\ & \exp \left[-\frac{r_{\rm ph}}{6r} \left(3 + \frac{1-\mu'}{1+\mu'} \right) \right], \end{aligned} \tag{2.5}$$

where $\mu' = cos\theta'$ is in the outflow comoving frame, $\mu = cos\theta$ is in the observer frame, and the Doppler factor is

$$\mathcal{D} = [\Gamma(1 - \beta \cos\theta)]^{-1} = (\Gamma u)^{-1}. \tag{2.6}$$

In this section and §2.3.2, we will use Eq.2.5 as $P(r, \theta)$ in Eq.2.1.

The last δ function in Eq.2.1 made the mono-energetic simplification for the photosphere photons. We consider a blackbody distribution of the photon energy and replace Eq.2.1 by a new equation

$$\begin{aligned} F_\nu(\nu, t) &= \frac{N_0}{4\pi d_{\rm L}^2} \int \int P(r, \mu) P(\nu, T) h\nu \\ &\times \delta \left(t - \frac{ru}{\beta c} \right) d\mu dr, \end{aligned} \tag{2.7}$$

where we have defined a new parameter

$$P(\nu, T) = \frac{n_\gamma(\nu, T)}{\int_0^\infty n_\gamma(\nu, T) d\nu} = \frac{n_\gamma(\nu, T)(hc)^3}{16\pi\zeta(3)(kT)^3}, \tag{2.8}$$

which is the probability function of a photon with frequence ν in a Plank distribution with a temperature T at the coordinate (r, θ) as observed by an observer located at $\theta = 0$, and

$$n_\gamma(\nu, T) = \frac{8\pi\nu^2}{c^3} \frac{1}{\exp(h\nu/kT) - 1} \tag{2.9}$$

is the specific photon number density at frequency ν for an observed temperature T. Here the mathematical relation

$$\int_0^\infty \frac{x^2 dx}{e^{\mathrm{x}} - 1} = 2\zeta(3) = 2 \times 1.202... \tag{2.10}$$

has been applied when calculating the integration $\int_0^\infty n_\gamma(\nu, T) d\nu$. Notice that here we have also adopted a blackbody function for the observed spectrum at any spatial point (r, θ). This is justified, since for any spatial point, the spectral shape is not modified from that in the co-moving frame, except that the entire spectrum is Doppler boosted by the local Doppler factor (Li & Sari, 2008). The global observed spectrum deviates from a blackbody due to different Doppler factors at different points. This effect is fully incorporated in our calculations.

The observer frame temperature at point (r, θ)

$$T(r, \theta) = \mathcal{D} T'(r) \tag{2.11}$$

depends on the angle through the Doppler factor and on the co-moving temperature. The co-moving frame temperature $T'(r)$ is more intrinsic, which depends on the radius r only. Its expression depends on the radius range (Mészáros & Rees, 2000), and can be calculated using the on-axis observed temperature divided by the on-axis Dopper

factor $\mathcal{D}(\theta = 0) = 2\Gamma$, i.e.

$$
\begin{aligned}
T'(r) &= T(r, \theta = 0)/(2\Gamma) \\
&= \begin{cases} T_0/(2\Gamma), & r < r_{\rm s} < r_{\rm ph}, \\ T_0(r/r_{\rm s})^{-2/3}/(2\Gamma), & r_{\rm s} < r < r_{\rm ph}, \\ T_0(r_{\rm ph}/r_{\rm s})^{-2/3}/(2\Gamma), & r_{\rm s} < r_{\rm ph} < r, \end{cases}
\end{aligned} \tag{2.12}
$$

where

$$T_0 = \left(\frac{L_0}{4\pi {r_0}^2 ca}\right)^{1/4} \tag{2.13}$$

is the temperature at the central engine, L_0 is the initial luminosity deposited at the central engine, and $r_0 = 10^7 r_{0,7}$ is the central engine radius. Notice that in order to satisfy our constant Γ assumption (§2.2.2), we have limited our study in the regime $r_s < r_{ph}$. Also for an easy treatment, in the above analytical model $T'(r)$ is taken as a broken power law function of r, whereas in reality it is a smoothly connected broken power law (Pe'er, 2008).

Since we mostly care about the shape of the spectrum, the normalization parameter N_0 is approximately taken as

$$N_0 = \frac{E_0}{kT_0}, \tag{2.14}$$

which denotes the rough total number of photons released at the central engine (assuming mono-energetic photon energy). By doing so, we have assumed that no additional emission or absorption processes occur as the photon-mediated outflow travels from the central engine to the photosphere, and that photons only undergo Thomson scattering with the total number conserved.

We integrate Eq. 2.7 to calculate the instantaneous spectra at different times. The

angle θ is integrated from 0 to $\pi/2$, which is wide enough to catch the relativistically beamed emission. The range of r is defined by the equal-arrival-time equation

$$t = \frac{ru}{\beta c}. \tag{2.15}$$

The results are presented in Fig.12. For an impulsive fireball as studied in this subsection, we calculate T_0 by taking $L_0 = 10^{52}$ erg s^{-1}, while adopt the impulsively injected total wind energy $E_0 = 10^{52}$ erg. This is to keep consistency with the continuous-wind calculations in the later subsections. Other parameters are adopted with the following values: dimensionless entropy $\eta = \Gamma = 300$, luminosity distance of the GRB $d_{\rm L} = 2 \times 10^{28}$ cm ($z \sim 1$), and the inner boundary of integration set to $r_0 = 10^7$ cm.

From Fig.12, we can see that under the assumptions adopted in this subsection, the on-axis, instantaneous photosphere spectrum evolves from a pure blackbody (early on) to a gradually flattened shape as the high-latitude emission becomes progressively dominant. Compared with the analytical results of Pe'er & Ryde (2011), our results show an exponential tail of blackbody emission instead of the flat spectrum $F_\nu \propto \nu^0$ extending all the way to high energies. Our results are however generally consistent with the numerical results of Pe'er & Ryde (2011).

2.3.2 Continuous wind with a constant wind luminosity and Lorentz factor

The next step is to study the observed instantaneous spectra for a continuous wind. For simplicity, we assume that the central engine wind has a constant luminosity and

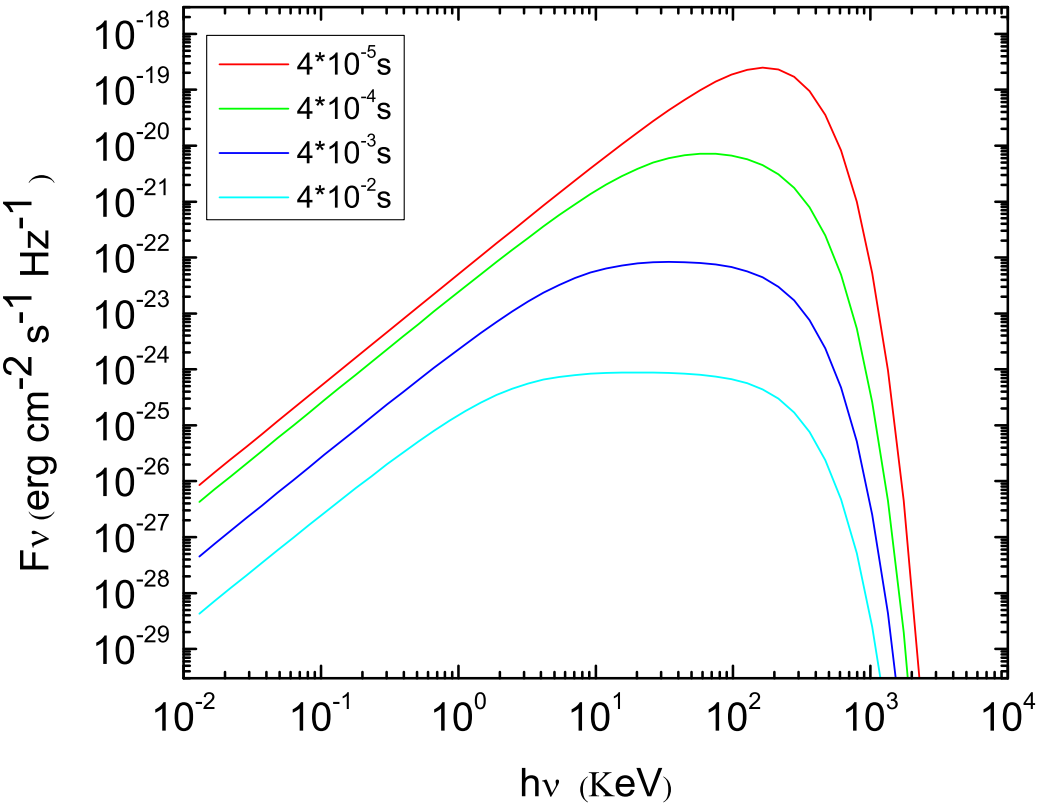

Figure 12 Instantaneous photosphere spectra for a fireball with impulsive injection of energy. The impulsively injected total energy is $E_0 = 10^{52}$ erg, the fireball temperature is calculated by taking $L_0 = 10^{52}$ erg s^{-1}, central engine radius $r_0 = 10^7$ cm, dimensionless entropy $\eta = \Gamma_0 = 300$, and luminosity distance $d_{\rm L} = 2 \times 10^{28}$ cm. Different colors represent different observational times. The spectra become progressively high-latitude dominated.

baryon loading rate, and hence, a constant Lorentz factor:

$$\begin{aligned} L_w(\hat{t}) &= L_0, \\ \dot{M}(\hat{t}) &= \dot{M}_0, \\ \eta(\hat{t}) &= \Gamma(\hat{t}) = \Gamma_0, \end{aligned} \tag{2.16}$$

where $\hat{t}$ denotes the central-engine time since the injection of the very first layer of the wind.

In order to calculate the emission from the entire wind, we dissect the wind into many thin layers, with each layer denoted by its injection time $\hat{t}$. Repeating the excise discussed in §2.3.1, we can write the contribution of specific flux at the observer time t for a layer ejected during the time interval from $\hat{t}$ to $\hat{t} + d\hat{t}$ (for $\hat{t} < t$)

$$\begin{aligned} \hat{F}_\nu(\nu, t, \hat{t}) &= \frac{\dot{N}_0(\hat{t})}{4\pi d_{\rm L}^2} \int\int P(r,\mu) P(\nu, T) h\nu \\ &\times \delta\left(t - \hat{t} - \frac{ru}{\beta c}\right) d\mu dr. \end{aligned} \tag{2.17}$$

The δ-function here takes into account the retardation effect for different layers ejected at different injection time $\hat{t}$. The parameter $\dot{N}_0(\hat{t})$ is the instantaneous injection rate of photons at the central engine time $\hat{t}$, and a rough normalization

$$\dot{N}_0(\hat{t}) = \frac{L_w(\hat{t})}{kT(\hat{t})} \tag{2.18}$$

is adopted. The calculation of $T(\hat{t})$ follows Eqs. (2.12) and (2.13), with L_0 replaced by $L_w(\hat{t})$. Notice that the parameter $\hat{F}_\nu$ has the dimension of specific flux over time.

The total observed instantaneous specific flux at t can be obtained by integrating $\hat{F}_\nu$ over all the layers, i.e.

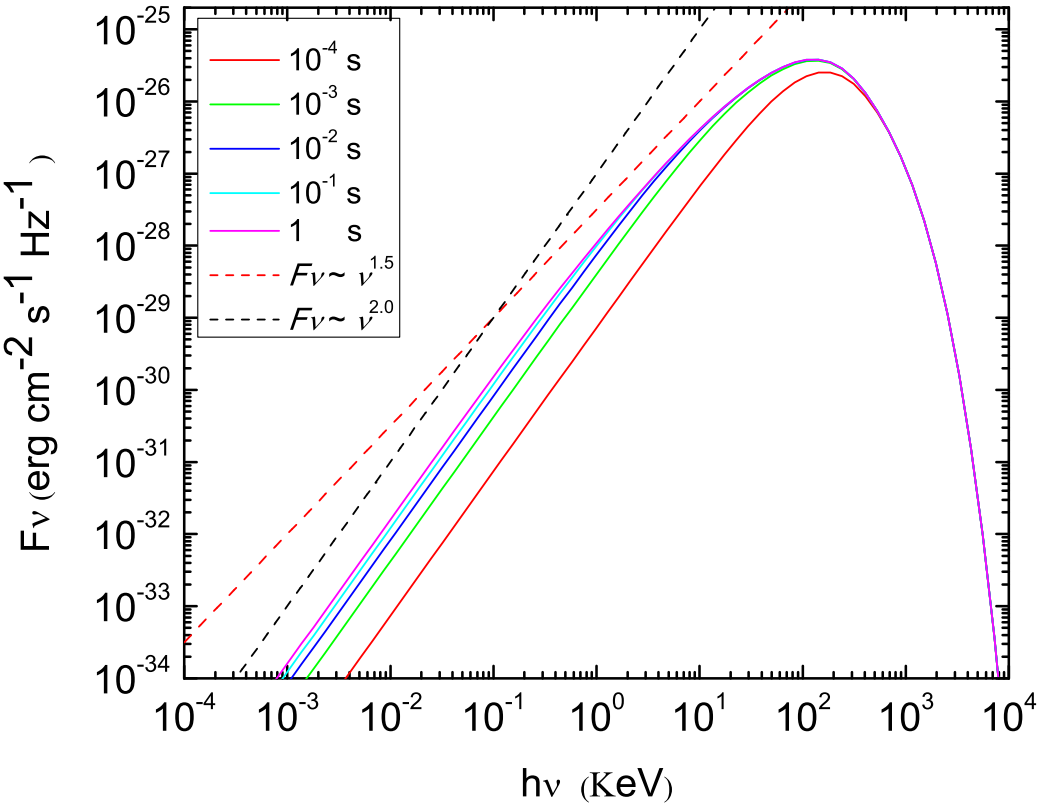

Figure 13 The instantaneous photosphere spectra of a continuous wind. The parameters are the same as Fig.12 except E_0 is not used and $L_w(\hat{t}) \equiv L_0 = 10^{52}$ erg s^{-1} is adopted. The two dashed lines are the reference lines for $F_\nu \propto \nu^2$ (black) and $F_\nu \propto \nu^{1.5}$ (red), respectively.

$$F_\nu(\nu, t) = \int_0^t \hat{F}_\nu(\nu, t, \hat{t}) d\hat{t}. \tag{2.19}$$

We study two cases in the following. In the first case, we assume that the central engine continuously injects an outflow with a constant luminosity during all the observation times (Fig.13). In the second case, we introduce shut-down of the central engine after a certain duration time (Fig.14 and Fig.15). All the parameters are the same as the ones adopted in §2.3.1, except E_0 is no longer used, and $L_w(\hat{t}) \equiv L_0 = 10^{52}$ erg s^{-1} has been adopted.

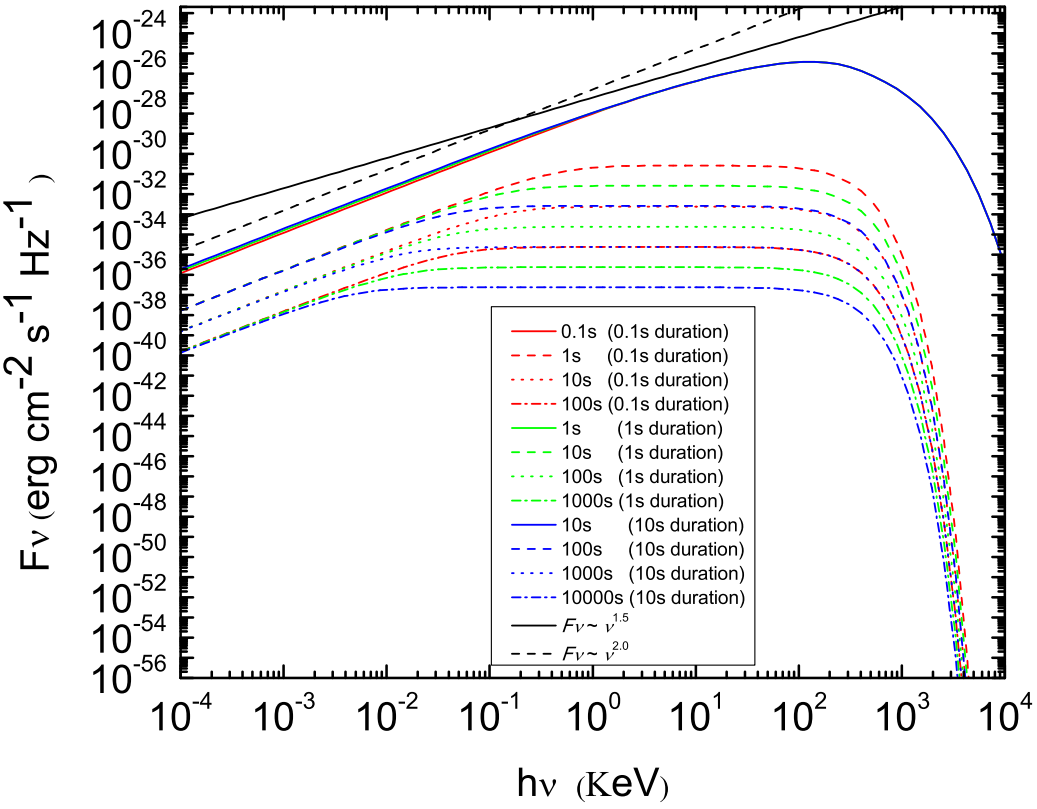

Figure 14 The instantaneous photosphere spectra of a continuous wind, which shuts down at a particular time. Parameters are same as Fig.13. Different color groups represent the spectra for different shut-down times: 0.1 s (red), 1 s (green) and 10 s (blue). For each group, four instantaneous spectra with different observation times are plotted: solid (end of continuous wind), dashed (one order of magnitude after), dotted (two orders) and dash-dotted (three orders). The two black lines are the reference lines for spectral indices being 2 and 1.5.

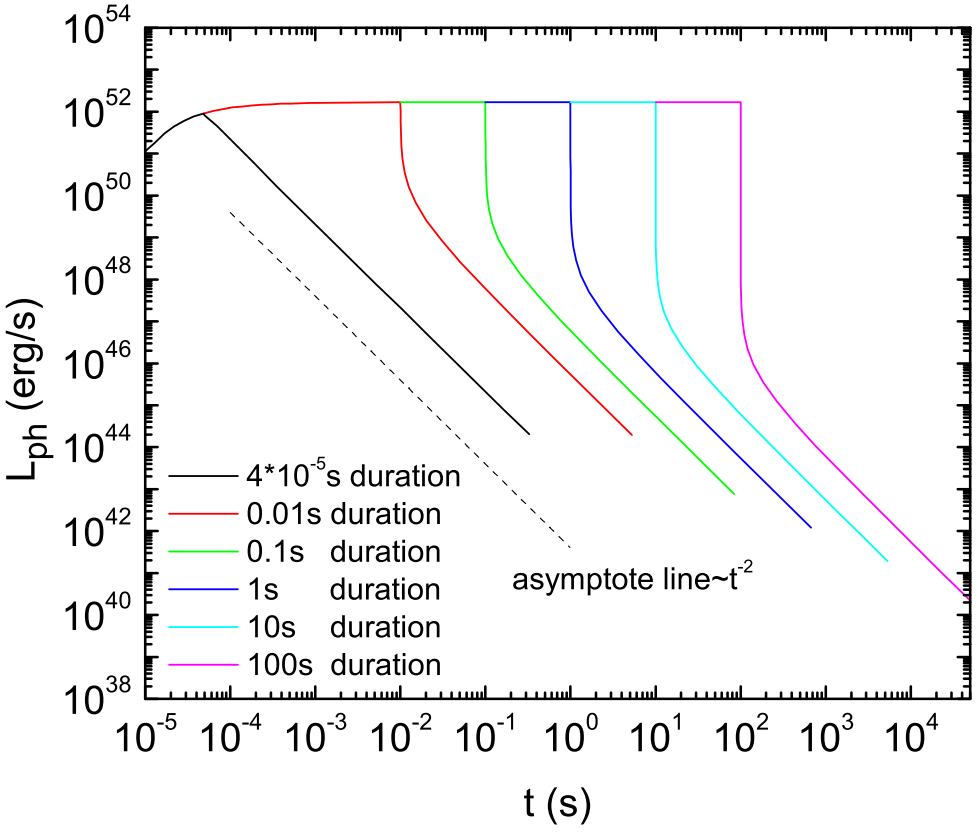

Figure 15 Photosphere luminosity light curves for continuous winds with abrupt shut-down of the central engine. Different colors represent different shut-down times. For the cases with duration longer than the characteristic duration ($t_{\rm N} \sim 4 \times 10^{-5}$ s), the light curves initially fall rapidly before entering the t^{-2} phase. The longer the central engine time, the more significant the rapid drop is.

Figure 13 presents the observed instantaneous photosphere spectra of a continuous wind with a constant luminosity and Lorentz factor. One can see several interesting features. The instantaneous spectrum is initially ($t = 10^{-4}$ s) blackbody-like with $F_\nu \propto \nu^2$ below the peak (Rayleigh-Jeans regime). Soon after, the spectrum below the peak starts to flatten, and a new segment with $F_\nu \propto \nu^{1.5}$ starts to merge below the peak. The reason for this softening can be understood from the results presented in Fig.12, which delineates the time evolution of instantaneous spectra of each layer. An old layer is high-latitude dominated, so that a more extended plateau with $\hat{F}_\nu \propto \nu^0$ spectral segment shows up. A relatively newer layer has a shorter plateau, and the newest layer has no plateau. The superposition of emission from all these layers give rise to relatively softer spectral segment. The spectral index of this new segment ($F_\nu \propto \nu^{1.5}$) is consistent with the result of Beloborodov (2010), who obtained a similar spectral index using a different method. Notice that in Fig.13 the absolute flux increases with time. This is because at early epochs, the outmost layer only reaches a certain r above which no photons are released. Given a simplistic probability function defined in Eq.2.3 or Eq.2.5, a good fraction of photons do not contribute to the observed flux. In the following (§2.3.3), we will give a more accurate treatment on this effect.

Figure 14 presents the instantaneous photosphere spectral evolution with the assumption that central engine shuts down after a certain duration. We calculate three different central engine durations: 0.1s (red group curves), 1s (green group curves) and 10s (blue group curves). For each case, we calculate four instantaneous spectra with different observational times: solid line (end of constant luminosity injection), dashed line (one order of magntitude in time after the injection phase), dotted line (two orders of magnitude after) and dash-dotted line (three orders of magnitude after). The results show that the shape of the spectrum become high-latitude dominated at later times, but early on there is a rapid falling phase. In order to fully reveal this

feature, we calculate the photosphere luminosity evolution with time (light curve) as shown in Fig.15. Our results show that the luminosity evolution depends on the duration of the central engine. Even though at late times the decaying slope of $L_{\rm ph}$ is t^{-2}, shortly after wind terminates, $L_{\rm ph}$ decays rapidly like free-fall[3]. The longer of the central engine duration, the more significant the initial rapid drop it is. Only when the duration becomes as short as a characteristic duration $t_{\rm N}$(Pe'er & Ryde, 2011) $\sim r_{ph}/(2\Gamma^2 c) \sim 4\times10^{-5}$s, does the rapid falling phase disappear (black curve in Fig.15. This feature is caused by the "initial time effect" for $\log-\log$ plots (see also Figure 3 of Zhang et al. (2006) in the case of afterglow emission). Previously Ryde & Pe'er (2009) analyzed the data from 56 long GRBs. They found that the light curves decay rate is universally around t^{-2}. They considered this as consistent with the prediction of the high latitude emission of the photosphere model. Our results in Fig.15 suggest that this interpretation is unlikely, since there is no steep decay phase (4 orders of magnitude drop in flux for a 1 s wind) observed.

2.3.3 Continuous wind with a constant wind luminosity, variable finite outer boundary

So far we have assumed that the outer boundary of the outflow is at infinity. For a constant luminosity wind, the optical depth at a certain position in the outflow is time independent. However, in real situations invoking a short, variable wind from a GRB, the outer boundary is time variable. As a result, the optical depth at a certain position in the outflow is time dependent and changes rapidly with time at early epochs due to the relativistic motion of the outflow, especially during the early phase of wind injection. Since the optical depth is one of the key factors to decide the photosphere probability function, the probability function also becomes

[3]Notice that the calculated photosphere luminosity slightly deviates from the input wind luminosity $L_0 = 10^{52}$ erg s^{-1}. This is caused by the inaccurate estimate of the normalization parameter $\dot{N}$ (Eq.(2.18).

time dependent. This also affects the observed photosphere temperature, and the observed E_p evolution in the photosphere model.

Technically, since our model is limited to the $r_{\rm ph} > r_{\rm s}$ case, in our calculation we keep track the evolution of $r_{\rm ph}$ and compare it with $r_{\rm s}$, to make sure the presented results are relevant ones when $r_{\rm ph} > r_{\rm s}$ is satisfied. The assumption of constant luminosity and Lorentz factor (Eq.2.16) is still adopted in the calculations.

2.3.3.1 Optical depth calculation

For a wind with boundary at infinity, the optical depth can be written as (Abramowicz et al., 1991; Beloborodov, 2011):

$$\begin{aligned} \tau &= \int_{r_1}^{\infty} d\tau \\ &= \int_{r_1}^{\infty} \mathcal{D}^{-1}\sigma_{\rm T} n' ds \\ &= \int_{r_1}^{\infty} \mathcal{D}^{-1}\sigma_{\rm T} n' dr/\cos\theta, \end{aligned} \tag{2.20}$$

where r_1 is the photon emission radius, ds and dr are along the ray direction and radial direction, respectively, $\mathcal{D} = [\Gamma(1-\beta\mu)]^{-1}$ is the doppler factor and

$$n' = \frac{\dot{M}}{4\pi m_{\rm p}\beta c\Gamma r^2} \tag{2.21}$$

is the number density in the comoving frame. Since the number density in rest frame is

$$n = \Gamma n', \tag{2.22}$$

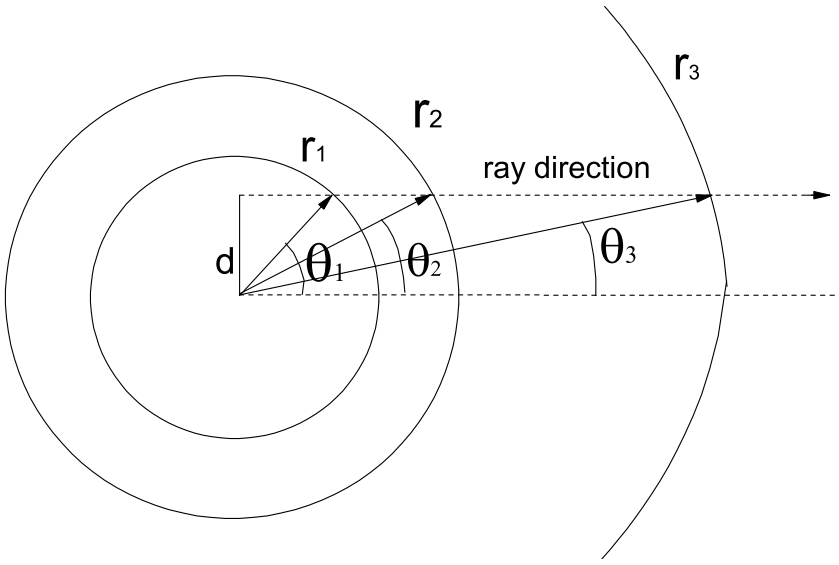

Figure 16 Geometric relations of the catch-up process.

the above equation can be written as

$$\begin{aligned} \tau &= \int_{r_1}^{\infty} \Gamma(1-\beta\mu)\sigma_{\rm T} n' dr/\cos\theta \\ &= \int_{r_1}^{\infty} (1-\beta\mu)\sigma_{\rm T} n dr/\cos\theta. \end{aligned} \tag{2.23}$$

For an finite outer boundary we are considering, the upper limit of integration has to be modified to a finite value. Assuming that a photon is emitted at a position (r_1, θ_1), ahead of which there is a shell of materials extending to an outer boundary at r_2 (Fig.16). The light ray intersects with the out boundary of the shell at (r_2, θ_2). Since the shell is also expanding near speed of light, the location as the photon catches up with the front of the shell would be at (r_3, θ_3). The optical depth should then be

calculated by

$$\begin{aligned} \tau &= \int_{r_1}^{r_3} d\tau \\ &= \int_{r_1}^{r_3} (1-\beta\mu)\sigma_{\rm T} n dr/\cos\theta, \end{aligned} \tag{2.24}$$

where r_3 can be solved through the equations

$$r_3\cos\theta_3 - r_1\cos\theta_1 = c\Delta t_{\rm c}, \tag{2.25}$$

and

$$r_3 - r_2 = \beta c\Delta t_{\rm c}, \tag{2.26}$$

where $\Delta t_{\rm c}$ is the time for the photons emitted from (r_1, θ_1) to catch up with the outer boundary at (r_3, θ_3). Meanwhile, a simple geometrical formula gives

$$d = r_1\sin\theta_1 = r_2\sin\theta_2 = r_3\sin\theta_3, \tag{2.27}$$

where d is the distance between the line of ray and the axis of the explosion along line-of-sight (Fig.16).

These equations can be solved in two different ways. First, we can calculate the catching-up outer boundary position r_3 based on the initial value of r_1, θ_1 and r_2. The solution is:

$$r_3 = \Gamma^2(-\mathcal{A} + \sqrt{\mathcal{A}^2 - (\mathcal{A}^2 + \beta^2 d^2)/\Gamma^2}, \tag{2.28}$$

where $\mathcal{A} = \beta r_1\cos\theta_1 - r_2$. Here only one physical solution of r_3 (two mathematic solutions) is kept.

Second, one can solve for r_2 using r_3, i.e.

$$\begin{aligned} r_2 &= r_3(1-\beta\cos\theta_3)+\beta r_1\cos\theta_1, \\ &= r_3(1-\beta\sqrt{1-\frac{d^2}{{r_3}^2}})+\beta r_1\cos\theta_1, \\ &= r_3-\beta\sqrt{{r_3}^2-d^2}+\beta r_1\cos\theta_1. \end{aligned} \tag{2.29}$$

By employing $r_2 = r_1 + \beta c\delta\hat{t}$, one can find out $\delta\hat{t}$, which is the emission time difference between layers at position r_2 and r_1. This second approach is applied during integration when a variable wind luminosity is introduced (see details in §2.3.4).

2.3.3.2 Modified probability function

With a finite outer boundary, one needs to modify the probability function of last scattering from the simple form with the infinite boundary (Eqs.(2.3-2.5)). In this sub-section we develop a general method to calculate the probability function.

We first recall a simple radiation transfer model: $I = I_0 e^{-\tau}$, where I_0 is the initial radiation intensity and I is the observed intensity after absorbtion (scattering in the current case) with optical depth τ. So $I/I_0 = e^{-\tau}$ (which is $\sim \tau$ when $\tau \ll 1$) is the fraction of the remaining radiation flux, which would stand for the probability of not being scattered. The factor $1 - I/I_0 = 1 - e^{-\tau}$, on the other hand, stands for the probability of being scattered.

The probability function for last scattering can be calculated in three steps. First, the probability for a photon being scattered from radius r to $r + dr$ should be

$$P_{\rm r}dr \propto d\tau = \sigma_{\rm T} n(r) dr. \tag{2.30}$$

Second, the probability for the photon to be scattered to the observer's direction can

be expressed as

$$P_\Omega d\Omega \propto -\frac{\mathcal{D}^2 d\mu d\phi}{4\pi} = \frac{\mathcal{D}^2 d\Omega}{4\pi}. \tag{2.31}$$

Here we have noticed that in the comoving frame of the flow, the probability to have the photon scattered to any direction is random, so that

$$P'_{\Omega'} d\Omega' \propto \frac{d\Omega'}{4\pi} = \frac{\sin\theta' d\theta' d\phi'}{4\pi} = -\frac{d\mu' d\phi'}{4\pi}, \tag{2.32}$$

$P'_{\Omega'} d\Omega' = P_\Omega d\Omega$, $d\mu' = \mathcal{D}^2 d\mu$, and $d\phi' = d\phi$. Finally, the probability for this scattered photon not being scattered again is $e^{-\tau}$. Putting everything together, one can write

$$P(r,\Omega) = \frac{\sigma_{\rm T} n \mathcal{D}^2 e^{-\tau({\rm r},\mu,{\rm r_{out}})}}{4\pi A} \tag{2.33}$$

where the normalization factor is

$$\begin{aligned} A &= \int\int P(r,\Omega) dr d\Omega \\ &= \int_{\rm r_{min}}^{\rm r_{max}} \int_0^1 \int_0^{2\pi} \sigma_{\rm T} n \frac{\mathcal{D}^2}{4\pi} e^{-\tau({\rm r},\mu,{\rm r_{out}})} dr d\mu d\phi \\ &= \int_{\rm r_{min}}^{\rm r_{max}} \int_0^1 \sigma_{\rm T} n \frac{\mathcal{D}^2}{2} e^{-\tau({\rm r},\mu,{\rm r_{out}})} dr d\mu \ . \end{aligned} \tag{2.34}$$

Here the function $\tau(r,\mu,r_{\rm out})$ is a function depending on r and μ, and the outer boundary $r_{\rm out}$ of the outflow at the time when the photon crosses the ejecta. It is r-dependent, and $\hat{t}$-dependent. The relation between r and $r_{\rm out}$ is the same as r_1 and r_3 discussed above (§2.3.3.1). Since this function is rapidly evolving with time, the probability function (Eq.(2.33)) is also rapidly evolving.

In the normalization function (Eq.(2.34)), the integration limits $r_{\rm min}$ and $r_{\rm max}$ should be 0 and $+\infty$, respectively. In reality, we take $r_{\rm min} \sim r_0 = 10^7$ cm, and $r_{\rm max}$ a large enough number (e.g. 5×10^{17} cm). Since the probabilities at very small and very large distances are both very small. The actual numerical values of the two limits

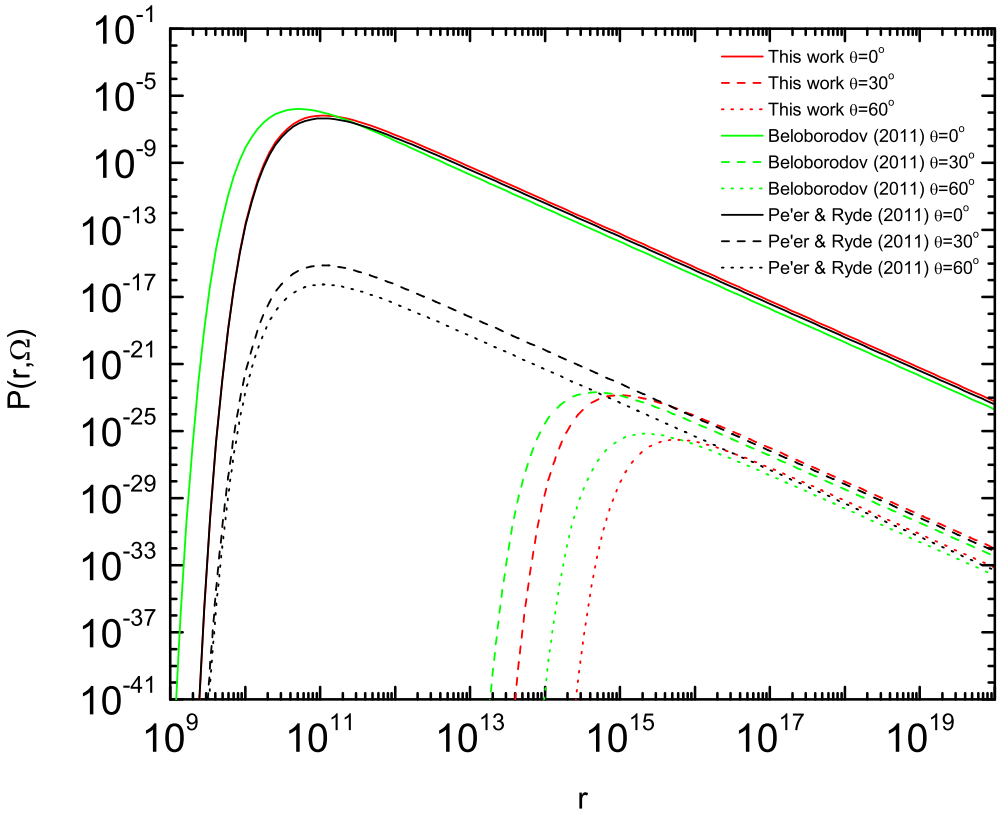

Figure 17 A comparison of the probability function $P(r, \Omega)$ between this work and those of Pe'er & Ryde (2011) and Beloborodov (2011).

essentially do not affect the calculation results.

In Fig.17, we compare our probability function in the infinite outer boundary limit with those of Pe'er & Ryde (2011) and Beloborodov (2011). Our results agree with Pe'er & Ryde (2011) in the small angle limit ($\theta = 0$), and are more consistent with that of Beloborodov (2011) in the large angle limit ($\theta = 30^{\rm o}, 60^{\rm o}$).

2.3.3.3 Putting pieces together

The specific flux at time t for a layer ejected at the time $\hat{t}$ can be expressed as

$$\begin{aligned}\hat{F}_\nu(\nu,t,\hat{t}) &= \frac{\dot{N}_0(\hat{t})}{4\pi d_{\rm L}^2}\int\int \hat{P}(r,\Omega)P(\nu,T)h\nu \\ &\quad\times\delta\left(t-\hat{t}-\left(\frac{ru}{\beta c}-t_0\right)\right)d\Omega dr. \end{aligned} \tag{2.35}$$

Compared with the calculation in §2.3.2 (Eq.(2.17)), this expression has two improvements. First, we have introduced $t_0 = \frac{r_0}{\beta c(1+\beta)\Gamma^2}$ to reflect that the wind is ejected from a central engine with radius $r_0 = 10^7$ cm (instead of $r_0 = 0$). Second, since $P(r,\Omega)$ is no longer a universal function, we express it as $\hat{P}(r,\Omega)$ to specify that it is related to the layer ejected at $\hat{t}$. The expanded full expression of $\hat{F}_\nu(\nu,t,\hat{t})$ (Eq.(2.35)) is presented in the Appendix.

Again the instantaneous specific flux can be calculated by integrating the contributions from all layers

$$F_{\nu,}(\nu,t) = \int_0^t \hat{F}_\nu(\nu,t,\hat{t})d\hat{t}. \tag{2.36}$$

Finally, one can integrate over a time interval $[\mathrm{t_1},\mathrm{t_2}]$ to get a time integral spectrum, which is what is observed:

$$F_\nu(\nu,t_1\rightarrow t_2) = \int_{\mathrm{t_1}}^{\mathrm{t_2}} F_\nu(\nu,t)\ dt. \tag{2.37}$$

2.3.3.4 Results

Here, we present the calculation results for a constant wind luminosity with a variable outer boundary. The input parameters are: constant wind luminosity $L_{\rm w} = 10^{52}$ erg s^{-1}, constant dimensionless entropy $\eta(\hat{t}) = \Gamma(\hat{t}) = \Gamma_0 = 300$, luminosity distance of the central engine $d_{\rm L} = 2\times10^{28}$ cm ($z\sim1$), and central engine radius $r_0 = 10^7$ cm.

Since our spectral calculation is valid for $r_{ph} > r_{\rm s}$, we need to closely track the location of r_{ph}. Figure 18 shows the numerical results of $r_{\rm ph}$ evolution ($L_w = 10^{52}$ erg s^{-1} and $\Gamma_0 = 300$). It shows that before $10^{-3}s$, $r_{\rm ph}$ increases rapidly, while after $10^{-3}s$, r_{ph} is nearly constant around 2×10^{11} cm. Since $r_{\rm s} = \eta r_0 = 3 \times 10^9$ cm, the condition $r_{\rm ph} > r_{\rm s}$ is easily satisfied from very early time. We choose seven observer times, $10^{-6}, 10^{-5}, 10^{-3}, 0.5, 2.3, 10, 100$ seconds, to calculate the instantaneous spectra. The results are shown in Figure 19. We find that early on ($10^{-6} - 10^{-3}$ s, the spectra evolve rapidly. In particular, the temperature displays a strong hard-to-soft evolution. This is because initially the photosphere radius is closer in due to the less opacity early on (Fig.18). However, such a phase is too short to have an observational consequence. After 10^{-3} s, the photosphere radius approaches the sympototic value, so is the photosphere temperature. As a result, the last four spectra are nearly identical with minor differences in the low energy regime. In other words, there is essentially no temporal evolution with time. For a constant initial wind luminosity, the density and probability function for different layers are essentially the same. As a result, given a same r_{ph} the spectral behavior is rather similar. From the results, we find that the spectral index from 3 keV to the peak is modified from 2 to ~ 1.5. This is again due to the superposition from the older layers' high latitude contribution, as already analyzed in §2.3.2. Compared with the results presented in §2.3.2 (which has an outer boundary at infinity), the more sophisticated method here can trace the evolution of the photosphere radius and probability function for a dynamic, finite outer boundary. For the constant luminosity case discussed in this sub-section, the finite boundary treatment makes a noticeable difference only at very early times ($t < 10^{-3}s$). The difference is more obvious for a variable luminosity wind, as we discuss next.

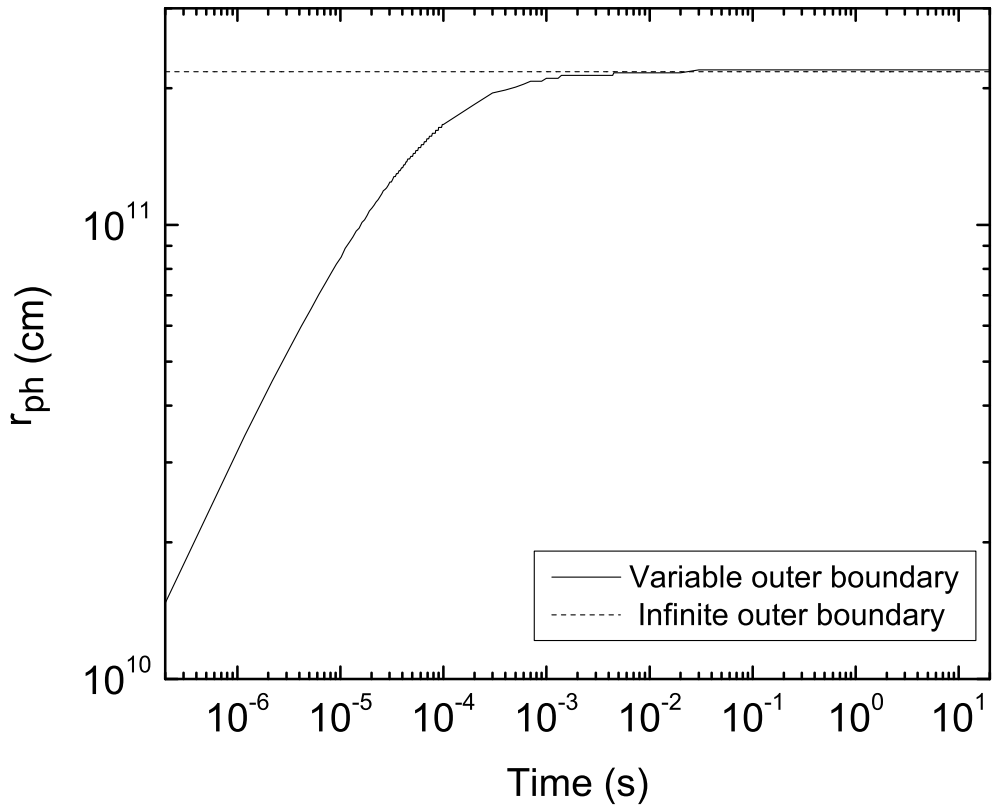

Figure 18 The evolution of r_{ph} as a function of observer time for a constant luminosity central engine wind. The dotted line is the asymptotic solution for an outer boundary at infinity.

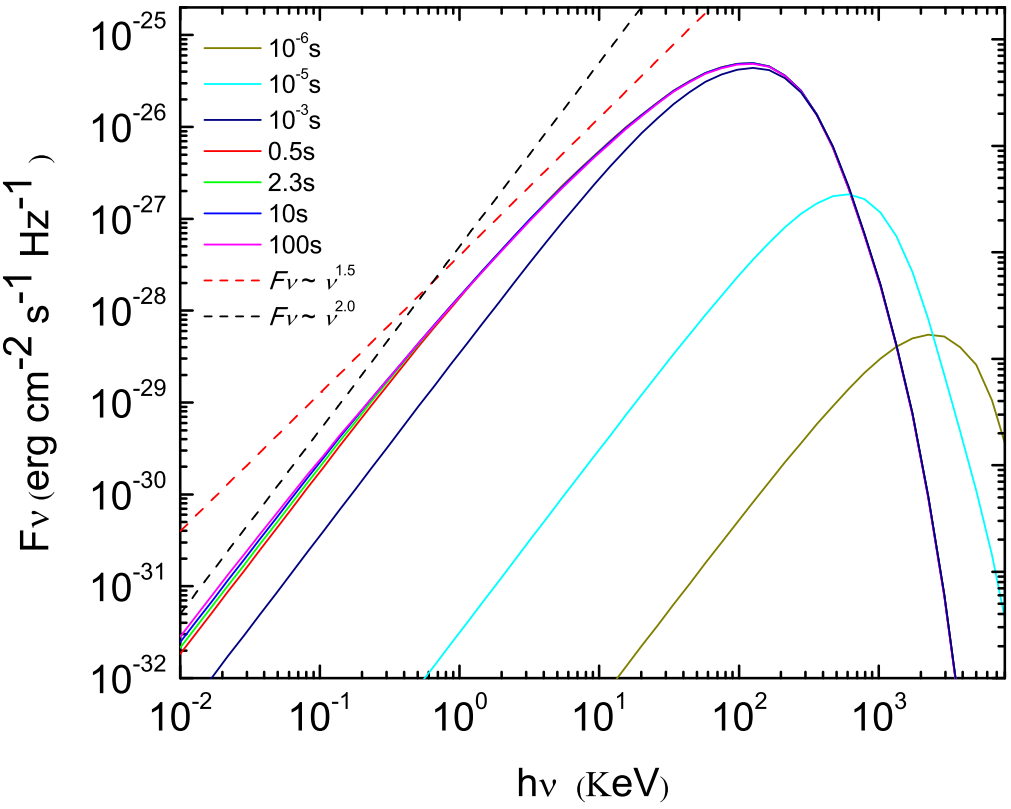

Figure 19 The instantaneous spectra for a constant luminosity wind with a variable outer boundary. Different colors stand for different epochs: 10^{-6} s (dark yellow), 10^{-5} s (cyan), 10^{-3} s (navy), 0.5 s (red), 2.3 s (green), 10 s (blue), and 100 s (magenta).

2.3.4 Variable wind luminosity

In a real GRB, wind luminosity varies rapidly with time. Unlike the constant luminosity/Γ model which preserves a $n \propto r^{-2}$ density profile of the wind, the density profile changes rapidly with time depending on the time history of luminosity, $L_w(\hat{t})$, and baryon loading, $\dot{M}(\hat{t})$. The integration for optical depth (Eq.(2.24)) becomes more complicated. In this sub-section, we develop a method to handle this problem. For simplicity, we assume a power law form of the time history, and assume a constant $\Gamma = \eta = L_w(\hat{t})/\dot{M}(\hat{t})c^2$ throughout.

2.3.4.1 Luminosity and baryon-loading history

We approximate a GRB pulse as broken power law in luminosity, with rising and decaying indices as a_r and a_d, respectively, with a peak $L_{w,p}$ at $\hat{t}_p$. The luminosity history in the rising phase ($\hat{t} < \hat{t}_p$) can be written as

$$\log L_{\rm w}(\hat{t}) = a_r \log \hat{t} + b_r, \tag{2.38}$$

while that in the decaying phase ($\hat{t} > \hat{t}_p$) can be written as

$$\log L_{\rm w}(\hat{t}) = a_d \log \hat{t} + b_d, \tag{2.39}$$

where $b_r = \log L_{w,p} - a_r \log \hat{t}_p$ and $b_d = \log L_{w,p} - a_d \log \hat{t}_p$ are normalization parameters of the two power law segments.

2.3.4.2 Complications in the catch-up process

For the constant L_w and $\dot{M}$ wind case as discussed in §2.3.3, since the n profile does not evolve with time, the integration of (2.24) from r_1 (photon emission radius) to r_3 (the radius where the photon escape the wind) is straightforward (see Fig.16 and §2.3.3.1 for detailed discussion). One can apply Eq.(2.28) to directly solve for

r_3 given any r_2, and the final optical depth is defined by the maximum catching up radius $r_{3,\rm M}$ (which is also $r_{\rm out}$ discussed in §2.3.3.2) corresponding to the maximum $r_{2,\rm M}$ of the wind at the time when the photon is emitted at r_1.

In the variable wind case discussed here, since the n profile is variable with time, one needs to precisely determine n at any r_3 value in the range of $(r_1, r_{3,\rm M})$. To do so, one needs to find out the corresponding r_2 of each r_3 using Eq.(2.29). Then one can connect r_2 with a certain central engine time $\hat{t}$, and hence, its baryon loading rate $\dot{M}(\hat{t})$, which defines the density profile, and hence, the relevant n at that r_3.

Solving for Eq.(2.29), we find an interesting fact (Fig.20): at low latitudes with respect to the line-of-sight (small θ_1), r_2 is always larger than r_1. This means that the emitted photons always catch up layers ejected earlier. However, at large latitudes (large θ_1), r_2 can be smaller than r_1. This means that photons emitted at a certain epoch would initially interact with the layers ejected later, so that it would see an even higher optical depth during propagation. This does not mean that the late ejected materials move with a superluminal velocity. A photon is caught up with by the electrons ejected later due to a geometric effect: electrons move in a hypotenuse "short-cut", even though their bulk motion velocity is sub-luminal (Fig.16).

For a large-angle geometry when the reverse of r_2 and r_1 happens, the relationship between r_2 and r_3 shows an interesting feature. Performing derivative to equation (2.29), one gets

$$\frac{dr_2}{dr_3} = 1 - \frac{\beta r_3}{\sqrt{{r_3}^2 - d^2}} = 1 - \frac{\beta}{\cos\theta_3}. \tag{2.40}$$

Setting $dr_2/dr_3 = 0$, one gets a critical catch-up point $\cos\theta_3 = \beta$, or $\sin\theta_3 = 1/\Gamma_0$. In the early stages, θ_3 is relatively large, so that $\sin\theta_3 > 1/\Gamma_0$ and $dr_2/dr_3 < 0$ are satisfied. As a result, initially r_2 is smaller than r_1 (e.g. $\sim 10^7$ cm), and r_2 decreases when r_3 increases. After passing the critical point (Eq.2.40), dr_2/dr_3 becomes positive.

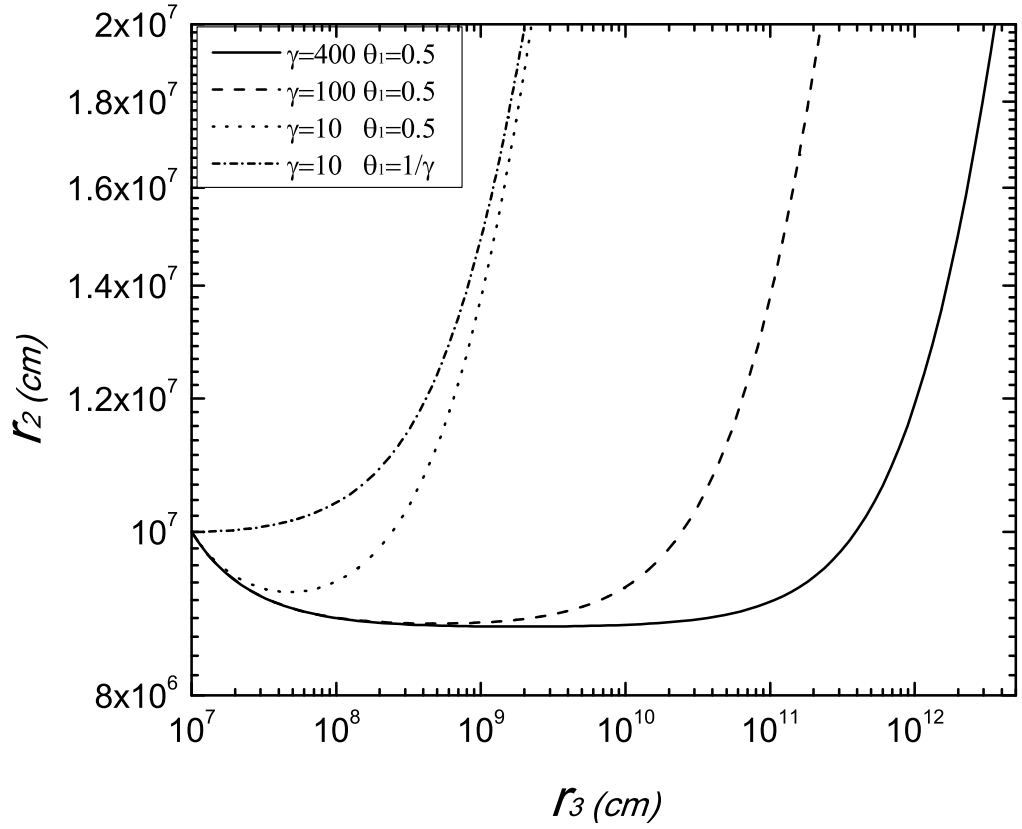

Figure 20 The relationship between r_2 and r_3 based on Equation (2.29). The solid, dashed, and dotted lines have the same initial angle $\theta_1 = 0.5$ but different Lorentz factors Γ_0 =400, 100 and 10. The dash-dotted line corresponds to the case of $\theta_1 = 1/\Gamma_0$ with $\Gamma_0 = 10$.

The photon starts to overtake the outflow layers and eventually escape the wind. If the initial angle θ_1 is small enough from the beginning, i.e. $\sin\theta_1 < 1/\Gamma_0$ is satisfied from the beginning, r_2 would increase with r_3 all the time. In Figure (20), we show four different cases of $r_2 - r_3$ evolution. The solid, dashed, and dotted lines have the same initial angle $\theta_1 = 0.5$ but with different Lorentz factors. The dash-dotted line corresponds to the critical case $\theta_1 = 1/\Gamma_0$.

2.3.4.3 Optical depth calculation

With the above preparation, one can calculate optical depth of a photon in a variable-luminosity wind. Figure 21 shows the spacial distribution of wind luminosity at an instant t in the observer frame. The layers ejected at an earlier epochs move in the front, so the spacial distribution is essentially a reversed temporal distribution. We have assumed a constant Lorentz factor in all layers so that the temporal profile does not evolve with time other than globally streaming forward.

We calculate the optical depth of a photon emitted from a layer ejected at the central engine time $\hat{t}$, which has an age of $t - \hat{t}$ at the observer time t. The radius of the layer is defined as r_1 (or more precisely $r_1(\hat{t})$). We discuss two cases in Fig.21: "Case 1" corresponds to the early stage when the photon is emitted during the rising phase of the pulse, while "Case 2" corresponds to the late stage when the photon is emitted during the falling phase. In both cases, the location of the layer emitted at the peak time $\hat{t}$ is denoted as r_p.

At the time t when a photon is emitted at $r_1(\hat{t})$, all the layers emitted before $\hat{t}$ are ahead of r_1, and the maximum radius $r_{2,\rm M}$ is the first layer ejected at $\hat{t} = 0$. The photon will over-take this layer at a much larger radius $r_{3,\rm M}$. In order to calculate the optical depth of the photon τ, one needs to integrate Eq.(2.24) from r_1 to $r_{3,\rm M}$. For any $r \in (r_1, r_{3,\rm M})$ (r is effectively r_3), the density $n(r)$ is defined by its corresponding r_2, which is related to $\dot{M}(\hat{t}_2)$ at the time

$$\hat{t}_2 = \frac{r_{2,\rm M} - r_2}{\beta c}, \tag{2.41}$$

when the layer associated with r_2 was ejected. One therefore needs to solve for r_2 using Eq.(2.29) for every step in r (i.e. r_3).

In view of the complicated catch-up process discussed in §2.3.4.2, there are three possibilities for each case (Fig.21). For Case 1, one has $r_p < r_1 < r_2$, $r_p < r_2 < r_1$,

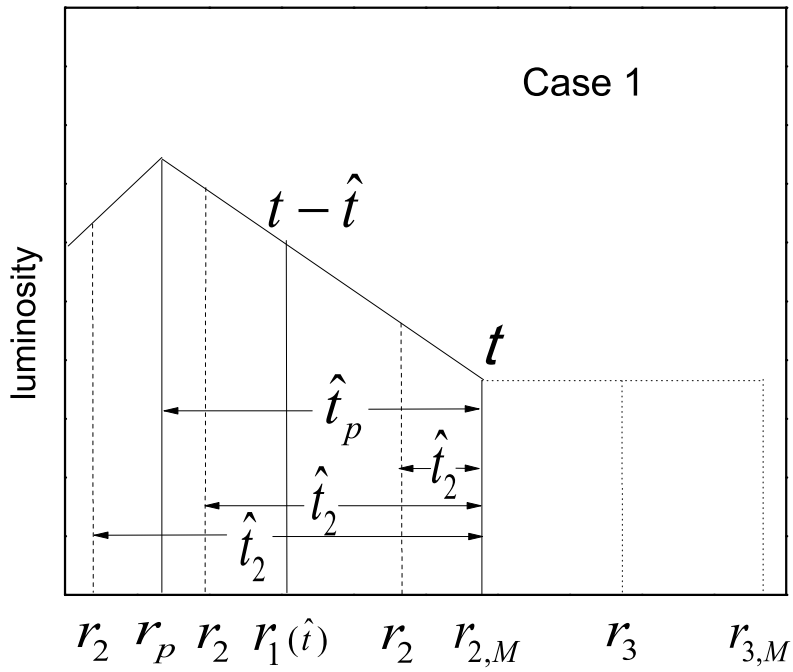

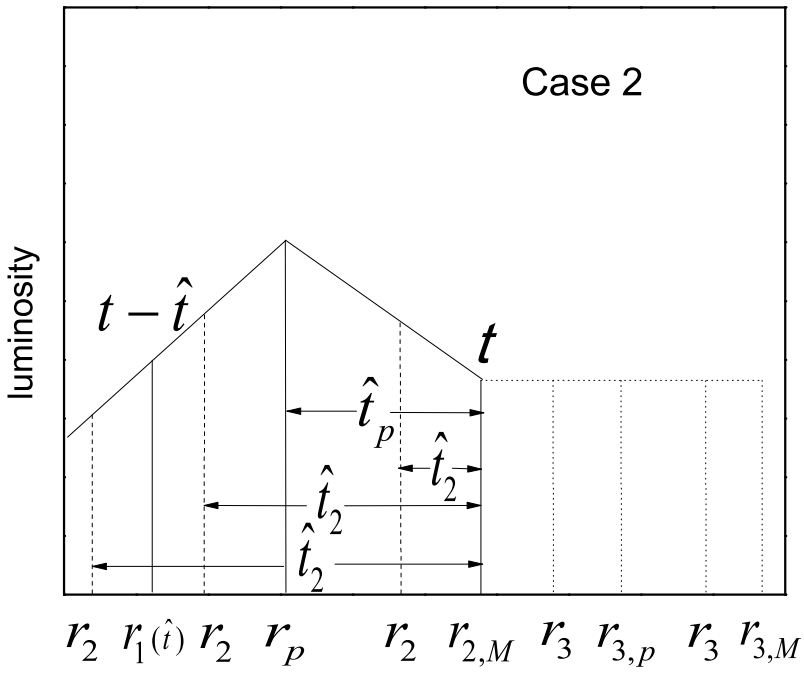

Figure 21 Instantaneous spacial structure of the wind luminosity as well as typical radii invoked to calculate optical depth.

or $r_2 < r_p < r_1$. The wind luminosity at $\hat{t}_2$ is defined by Eq.(2.38) for the first two cases, and by Eq.(2.39) for the last case. For Case 2, one has $r_1 < r_p < r_2$, $r_1 < r_2 < r_p$, or $r_2 < r_1 < r_p$. The wind luminosity at $\hat{t}_2$ is defined by Eq.(2.38) for the first case, and by Eq.(2.39) for the last two cases. From $L_w(\hat{t}_2)$ one can calculate $\dot{M}(\hat{t}_2) = L_w(\hat{t}_2)/\eta c^2$ given the constant η value, which can be used to calculate the density n using Equations (2.21) and (2.22). One can then complete integration to calculate the optical depth τ for any coordinate (r, θ). The photosphere radius r_{ph}^{θ} at any angle θ is defined by the condition

$$\tau(r_{ph}^{\theta}, \theta) = \int_{r_{\rm ph}}^{r_{\rm 3,M}} (1 - \beta\cos\theta)\sigma_{\rm T} n dr / \cos\theta = 1. \tag{2.42}$$

And the traditional photosphere radius is defined as $r_{ph} = r_{ph}^{\theta=0}$.

2.3.4.4 Results

We perform calculations for several different luminosity profiles. We fix $L_{w,p} = 10^{52}$ erg s^{-1}, $\hat{t}_p = 2.4$ s, $\eta = \Gamma_0 = 300$, $r_0 = 10^7$ cm, and $d_{\rm L} = 2 \times 10^{28}$ cm (effectively $z \sim 1$), and investigate six different luminosity profiles with $(a_r, a_d) = (+0.75, -1)$, $(+0.75, -2)$, $(+0.75, -5)$, $(+2, -1)$, $(+2, -2)$, $(+2, -5)$, respectively. Analytically, the on-axis ($\theta = 0$) photosphere radius (Mészáros & Rees, 2000)

$$r_{ph} = \frac{L_w \sigma_{\rm T}}{4\pi m_p c^3 \eta^3} \simeq 3.7 \times 10^{11}\ {\rm cm} L_{\rm w,52} \eta_{2.5}^{-3} \tag{2.43}$$

follows the luminosity profile $L_w(\hat{t})$ for a constant η, so $r_{ph}(\hat{t})$ should follow the same temporal profile as $L_w(\hat{t})$. We numerically reproduced this for a variable luminosity wind, with a slight deviation only at very early epochs ($\hat{t} < 10^{-3}$ s. The satuation radius is $r_s = \eta r_0 = 3 \times 10^9$ cm $(\eta/300)$. To assure $r_{ph} > r_s$, we choose the following observed epochs to calculate the instantaneous spectra: $t = 0.5$ s, 2.3 s before $\hat{t}_p = 2.4$ s, and $t = 2.5$ s, 4 s, and 10 s after $\hat{t}_p$. For $a_d = -5$ case, the last epoch ($t = 10$ s)

already violates the $r_{ph} > r_s$ condition, so we do not include it in the calculation.

Figure 22 shows the calculated instantaneous spectra, each panel displaying results for a luminosity profile. For each panel, different colors show different epochs. We can see that during the rising phase ($t = 0.5, 2.3$ s) the resulting spectra are very similar to the cases for a constant luminosity (Fig.19), i.e. the spectral slope is modified from Rayleigh-Jeans (2) to 1.5, mainly due to high-latitude contribution. During the decay phase ($t = 2.5, 4, 10$ s), the spectral index below E_p is somewhat shallower. This is because the high-latitude emission is more dominant since it comes from the layers that have higher luminosities. The steeper the decay phase, the more significant the high-latitude effect is.

In Figure 23, we compare the resulting spectra for different Γ_0. We fix $a_r = +0.75$, and vary a_d for three values -1, -2, -5. For each set of luminosity profile, we compare the resulting spectra for $\Gamma_0 = 300$ (solid curves) and $\Gamma_0 = 150$ (dashed curves). A smaller Γ_0 corresponds to a larger photosphere radius (Eq.(2.43)) and a lower photosphere temperature. A larger photosphere also gives a more significant high-latitude effect, which is reflected from the somewhat shallower spectral index below E_p during the decay phase, especially when a_d is steep.

Figure 24 shows the time integrated spectra. we choose 0.5 s as time bin for integration. For a same η and r_0, the instantaneous spectra do not evolve significantly. As a result, the time-integrated spectra are not much different from the instantaneous ones.

We also consider the case when the variable luminosity central engine wind ceases abruptly. Still keeping the same parameters, but make the wind abruptly cease at $\hat{t}_p = 2.4$ s, the calculation spectra are presented in Fig.25. It is seen that at $t > \hat{t}_p$, a progressively more prominent plateau develops, similar to the results presented in Fig.14.

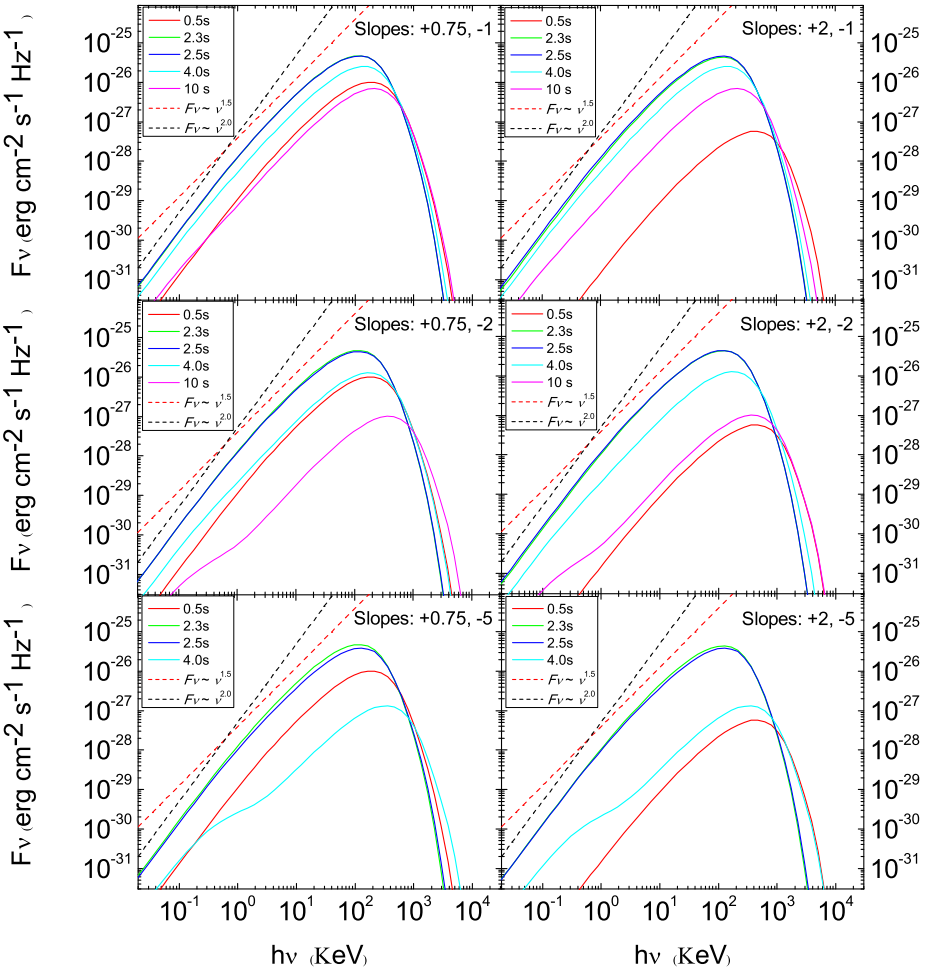

Figure 22 The instantaneous photosphere spectra of winds with variable luminosity. A constant $\Gamma_0 = 300$ and $d_{\rm L} = 2 \times 10^{28}$ cm, a peak time $\hat{t}_p = 2.4$ s, and a peak luminosity $L_{w,p} = 10^{52}$ erg s^{-1} are adopted for all cases. Different panels show different luminosity histories, and the temporal rising and decaying indices (slopes) are marked in each panel. For each panel, the spectra are calculated at the following times: 0.5 s (red), 2.3 s (green), 2.5 s (blue), 4 s(cyan), and 10 s (magenta). Two reference lines for spectral indices 1.5 (red dashed line) and 2 (black dashed line) are also drawn.

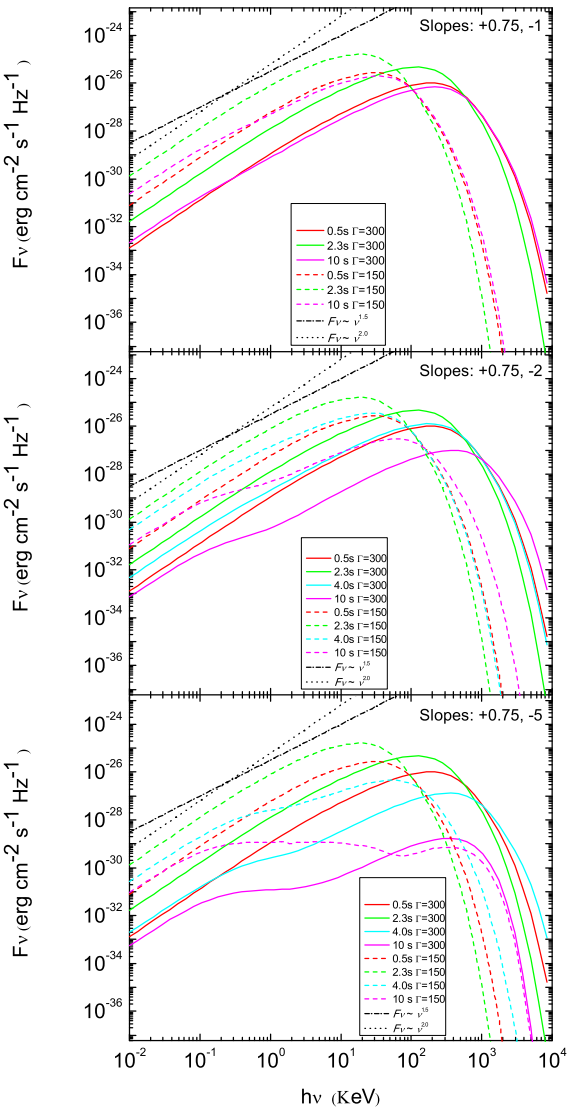

Figure 23 A comparison of instantaneous photosphere spectra for different Lorentz factors: $\Gamma_0 = 150$ (dashed) and 300 (solid). Other notations are the same as Fig.22.

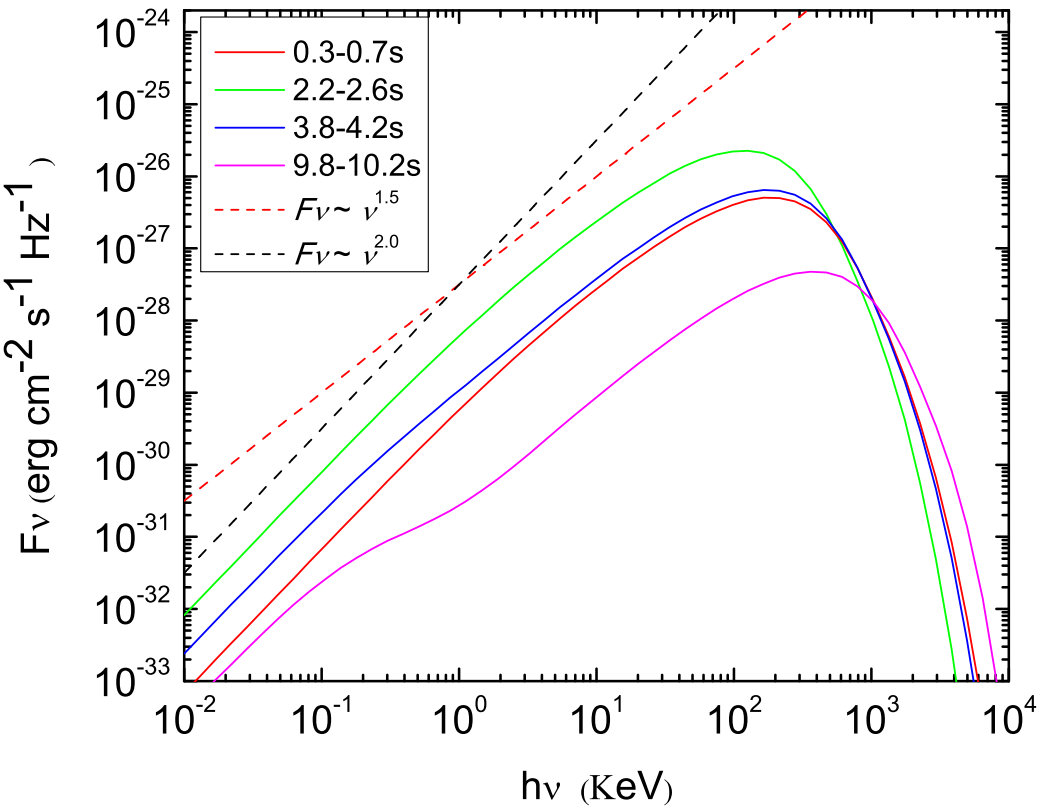

Figure 24 The time integrated photosphere spectra for the case "Slopes: +0.75, -2" with $\Gamma_0 = 300$. Integration in four time intervals are presented: 0.3-0.7 s (red), 2.2-2.6 s (green), 3.8-4.2 s (blue) and 9.8-10.2 s (magenta).

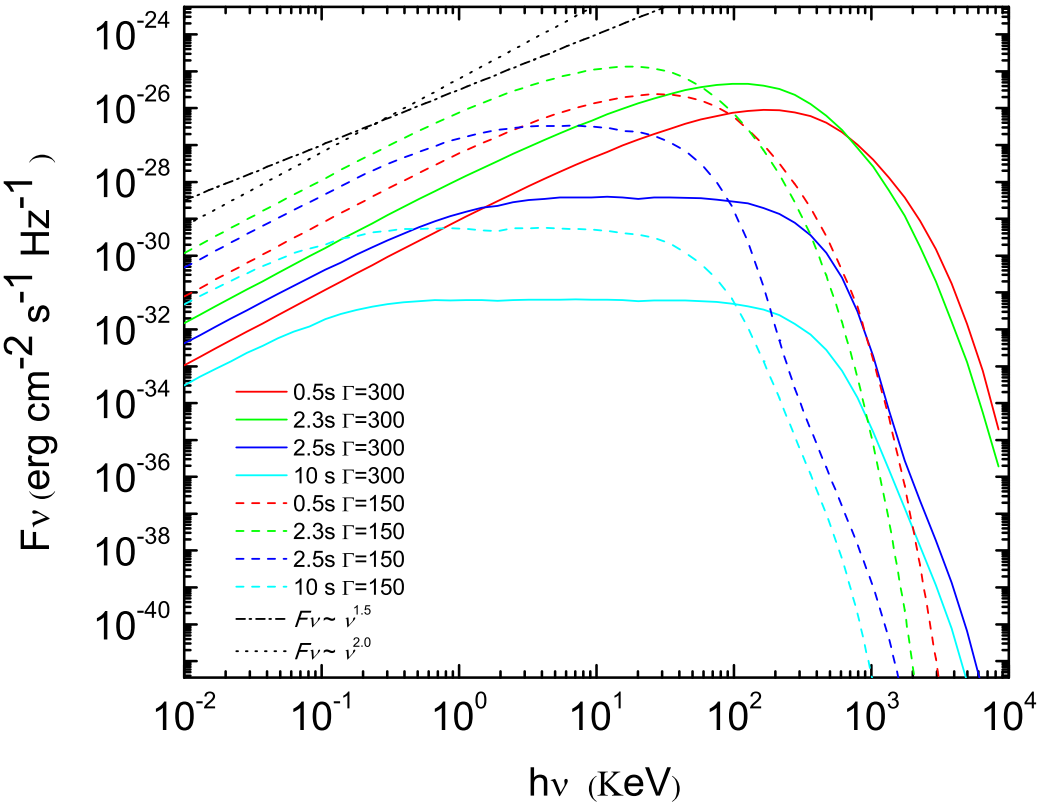

Figure 25 The instantaneous photosphere spectra for a variable luminosity wind with abrupt shut-down of the central engine. The parameters are the same as Fig.23, except there is a sharp cutoff at $\hat{t}_p = 2.4$ s. The dashed lines are for $\Gamma_0 = 150$, while the solid lines are for $\Gamma_0 = 300$. Different colors represent different observational times.

2.3.5 E_p evolution

The evolution of E_p is an important criterion to judge the correctness of a GRB prompt emission model. Observationally, hard-to-soft evolution and intensity-tracking patterns across a broad GRB pulse have been identified (Liang & Kargatis, 1996; Ford et al., 1995; Lu et al., 2010, 2012), and some tracking behavior may be due to superposition of intrinsically hard-to-soft evolution pattern in most pulses (Hakkila & Preece, 2011; Lu et al., 2012). It is important to check whether the quasi-thermal photosphere emission can reproduce the observed E_p evolution patterns.

Before performing numerical calculations, it is instructive to perform some analytical estimates. For the regime $r_{ph} > r_s$ we are interested in, one has $\eta = \Gamma_0$, $T_{ph} \propto L_w^{1/4} r_0^{-1/2} (r_{ph}/r_s)^{-2/3}$, $r_s = \eta r_0$, and $r_{ph} \sim L_w \eta^{-3}$, so that the observer temperature can be expressed as:

$$E_p \propto T_{ph} \propto L_w^{-5/12} r_0^{1/6} \eta^{8/3}. \tag{2.44}$$

One can immediately see that if η and r_0 are constants, E_p is anti-correlated to L_w. This trend seems to be consistent with the "hard-to-soft" evolution pattern during the pulse rising phase. However, it gives an opposite trend during the pulse decaying phase, namely, E_p rises as luminosity drops. Based on the numerical results of instantaneous spectra presented in Fig.22, we plot E_p evolution with respect to wind and photosphere luminosities in Fig.26. The $L_w - E_p$ anti-correlation is clearly shown. Such a pattern has never been observed in GRB pulses.

A related idea would be to attribute to the decaying phase as due to the high-latitude curvature effect. By doing so, one may expect to have E_p continues to decay during the decaying phase of the pulse. Including the $E_p - L_w$ anti-correlation during the rising phase, this might reproduce the observed hard-to-soft evolution pattern. In Fig.27, based on the numerical results of the instantaneous spectra presented in

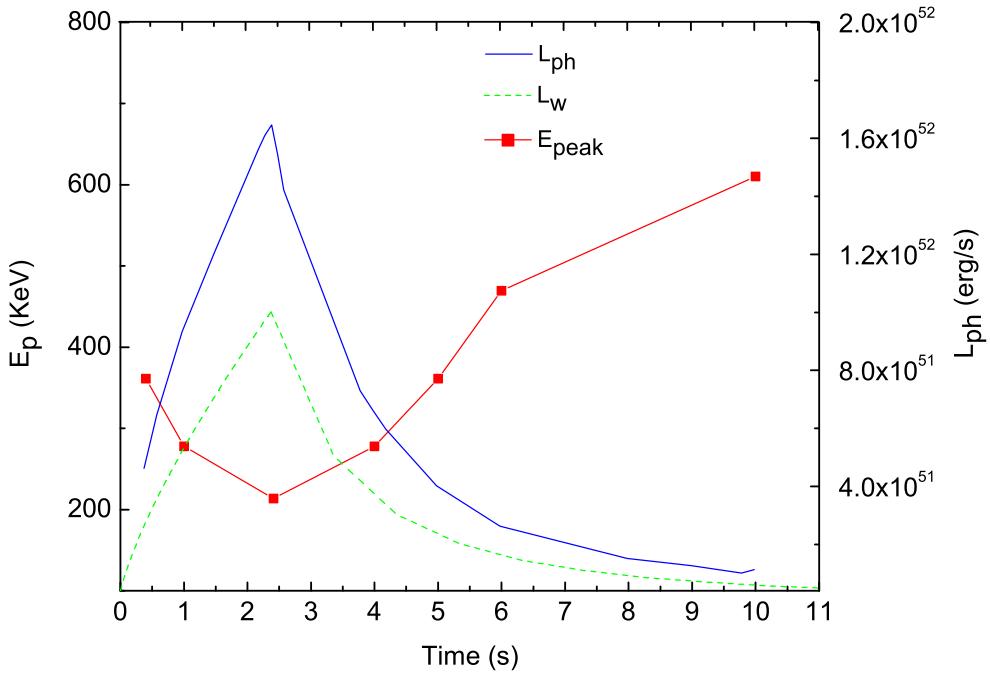

Figure 26 The evolution of E_p (Red solid line), initial wind luminosity L_w (green dash line), and the photosphere luminosity L_{ph} (blue solid line) for the case "Slopes: +0.75, -2", $\Gamma_0 = 300$.

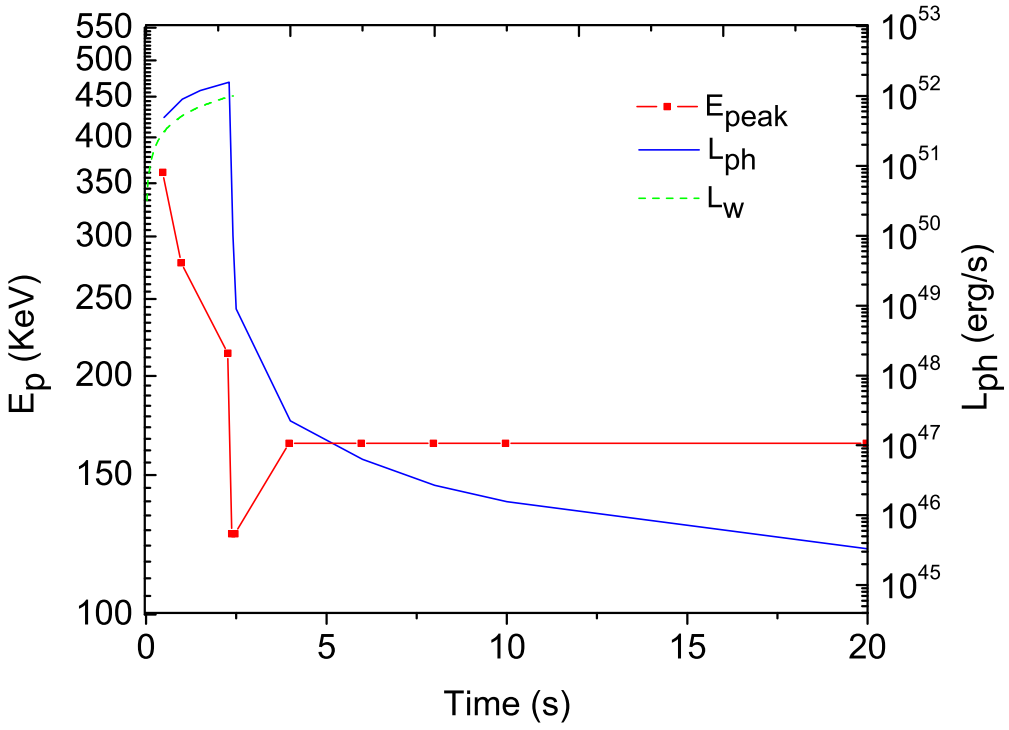

Figure 27 The evolution of E_p (Red solid line), initial wind luminosity L_w (green dash line), and the photosphere luminosity L_{ph} (blue solid line) for the case "Slope +0.75" with an abrupt shut-down and $\Gamma_0 = 300$.

Fig.25, we plot E_p evolution with respect to wind and photosphere luminosities. As can be seen from the figure, this model also cannot reproduce the data. There are two problems: First, the high-latitude curvature tail of the photosphere luminosity light curve drops rapidly (similar to Fig.15), since the photosphere radius is small. The predicted E_p evolution during the tail (even though not measurable due to the rapid decay of the flux) displays a flat feature. This is because the upper end of the flat segment of the F_ν spectrum in the high-latitude-emission-dominated phase (which defines E_p) essentially does not decay with time (Fig.14).

If one allows η to vary with L_w with a certain power law dependence, the E_p-evolution pattern may be modified. From Eq.2.44, one can see that if one defines $\eta = L_w^m$, one would have $E_p \propto L_w^{(-5+32m)/12}$. The $E_p - L_w$ dependence would be reversed

(i.e. positive dependence) when $m > 5/32 \simeq 0.156$. From afterglow data, Liang et al. (2010); Lü et al. (2012) have discovered a rough global $\Gamma_0 \propto L_w^{1/4}$ correlation in different GRBs. If such a correlation also exist within a same GRB, as theoretically motivated in GRB central engine models (Lei et al., 2013), then one would predict an $E_p - L$ intensity tracking behavior within this simple photosphere model. Such a pattern has been observed in a fraction of GRB pulses (Lu et al., 2012). For the hard-to-soft evolution case, on the other hand, in order to reproduce the data, one has to demand that the index m switches from $m < 5/32$ before the peak to $m > 5/32$ after the peak. This requires contrived physical conditions that are not known theoretically.

2.4 Conclusions and Discussion

In this Chapter, we have developed a sophisticated method to calculate quasi-thermal GRB photosphere spectra numerically by introducing several improvements on previous treatments (Pe'er, 2008; Pe'er & Ryde, 2011). The new ingredients introduced in this Chapter include: the probability distribution of the location of a dynamically evolving photosphere, superposition of emission from an equal-arrival-time "volume" in a continuous wind, the evolution of optical depth of a wind with finite but evolving outer boundary, as well as the effect of different wind luminosity profiles. By assuming a co-moving blackbody spectrum emerging from the photosphere and a top-hat jet profile, we address how these effects modify the observed spectra from blackbody. The following robust conclusions are drawn: 1. For an outflow with constant or increasing wind luminosity, the low-energy spectrum below E_p can be modified to $F_\nu \sim \nu^{1.5}$, corresponding to a low-energy photon index $\alpha \sim +0.5$. Introducing temporal smearing does not change α significantly. 2. A softer spectrum can be obtained during the phase of decreasing wind luminosity with time, and a flat spectrum $F_\nu \sim \nu^0$ ($\alpha = -1$) can be obtained only when the spectrum is high-latitude

emission dominated. However, since the photosphere radius is small, the flux drops very rapidly shortly after the wind terminates. 3. Depending on how η is related to L_w, this model can give both negative or positive $E_p - L_w$ correlation. The observed "hard-to-soft" evolution of E_p across broad pulses of seconds duration (Lu et al., 2012) cannot be interpreted with this simple photosphere model, unless an unknown contrived physical condition to switch the index m at the pulse peak is invoked. The intensity tracking patterns as observed in some broad pulses (Lu et al., 2012) can be accounted for this model if $\eta \propto L_w^m$ with $m > 5/32$.

The results presented here suggest that the observed dominant spectral component, the so-called "Band-function" (Band et al., 1993) component, is not easy to interpret by this simplest photosphere model. The predicted low energy spectral index $\alpha = +0.5$) is too hard compared with the typical observed value ($\alpha = -1$), and the widely observed "hard-to-soft" E_p evolution across broad pulses cannot be accounted for unless a contrived condition is invoked. In order to naturally interpret GRB spectra within the framework of the photosphere model, more complicated factors have to be considered. One possibility is to introduce energy dissipation (e.g. proton-neutron collisions, internal shocks, or magnetic reconnections) and particle heating around the photosphere region. Such a dissipative photosphere model can naturally account for a high energy tail through Compton scattering, but could not significantly modify the low-energy spectral index from $\alpha \sim +0.5$. Vurm et al. (2011) introduced a synchrotron emission component, which peaks below the quasi-thermal component to make the "effective" low-energy spectral index softer. In order to make this synchrotron + quasi-thermal spectrum mimic a Band-function as observed, the outflow magnetization parameter has to fall into a narrow range. Recently, Thompson & Gill (2013) invoked a magnetically dominated, low baryon-loading outflow, and modified the low-energy spectral index through the contribution from electron-positron pairs. Several authors pointed out the contrived conditions for the dissipative photo-

sphere models to produce a single-component spectrum (Vurm et al., 2013; Asano & Mészáros, 2013; Kumar & Zhang, 2013). Another possibility to soften the spectrum below E_p is to introduce a structured jet. Lundman et al. (2013) showed that $\alpha \sim -1$ can be reproduced given that the GRB jets have a near constant L_w but a structured Lorentz factor profile with angle. This can enhance the high-latitude contribution (large $1/\Gamma$ cone at high-latitudes) to raise flux in large angles. For more general structured jets where both L_w and Γ follow a certain angular profile (e.g. Mészáros et al., 1998; Zhang & Mészáros, 2002b; Rossi et al., 2002; Zhang et al., 2004), the α value would not be very different from what is calculated in this Chapter. In all these models, it is unclear how the "hard-to-soft" E_p evolution commonly observed in many GRB pulses can be accounted for.

Alternatively, the main Band-component in the GRB spectra could arise from an optically-thin region well above the photosphere due to synchrotron radiation. Uhm & Zhang (2014) recently showed that if the emission radius is large enough, the fast cooling problem for synchrotron radiation is alleviated, and $\alpha \sim -1$ can be reproduced in a moderately fast cooling regime. The hard-to-soft E_p evolution pattern is a natural prediction in this model, since the outflow streams from small-radii where magnetic fields are stronger to large-radii where magnetic fields are weaker. Alternatively, the Band component may be interpreted as slow-cooling or slow-heating synchrotron emission in internal shocks where magnetic field strengths decays rapidly behind the shock (Pe'er & Zhang, 2006; Asano & Terasawa, 2009; Zhao et al., 2014).

Recent Fermi observations revealed a quasi-thermal component superposed on the main Band component in a growing population of GRBs (Ryde et al., 2010; Zhang et al., 2011; Guiriec et al., 2011; Axelsson et al., 2012; Guiriec et al., 2013). The spectral shape in our calculated photosphere emission is consistent with what is observed, suggesting that that component is very likely the photosphere emission from the GRB outflow (Pe'er et al., 2012). This component is typically weaker than

what is predicted in the standard fireball-internal-shock model, so that a certain degree of magnetization is needed for the outflow (Zhang & Pe'er, 2009). Within this picture, the non-thermal emission region in the optically-thin zone could be the internal shock region only if the magnetization parameter already falls below unity at the internal shock radius (Daigne et al., 2011). It is possible that the outflow is still moderately magnetically dominated in the large zone. In this case, efficient GRB emission is possible due to internal-collision-induced magnetic reconnection and turbulence (ICMART) (Zhang & Yan, 2011; Zhang & Zhang, 2014).

CHAPTER 3

RELATIVISTIC MHD SIMULATIONS OF COLLISION-INDUCED MAGNETIC DISSIPATION IN POYNTING-FLUX-DOMINATED JETS/OUTFLOWS

This chapter is based on the following paper :

Deng, W., Li, H., Zhang, B., & Li, S. 2015, The Astrophysical Journal, in press, arXiv:1501.07595

LA-UR-15-20564

3.1 Motivation and Introduction

The energy composition in the jet/outflow of astrophysical systems is an important and fundamental question, since it leads to significant differences for the subsequent energy dissipation process, particle acceleration mechanism, radiation spectrum and light curve, polarization behavior, neutrino emission luminosity, and so on. Generally speaking, jets can be separated into two types depending on their energy composition: Poynting-flux-dominated (PFD) ($\sigma >> 1$) and matter-flux-dominated (MFD) ($\sigma << 1$), where σ is the magnetization parameter defined as the ratio between the electromagnetic field (EMF) energy flux to the plasma matter energy flux.

Many independent observations from Gamma-Ray Bursts (GRBs), Active Galactic Nuclei (AGNs), micro-quasars, and Crab nebula give strong hints of the PFD outflows at least for some events. Several theoretical models have been proposed within the framework of PFD jets/outflows to interpret the observations.

In the field of GRBs, evidence of PFD jets has been collected independently in several directions. First, a prominent thermal emission component as expected in the fireball-internal-shock model (e.g. Mészáros & Rees, 2000) has been seen only in a small fraction of GRBs (e.g. GRB 090902B, Ryde et al. 2010; Zhang et al. 2011). The majority of GRBs either show no evidence of a thermal component or a weak, sub-dominant thermal component (e.g. Abdo et al., 2009a; Guiriec et al., 2011; Axelsson et al., 2012). These GRBs require that the GRB central engine is highly

magnetized, and jet is still PFD at the emission site (Zhang & Pe'er, 2009; Gao & Zhang, 2015). Next, strong linear polarization was discovered during the prompt gamma-ray emission phase for some GRBs (Yonetoku et al., 2011, 2012), and during the reverse-shock-dominated early optical afterglow emission phase for some others (Steele et al., 2009; Mundell et al., 2013), which hint at the existence of globally ordered magnetic fields in the jet. Furthermore, strong PeV neutrino emission as predicted by the MFD models has not been observed from GRBs so far (Abbasi et al., 2012), which is consistent with the expectation of the PFD models (Zhang & Kumar, 2013). Finally, the MFD internal shock (IS) model for GRBs also suffers some criticisms, such as low energy dissipation efficiency (Panaitescu et al., 1999; Kumar, 1999), electron fast cooling (Ghisellini et al., 2000), the electron number excess (Bykov & Mészáros, 1996; Daigne & Mochkovitch, 1998; Shen and Zhang, 2009), and inconsistency with some empirical (Amati/Yonetoku) relations (Zhang & Mészáros, 2002a; Liang et al., 2010). Zhang & Yan (2011) proposed a novel PFD outflow model named as "the Internal-Collision-induced MAgnetic Reconnection and Turbulence (ICMART)", which can potentially keep the merits of the IS model but alleviate the criticisms faced by the IS model mentioned above. The main idea of the ICMART model is that the GRB jets are Poynting-flux dominated. The Poynting flux is catastrophically discharged at a relatively large distance (e.g. 10^{15} cm) from the central engine through collision-induced magnetic reconnection. The magnetic energy is converted to particle energy and radiation efficiently, leading to a very high radiation efficiency as demanded by the GRB data (Panaitescu & Kumar, 2002; Zhang et al., 2007). A PFD jet has less leptons than the MFD model so that the electron excess problem is avoided. A large emission radius favors a moderately fast cooling, which can account for the right low-energy spectral index observed in GRBs (Uhm & Zhang, 2014). It also gives a natural explanation of the seconds-duration of "slow variability component"observed in GRBs (Gao et. al., 2012). The rapid

"fast variability component" can be interpreted within this scenario as mini-jets due to locally Lorentz boosted regions (see also Lyutikov & Blandford 2003; Narayan & Kumar 2009[1]). It is speculated that turbulent reconnection in a moderately high-σ flow can give rise to relativistic motion of mini-jets within the bulk relativistic motion of the jets.

For AGNs, observations show fast variable TeV flares of two blazars (Mrk 501 and PKS 2155-304) (Aharonian et al., 2007; Albert et al., 2007). The light-crossing time is even shorter than the event horizon size of the black holes, so that emission must come from a small local region. The derived Lorentz factor in the emission region should be larger than 50 (Begelman et al., 2008; Mastichiadis & Moraitis, 2008). This value is much larger than the observed Lorentz factor of the bulk motion of the global jet, which is generally smaller than 10 (Giroletti et al., 2004; Piner & Edwards, 2004). To interpret these observations, Giannios et al. (2009) proposed a "jets in a jet" model, which considers that some mini-jets are generated by local reconnection outflows in a global PFD jet. The mini-jets can give extra Lorentz boosting and particle acceleration to generate the observed TeV photons around these local reconnection regions with fast variability. Even though Giannios et al. (2009) did not specify the mechanism of magnetic dissipation, observations of AGN jets reveal bright knots that are consistent with internal interactions within the jet. Within the PDF jet scenario, ICMART processes similar to what are envisaged in GRB jets may also play a role.

Another related astrophysical phenomenon is γ-ray flares observed from the Crab nebula. Monte carlo simulations suggest that the bright γ-ray flares and fluctuations in longer time scales can be understood within the framework that there are many mini-jets with a wide distribution of size and Lorentz factor within the PFD outflow of

[1]Lyutikov & Blandford (2003) and Narayan & Kumar (2009) proposed that GRB variability is a consequence of mini-jets due to relativistic outflow from reconnection or relativitic turbulence. There is no simple explanation to the observed slow variability component in these models. Zhang & Yan (2011) attributed the two variability components (slow and fast) as due to central engine activity and mini-jets, respectively. Monte Carlo simulations by Zhang & Zhang (2014) showed that the ICMART model can indeed reproduce the observed GRB light curves.

the pulsar. The flares correspond to the epochs when some bright mini-jets beaming towards earth (Yuan et al., 2011). The observations suggest that similar physical processes as those operating in GRBs and AGNs may be playing a role in the Crab nebula.

In another front, recent Partical-In-Cell (PIC) simulations (Sironi & Spitkovsky, 2014; Guo et al., 2014) show that reconnection under high-σ condition can efficiently accelerate thermal particles to form a non-thermal power-law population of the particles. This gives a good support to the above PFD models from the particle acceleration point of view.

The models discussed above for different astrophysical systems share some common physical processes, such as efficient magnetic energy dissipation in the PFD outflow/jet, mini-jets generated by the relativistic outflows due to local reconnections, particle acceleration in the reconnection region, and production of the non-thermal emission. Although these models show great potential to interpret the observations and overcome the criticisms in the traditional MFD models, some important ingradients of the models are still of a speculative nature. Detailed numerical simulations are needed to give a solid footing to these models.

From the morphologic point of view, jets/outflows can be categorized into two types: continuous and episodic. Theoretically, episodic jets can be formed either from a highly variable central engine with variable accretion rate; or disruption of a continuous jet by screw or kink instabilities (Li, 2000; Mizuno et al., 2009); or from a MHD erruption process similar to solar coronal mass ejection (Yuan et al., 2009; Yuan & Zhang, 2012). Observationally, episodic jets or knots in jets have been observed in many X-ray binaries (Mirabel & Rodriguez, 1994; Hjellming & Rupen, 1995; Fender & Belloni, 2004) and AGNs (Marscher et al., 2002; Chatterjee et al., 2009; Doi et al., 2011). Rapid variabilities observed in GRBs also point towards highly episodic jets (Rees and Mészáros, 1994; Paczýnski and Xu, 1994). As a result,

studying interactions or collisions between magnetic blobs or shells is of great interest.

In this chapter, we perform detailed numerical simulations on the global properties of collisions between high-σ blobs, as envisaged in the ICMART model of GRBs (Zhang & Yan, 2011). In Section §3.2, we give a brief introduction of our 3D relativistic MHD code and the simulation setup. In Section §3.3, we present an example simulation case to show the key results, and perform a detailed analysis and resolution study. We then expand our simulations on two-blob collisions in Section §3.4 to a large parameter space and discuss how different parameters affect the simulations results. In Section §3.5, we show preliminary results for multiple collisions among four high-σ blobs. We summarize our results in Section §3.6 and discuss the implications of our simulation results on some high energy astrophysical systems, such as GRBs and AGNs.

3.2 Numerical Method and Problem Setup

3.2.1 Code introduction

We use a 3D special relativistic MHD (SRMHD) code which solves the conservative form of the ideal MHD equations using higher-order Godunov-type finite-volume methods. This code is a development version of the "LA-COMPASS" MHD code which was first developed by Li & Li (2003) at Los Alamos National Laboratory. The

equations solved in the code are:

$$\frac{\partial(\Gamma\rho)}{\partial t} + \nabla \cdot (\Gamma\rho \boldsymbol{V}) = 0, \tag{3.1}$$

$$\frac{\partial}{\partial t}(\frac{\Gamma^2 h}{c^2}\boldsymbol{V} + \frac{\boldsymbol{E}\times\boldsymbol{B}}{4\pi c}) + \nabla \cdot [\frac{\Gamma^2 h}{c^2}\boldsymbol{V}\otimes\boldsymbol{V} + (p + \frac{B^2+E^2}{8\pi})\boldsymbol{I} - \frac{\boldsymbol{E}\otimes\boldsymbol{E} + \boldsymbol{B}\otimes\boldsymbol{B}}{4\pi}] = 0, \tag{3.2}$$

$$\frac{\partial}{\partial t}(\Gamma^2 h - p - \Gamma\rho c^2 + \frac{B^2+E^2}{8\pi}) + \nabla \cdot [(\Gamma^2 h - \Gamma\rho c^2)\boldsymbol{V} + \frac{c}{4\pi}\boldsymbol{E}\times\boldsymbol{B}] = 0, \tag{3.3}$$

$$\frac{\partial \boldsymbol{B}}{\partial t} + c\nabla \times \boldsymbol{E} = 0, \tag{3.4}$$

$$\boldsymbol{E} = -\frac{\boldsymbol{V}}{c} \times \boldsymbol{B}, \tag{3.5}$$

where Γ, ρ, h, P are the Lorentz factor, rest mass density, relativistic enthalpy, and gas pressure, respectively, $\boldsymbol{V}$, $\boldsymbol{E}$, $\boldsymbol{B}$ are the vectors of fluid velocity, electric field, and magnetic field, respectively, and the symbol "$\otimes$" denotes tensor product. We also use the ideal gas equation of state: $p = (\hat{\gamma} - 1)u$, where $\hat{\gamma}$ and u are the adiabatic index and the internal energy density, respectively.

We use HLL flux with the piecewise parabolic reconstruction method to solve the Riemann problem (Colella & Woodward, 1984), and use the constrained transport (CT) method (Balsara & Spicer, 1999; Guan et al., 2014) to ensure $\nabla \cdot \boldsymbol{B} = 0$. We use the Cartesian coordinates (x, y, z) in our simulations.

3.2.2 Problem set up

We envisage that the central engine of GRBs or AGNs launch a Poynting-flux-dominated jet/outflow. As discussed in Section §3.1, episodic jets are preferred from observational data. Even if the jet may be overall continuous, it is very likely non-uniform internally and may form many knots in the jet, where a much larger amount of EMF energy ($E_{\rm em}$) is concentrated compared with other sparse regions in the

jet. We can simplify the knots of the jet/outflow as many quasi-isolated magnetic blobs with both poloidal and toroidal field components. Due to the intrinsic erratic behavior at the central engine, different magnetic blobs may have different velocities at the emission region, so that multiple collisions are very likely to happen among different blobs. Due to the ultra relativistic motion of the jet, the relative velocities between different blobs can easily become relativistic.

In our simulation domain, we use the model from Li et al. (2006) to initialize the magnetic field configuration. The equations are introduced in the cylindrical coordinates (r, ϕ, z), and we will transfer them to the Cartesian coordinates (x, y, z) in our simulations. from the center ($r = 0$) of each blobs, the field is assumed to be axisymmetric with the poloidal flux function Φ as

$$\Phi(r, z) = B_{\rm b,0} r^2 \exp\left(-\frac{r^2 + z^2}{r_0^2}\right), \tag{3.6}$$

and the relationship between $\Phi(r, z)$ and the ϕ component of the vector potential A_ϕ is $\Phi(r, z) = rA_\phi$. $B_{\rm b,0}$ and r_0 are the normalization factor for the magnetic strength and characteristic radius of the magnetic blob, respectively. One can then calculate the $r-$ and $z-$ components of the poloidal field

$$B_r = -\frac{1}{r}\frac{\partial \Phi}{\partial z} = 2B_{\rm b,0}\frac{zr}{r_0^2}\exp\left(-\frac{r^2 + z^2}{r_0^2}\right), \tag{3.7}$$

and

$$B_z = \frac{1}{r}\frac{\partial \Phi}{\partial r} = 2B_{\rm b,0}\left(1 - \frac{r^2}{r_0^2}\right)\exp\left(-\frac{r^2 + z^2}{r_0^2}\right). \tag{3.8}$$

The poloidal field is closed and keeps the net global poloidal flux as zero. The toroidal field configuration is motivated by considering the black hole accretion disk system as a "dynamo", which shears the poloidal flux to form the toroidal flux from

the rotation. The toroidal component of the magnetic field therefore has the form

$$B_\phi = \frac{\alpha\Phi}{r_0 r} = B_{\rm b,0}\alpha\frac{r}{r_0}\exp\left(-\frac{r^2+z^2}{r_0^2}\right) \ . \tag{3.9}$$

Here the parameter α controls the toroidal-to-poloidal flux ratio. Li et al. (2006) showed that when $\alpha \sim 3$, the two flux components are roughly equal with each other. We set $\alpha = 3$ for our example simulation, and explore a larger value of α in Section §3.4.7. We choose the comoving center-of-mass frame of the blobs as our simulation frame. The direction of velocity is along Z-axis with a profile

$$V_z = \begin{cases} V_{\rm b,z}, & (r \le r_0), \\ \\ V_{\rm b,z}\exp\left(-\left(\frac{r-r_0}{r_0/2}\right)^2\right), & (r > r_0), \end{cases} \tag{3.10}$$

where $V_{\rm b,z}$ is a constant value which can be either positive or negative corresponding to $+Z$ or $-Z$ direction of the velocity. We also set a uniform gas pressure value (P) both inside and outside the blobs. The value of P is much smaller than the initial magnetic energy density of the blobs.

For the density profile, we first define a constant initial value of the blob magnetization parameter around the central region of the blobs:

$$\sigma_{\rm b,i} = \frac{E_{\rm em}}{\Gamma^2 h}, \tag{3.11}$$

where $h = \rho c^2 + \hat{\gamma}P/(\hat{\gamma}-1)$ is the specific enthalpy defined in the fluid's comoving frame, ρ is the rest mass density, P is the gas pressure introduced above, $\hat{\gamma}$ is the adiabatic index, Γ is the bulk Lorentz factor calculated by the velocity profile introduced above, and $E_{\rm em}$ is the EMF energy density calculated by $E_{\rm em} = (\boldsymbol{B}^2 + \boldsymbol{E}^2)/8\pi$

from the magnetic field profile introduced above. The density profile is therefore

$$\rho = \begin{cases} \frac{1}{c^2}\left(\frac{E_{\rm em}}{\Gamma^2\sigma_{\rm b,i}} - \frac{\hat{\gamma}P}{\hat{\gamma}-1}\right), & (r \le r_0 \ \text{ and } \ \rho > \rho_{\rm bkg}), \\ \\ \rho_{\rm bkg}, & (r > r_0 \ \text{ or } \ \rho \le \rho_{\rm bkg}), \end{cases} \tag{3.12}$$

where $\rho_{\rm bkg}$ is a constant parameter to control the uniform background mass density.

We also introduce two position-control parameters z_d and x_s. For a collision between two blobs, the center of the two blobs are located at (x_1, y, z_1) and (x_2, y, z_2), so $z_d = |z_1 - z_2|$ is the initial distance between the center of the two blobs in Z direction, and $x_s = |x_1 - x_2|$ is the initial misalignment between the center of the two blobs in X direction due to the possible misalignment of the blobs. The Y coordinate is the same for both of them.

In Table 1, we give the normalization relationship between the code units and the physical units. There are only three free parameters, L_0, B_0 and c to control the normalization of the entire system. Defining different physical values of L_0 and B_0, we can normalize the simulation system to different environments and problems. In Table 1, we also list two sets of example typical values to show the way of the normalization. In the rest of this Chapter, all the parameters are given using code units. We keep $r_0 = 1.0$ for all the following simulations. In addition, we use $\hat{\gamma} = 5/3$ in most of the simulations, since most of the regimes are mildly relativistic. This may not always be true, especially in the regions of reconnection outflows, so in Section §3.4.8 we also try $\hat{\gamma} = 4/3$ to test the difference.

Parameters:	Length	Velocity	Time	Magnetic field	Pressure	Density
Code units:	1	1	1	1	1	1
Normalization factors:	L_0	c	L_0/c	B_0	B_0^2	B_0^2/c^2
Typical values 1:	10^{12} cm	3×10^{10} cm/s	33 s	10^3 G	10^6 Ba	1.1×10^{-15} g/cm^3
Typical values 2:	10^{13} cm	3×10^{10} cm/s	333 s	10 G	10^2 Ba	1.1×10^{-19} g/cm^3

Table 1 The normalization factors between physical units and code units.

3.3 An Example Case

In this section, we show a series of detailed analyses based on one example simulation case. We focus on the following aspects: the evolution of magnetic energy to address the efficiency of magnetic energy dissipation, the details of the collision process, the properties of magnetic reconnection and outflows, and the numerical resolution effects. We reveal significant collision-induced reconnection events with a remarkable efficiency around 35%, which is resolution insensitive. The outflow properties of reconnection events indicate the potential capability to generate super-Alfvénic relativistic mini-jets.

3.3.1 Initial parameters

The initial parameters of the example run are listed in Table 2. We consider two identical blobs with initial magnetization parameter $\sigma_{\rm b,i} = 8$ separated by $z_d = 4.4$, with an X-direction offset 1.0. The two blobs move in opposite directions in Z direction with an initial center speed $V_{\rm b,z} = 0.3$ c. The background pressure and density are $P = 10^{-2}$ and $\rho_{\rm bkg} = 10^{-1}$, respectively. In order to clearly show the initial magnetic field configuration of the blobs, in Figure 28 we show a $y = 0$ slice (cut through the blob centers) of the profiles of several parameters: projected field line configuration (panel A), σ distribution (panel B), B_x (panel C), and B_y (panel D).

For this example run, the 3D box size is chosen as 20^3 from -10 to +10 in each dimension, which means that the position (x,y,z)=(0,0,0) corresponds to the center of the box. And the resolution is chosen as 1024^3.

3.3.2 Energy evolution analysis

Since the initial magnetic configuration is not in complete force balance (between the internal magnetic pressure and the background gas pressure), the blobs would

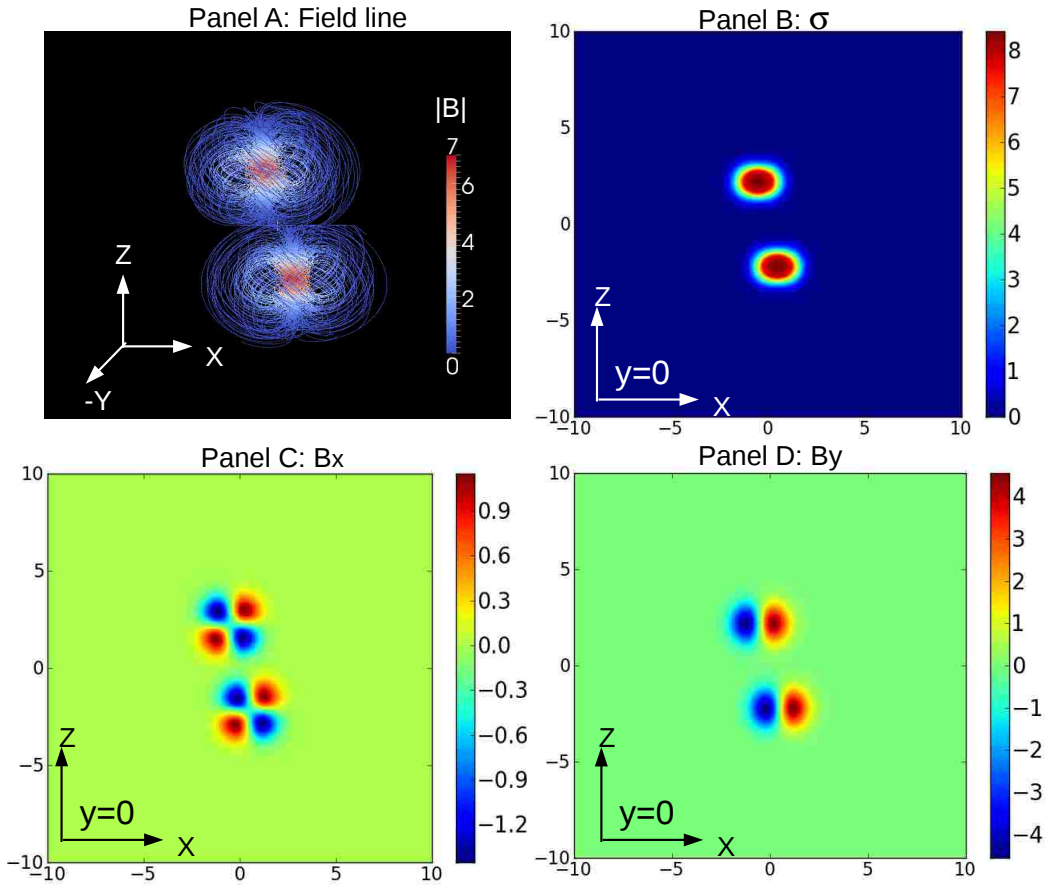

Figure 28 Several manifestations of the initial magnetic field configuration cut in the blob-center plane in the example simulation. *Panel A*: The initial 3D field line profile viewed along the Y direction. The color contour denotes the value of magnetic field strength $|B|$; *Panel B*: The 2D contour cut of the initial σ profile in the XZ plane ($y = 0$); *Panel C*: The 2D contour cut of the x-component of the initial magnetic field strength in the XZ plane ($y = 0$); *Panel D*: The 2D contour cut of the y-component of the initial magnetic field strength in the XZ plane ($y = 0$).

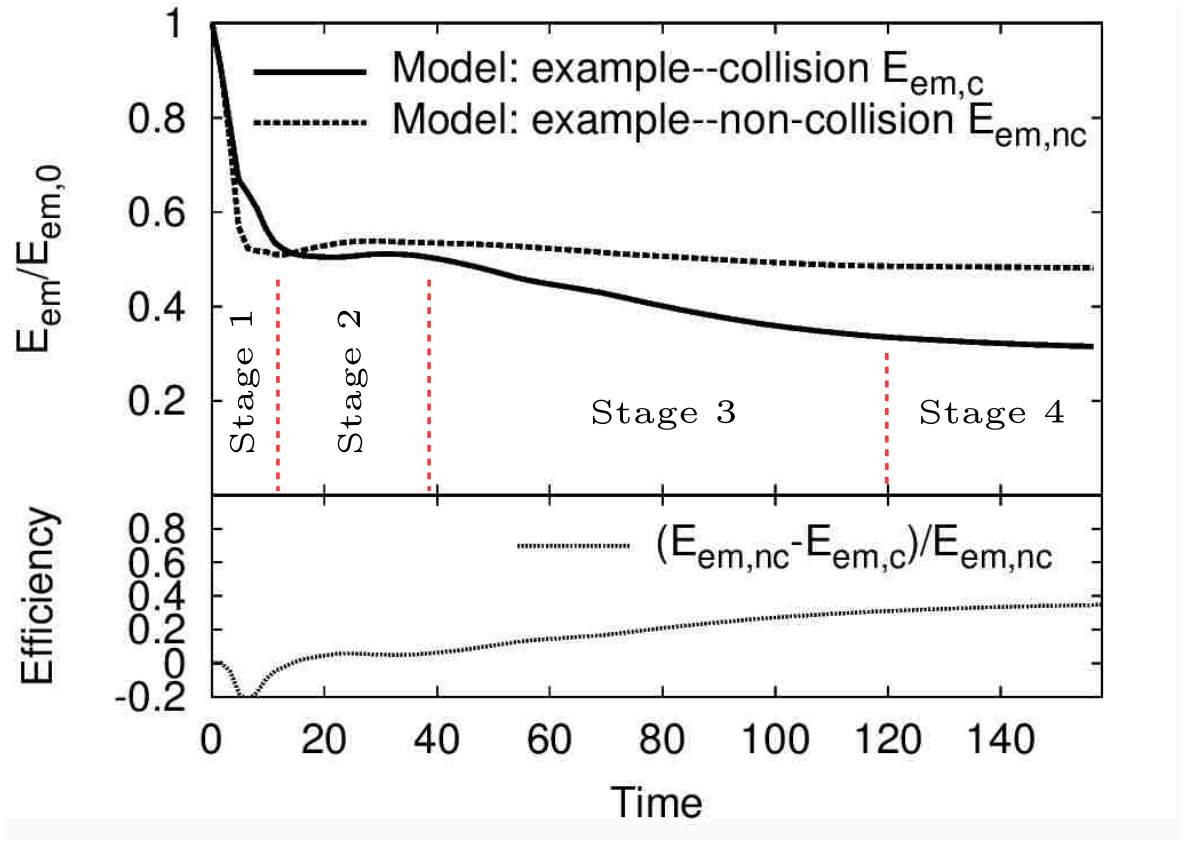

Figure 29 *Upper panel*: The Poynting flux energy ($E_{\rm em}$) evolution of the example simulation case. Dashed line denotes the non-collision case, which serves as the reference for additional magnetic dissipation. Solid line denotes the case of collision between two blobs. *lower panel*: Ratio calculated by $(E_{\rm em,nc} - E_{\rm em,c})/E_{\rm em,nc}$ to show the additional $E_{\rm em}$ dissipation efficiency triggered by the collision-induced processes.

$\sigma_{\rm b,i}$	$B_{\rm b,0}$	α	$\lvert V_{\rm b,z}\rvert$	P	$\rho_{\rm bkg}$	z_d	x_s
8	$\sqrt{4\pi}$	3	0.3c	10^{-2}	10^{-1}	4.4	1.0

Table 2 The initial parameters for the example simulation.

quickly expand and evolve into a quasi-steady phase, forming a quasi-force balance between the gas pressure and magnetic pressure. During this process, a fraction of EMF energy $E_{\rm em}$ is converted to thermal and kinetic energy due to magnetic field relaxation. So before performing a collision simulation, we first simulate the blob evolution of non-collision case to quantify the EMF energy level in the quasi-steady phase. This would serve as the reference value to be compared with the collision case in which additional EMF energy drop is expected due to additional magnetic dissipation.

The upper panel of Figure 29 shows the evolution of the blob electromagnetic energy $E_{\rm em}$ as a function of time (normalized to the initial value $E_{\rm em,0}$). The dashed line shows the evolution in the non-collision case. There is a significant drop of $E_{\rm em}$ before $t \sim 6$, which is due to the magnetic field relaxation during the process of establishing a force balance between the outward magnetic pressure force and the inward gas pressure force. After the balance is established, $E_{\rm em}$ is nearly constant and enters a quasi-steady phase, which can be used as the reference energy level without collision.

Next, we simulate the collision case between two high-σ blobs. The initial parameters for these two blobs are the same as the non-collision case. The $E_{\rm em}$ evolution of the two blobs with collision is shown as the solid line in the upper panel of Figure 29. The efficiency (η) of $E_{\rm em}$ energy dissipation due to collision-induced process can be calculated by

$$\eta = \frac{E_{\rm em,nc} - E_{\rm em,c}}{E_{\rm em,nc}}, \tag{3.13}$$

where $E_{\rm em,c}$ and $E_{\rm em,nc}$ are the EMF energy values for the collision and non-collision cases, respectively. The efficiency of the example case is shown in the lower panel of

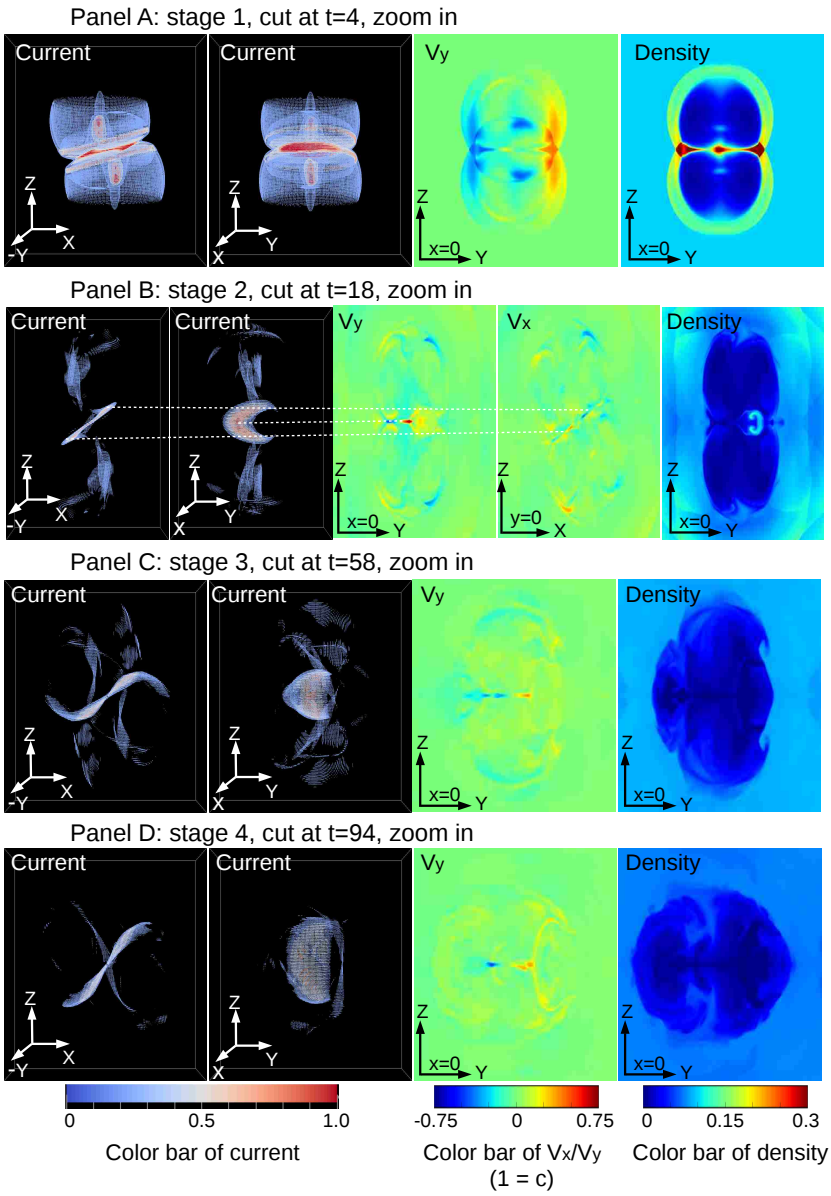

Figure 30 The representative cuts of current, velocity and density for the different evolution stages corresponding to Figure 29. We show them in a zoom-in region whose size is 15^3 from -7.5 to 7.5 in each dimension. (The size of simulation box is 20^3.) Panel A corresponds to the initial "self adjustment" phase; Panel B corresponds to the following "plateau" phase; Panel C & D correspond to the "normal decay" phase. The last quasi-steady phase has no obvious feature, so we do not draw cuts for that stage. For each panel, the cuts from left to right are the 3D current contour plot viewed from Y-axis, the 3D current contour plot viewed from X-axis, the 2D contour cut of the y-component of the outflow velocity (V_y) in the YZ-plane (x=0) corresponding to the current plot, and the 2D contour cut of the rest mass density in the YZ-plane (x=0), respectively. In Panel B, we add an additional 2D contour cut of the x-component of outflow velocity (V_x) in the XZ-plane (y=0) to show the existence of multiple directions of the outflows.

Figure 29, where we find that the efficiency is about 35% near the end of collision process. This efficiency is much higher than the collision-induced kinetic energy release efficiency in the MFD outflows in the internal shock model of GRBs, which is typically a few percent or less (e.g. Panaitescu et al., 1999; Kumar, 1999; Maxham & Zhang, 2009; Gao & Mészáros, 2015). It is consistent with the analytic estimate of the ICMART model (Zhang & Yan 2011, see more discussion below in §3.3.5).

One important question is what mechanism causes this efficient magnetic energy dispassion? From the magnetic configuration we can see B_x and B_y have opposite directions around the collision region (see Figure 28). We suggest that most likely the additional $E_{\rm em}$ dissipation is triggered by strong collision-driven reconnection events. In order to check our conjecture, in the following, we carry out a series of detailed analyses based on our simulation data.

The $E_{\rm em}$ evolution in Figure 29 can be characterized in four stages: (1) an initial "self adjustment" (steep decay) phase before $t \sim 10$; (2) a "plateau" phase from about $t \sim 10$ to $t \sim 38$; (3) a "normal decay" phase from about $t \sim 38$ to $t \sim 120$; and (4) a final quasi-steady phase. We analyze these stages in detail below.

The major collision starts from the later part of the "self-adjustment" steep decay phase. The collision compresses the magnetic fields to make the energy level higher than non-collision case. Panel A of Figure 30 shows a series of representative cuts at $t = 4$. From left to right, the four images display the 3D current contour plot viewed from Y-axis, the 3D current contour plot viewed from X-axis, the 2D contour cut of the y-component of the outflow velocity (V_y) in the YZ-plane (x=0) corresponding to the current plot, and the 2D contour cut of the rest mass density in the YZ-plane (x=0), respectively. From these results we find that a strong current layer and a pair of outflows are forming around the contact surface, which are consistent with the features of a collision-driven reconnection.

The second stage is the "plateau" phase from about $t \sim 10$ to $t \sim 38$. Panel

B of Figure 30 shows a series of representative cuts at $t = 18$. We can see that the current layer around the contact surface becomes clearer and more concentrated. The outflows become faster (nearly 0.75c) and are also more concentrated at the current layer. Besides the four representative cuts shown in all panels, for panel B, we also add one extra 2D contour cut of the x-component of the outflow velocity (V_x) in the XZ-plane (y=0) corresponding to the current plots, which presents another important result that the current layer actually generates multi-orientation outflows in a 3D structure. These results suggest that many mini-jets with relativistic speeds can be potentially generated, if multiple collisions are invoked in a PFD outflow. Another interesting phenomenon is that although the system undergoes a strong reconnection process which in principle dissipates the EMF energy significantly, the global $E_{\rm em}$ evolution is nearly flat and even shows slight increase during this stage. The main reason for this feature is that the initial strong reconnection is collision-driven. Besides the strong reconnection, collision-induced strong compression also exists and tends to increase $E_{\rm em}$, which balances and even slightly surpasses $E_{\rm em}$ dissipation due to reconnection. The additional outflow study in the following Section §3.3.3, which shows that the outflows become super-Alfvénic at this stage, also supports the above analysis.

The next stage is the "normal decay" phase. We choose two series of representative cuts at $t = 58$ (Panel C) and $t = 94$ (Panel D), respectively. The current strength and outflow velocity are similar between panels C and D, while they are systematically weaker and slower compared with the "plateau" phase (panel B). This means that the initial collision-driven effect becomes weaker and the reconnection-facilitated dissipation enters a relatively steady phase. In the mean time, compression becomes sub-dominant, so that globally $E_{\rm em}$ dissipates with a relatively steady rate, which roughly equals to $\frac{0.1E_{\rm em,0}}{40t_0} = \frac{c\cdot E_{\rm em,0}}{400L_0}$ in the center-of-mass frame of the blobs (L_0 is the length normalization factor introduced in Table 1). The additional outflow study in

the following Section §3.3.3, which shows that the outflow velocity keeps being around the Alfvén velocity at this stage, also supports this conclusion.

Finally, after $t \sim 120$, the reconnection-dissipation gradually becomes weaker, and the system enters the quasi-steady phase without obvious $E_{\rm em}$ dissipation. The $E_{\rm em}$ evolution becomes nearly parallel with the non-collision case in Figure 29.

From these analyses, we conclude that the collision between two high-σ blobs can indeed trigger strong magnetic reconnections and dissipate a significant fraction of EMF energy due to the reconnection-facilitated processes.

3.3.3 Additional outflow study

Following the above analyses, in this subsection, we carry out an additional study on the outflow velocity. We compare the local Lorentz factor of the outflow ($\Gamma_{\rm out}$) with the critical Lorentz factor $\Gamma_{\rm A}$ calculated from the local relativistic Alfvén velocity

$$V_{\rm A} = \frac{c}{\sqrt{4\pi h'/B'^2 + 1}}, \tag{3.14}$$

and the critical Lorentz factor $\Gamma_{\rm ms}$ calculated from the maximum possible value of the local relativistic fast mode magnetosonic velocity

$$V_{\rm ms} = \sqrt{V_{\rm A}^2 + C_s^2(1 - V_{\rm A}^2/c^2)}, \tag{3.15}$$

where h' and B' are the specific enthalpy and magnetic strength in the local comoving frame of the fluid, and C_s is the relativistic sound speed calculated by

$$C_s = c\sqrt{\hat{\gamma}P/h'}. \tag{3.16}$$

In order to investigate whether the fluid velocities exceed the two characteristic

velocities, we define

$$R_{\rm A} \equiv \frac{\Gamma_{\rm out}}{\Gamma_{\rm A}}, \tag{3.17}$$

$$R_{\rm ms} \equiv \frac{\Gamma_{\rm out}}{\Gamma_{\rm ms}}. \tag{3.18}$$

Figure 31 shows the selected 2D contour cuts of $R_{\rm A}$. The three panels in the upper row correspond to the starting time when $R_{\rm A} > 1$ is reached ($t = 4$), the time when $R_{\rm A}$ is the largest ($t = 18$), and the ending time for the condition of $R_{\rm A} > 1$ ($t = 38$), respectively. After $t \sim 38$, the $\Gamma_{\rm out}$ starts to become slightly smaller but still close to $\Gamma_{\rm A}$ (see the three panels in the lower row of Figure 31). These results are consistent with the energy evolution analysis presented above in Section §3.3.2. The duration when $R_{\rm A} > 1$ is satisfied is just the "plateau" phase of energy evolution, in which strong compression exists and drives the outflows to become super-Alfvénic. After $t \sim 38$ the energy evolution enters the "normal decay" phase, which corresponds to the phase of relatively steady reconnection-facilitated dissipation without strong compression, so that the outflow velocity is close to the theoretical Alfvénic velocity.

Figure 32 show the contour cuts of $R_{\rm ms}$. Since $V_{\rm ms}$ is the maximum wave propagation speed in a MHD system, if $R_{\rm ms} > 1$, a local shock in the front of the outflow would potentially be generated. The three epochs shown in Figure 32 correspond to the starting time when $R_{\rm ms} > 1$ is satisfied ($t = 6$), the time when $R_{\rm ms}$ is the largest ($t = 18$), and the ending time for the condition of $R_{\rm ms} > 1$ to be satisfied ($t = 20$), respectively. These results indeed show a period of about 15 time units during which $R_{\rm ms} > 1$ is satisfied. This duration is shorter than the duration when $R_{\rm A} > 1$ is satisfied. For this case, the largest value of $R_{\rm ms}$ is about 1.13. Since the $\Gamma_{\rm out}$ depends on numerical resolution (see Section §3.3.4 below for details) and other physical parameters, it is worthwhile to perform a more detailed study for this feature in the future. In this study, since $V_{\rm out}$ is only slightly larger than $V_{\rm ms}$ in a small local

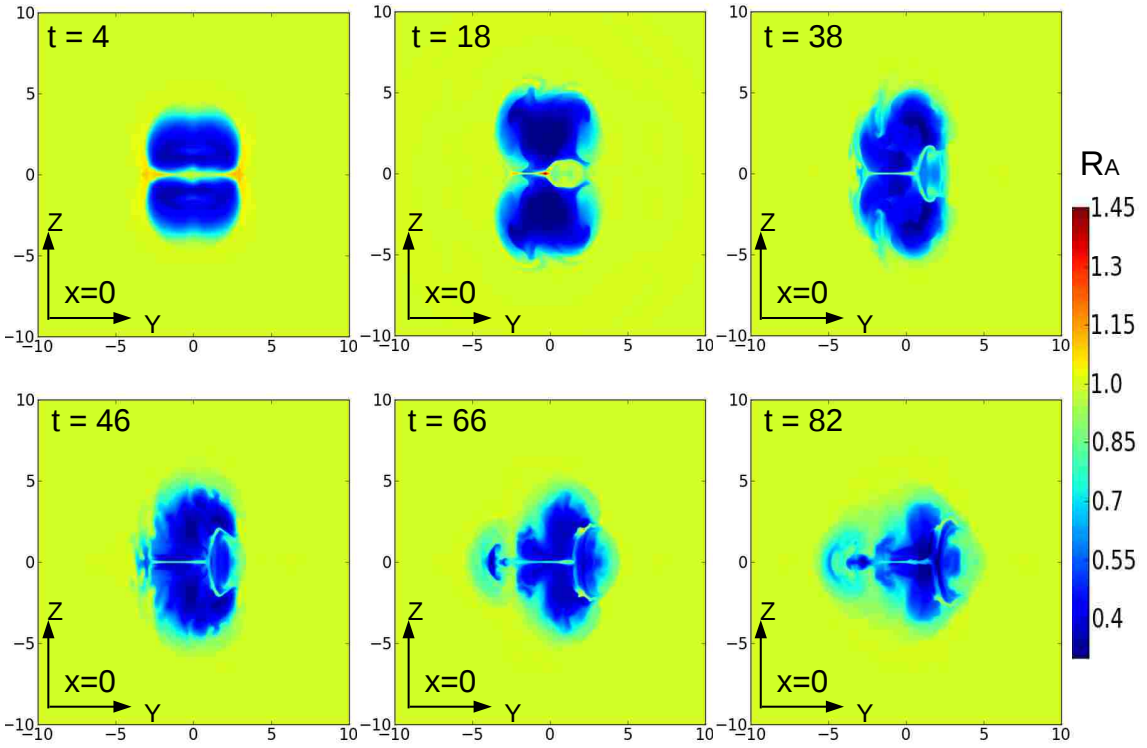

Figure 31 The selected 2D contour cuts of $R_{\rm A}$ for different stages. The three panels in the upper row correspond to the starting time when $R_{\rm A} > 1$, the time when $R_{\rm A}$ is the largest, and the ending time for the condition of $R_{\rm A} > 1$, respectively. These correspond to the plateau stage. The three panels in the lower row correspond to three epochs during the normal decay phase, during which $\Gamma_{\rm out}$ becomes relatively steady and close to $\Gamma_{\rm A}$.

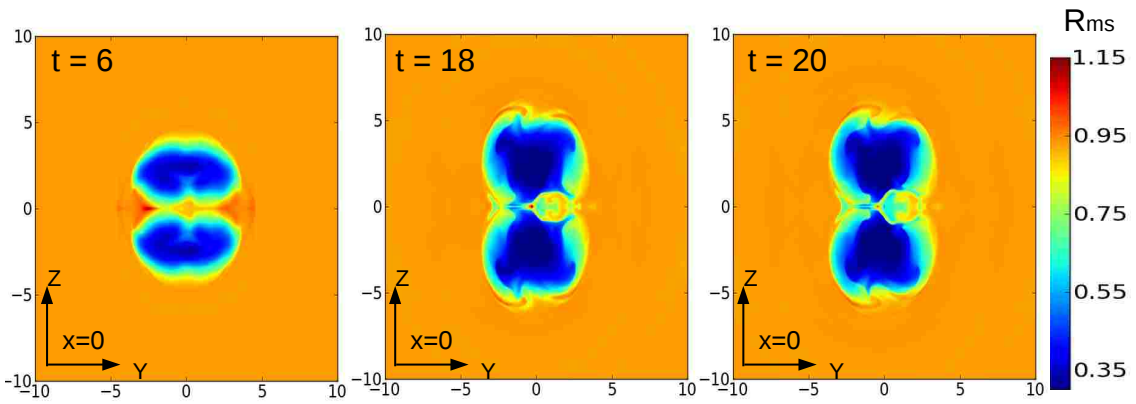

Figure 32 the selected 2D contour cuts from the results of $R_{\rm ms}$. The three panels correspond to the starting time when $R_{\rm ms} > 1$ is satisfied, the time when $R_{\rm ms}$ is the largest, and the ending time when the condition of $R_{\rm ms} > 1$ is satisfied, respectively.

region and for a short duration, we do not resolve an obvious shock feature from the numerical data.

3.3.4 Resolution study

We now discuss the effects of numerical resolution on our results. Although the ideal MHD code that we use does not have explicit resistivity, it still has numerical resistivity from the numerical scheme, which depends on the resolution of the simulation. This may affect the reconnection rate and energy dissipation rate in the simulations. To address this uncertainty, we perform a resolution test based on the above example case. We keep the same box size and the parameters in Table 2, and only change the resolution. Figure 33 shows the results. The magenta, red, green and blue groups of lines correspond to the results with numerical resolution 128^3, 256^3, 512^3 and 1024^3, respectively. When the resolution decreases, we find that the level of $E_{\rm em}$ evolution is systematically lower and the efficiency also slightly decreases. On the other hand, the change of efficiency is only several percentage from the highest to the lowest resolutions, which means that the $E_{\rm em}$ dissipation efficiency is insensitive to numerical resolution. In addition, the $E_{\rm em}$ level and the efficiency in the final quasi-steady phase also show a trend of convergence when the resolution increases.

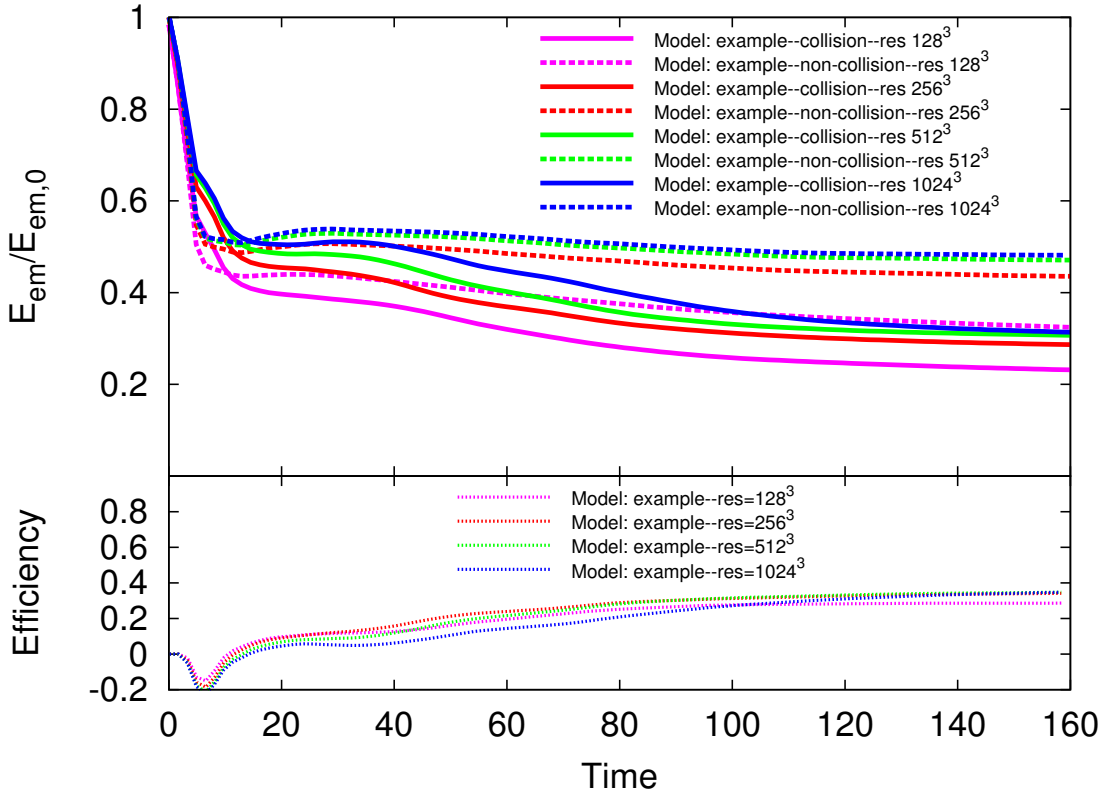

Figure 33 A numerical resolution study based on the above example case in Section §3.3.2. The magenta, red, green and blue groups of lines correspond to the resolutions of 128^3, 256^3, 512^3 and 1024^3, respectively. The $E_{\rm em}$ dissipation efficiency at the finial quasi-steady phase is nearly the same in all cases.

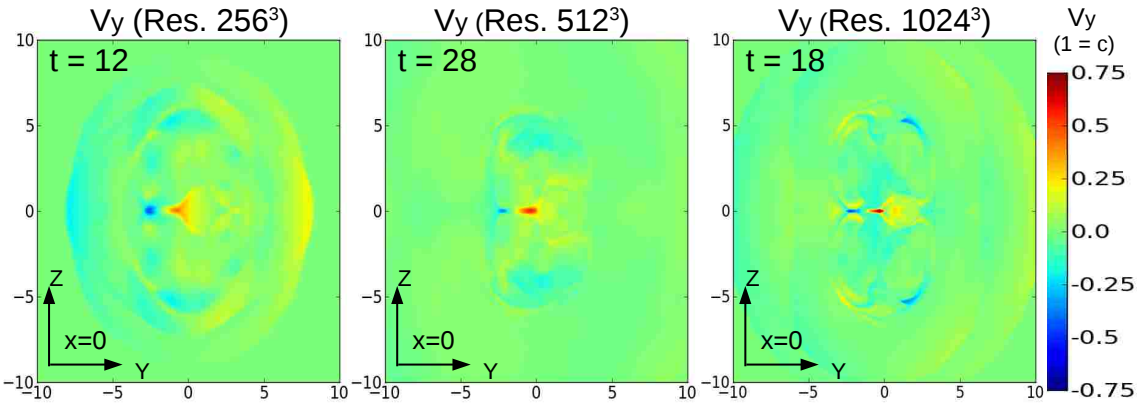

Figure 34 The contour cuts corresponding to the maximum y-component of the outflow velocity (V_y) in the YZ-plane (x=0) for different resolutions. The maximum values of V_y are about $0.45c$, $0.55c$, $0.75c$ for the resolutions of 256^3, 512^3, and 1024^3, respectively. The aspect ratio becomes smaller for a higher resolution.

Another important result from the resolution study is that the maximum outflow velocity increases when the resolution increases. Figure 34 shows the contour cuts corresponding to the maximum y-component of the outflow velocity (V_y) in the YZ-plane (x=0) for different resolutions. The maximum values of V_y are about $0.45c$, $0.55c$, and $0.75c$ for resolution of 256^3, 512^3, and 1024^3, respectively. The reason is probably that the higher resolution decreases the effective numerical resistivity and decreases the aspect ratio between the thickness and the length of the reconnection layer, so that the outflow speed is forced to reach a higher value in order to balance the similar compression forced inflow. This analysis is also supported by Figure 34, which shows that with an increasing resolution, the length of the reconnection layer is similar, but the thickness becomes thinner.

3.3.5 Physical analyses

In this subsection we carry out some physical analyses to understand the $\sim 35\%$ $E_{\rm em}$ dissipation efficiency obtained from our numerical simulations.

Assuming a complete inelastic collision between two high-σ blobs, Zhang & Yan (2011) analytically estimated the total efficiency of the collision-induced $E_{\rm em}$ dissi-

pation efficiency based on energy and momentum conservation laws. Their Equation (51) can be written as

$$\eta = \frac{1}{1+\sigma_{\rm b,f}} - \frac{\Gamma_m(m_1+m_2)}{(\Gamma_1 m_1 + \Gamma_2 m_2)(1+\sigma_{\rm b,i})}, \tag{3.19}$$

where $\sigma_{\rm b,i}$ is the initial σ value of the two colliding blobs, $\sigma_{\rm b,f}$ is the final σ value after the inelastic collision is over, Γ_1, Γ_2, and Γ_m are the Lorentz factors of the two colliding blobs and the merged blob, respectively, and m_1, m_2 are the masses of the two colliding blobs. In our simulations, the two blobs are identical so that $m_1 = m_2$. Since we are observing in the merged frame so that $\Gamma_m = 1$, $\Gamma_1 = \Gamma_2 = \Gamma$, the final expression of the efficiency can be reduced to[2]

$$\eta = \frac{1}{1+\sigma_{\rm b,f}} - \frac{1}{\Gamma(1+\sigma_{\rm b,i})}. \tag{3.20}$$

In order to connect this analytical equation with our simulated results, we first carry out some analyses to see if the condition of complete inelastic collision is satisfied. For ideal MHD simulations, fluid elements are attached to the field lines. Tracking the evolution of magnetic field configuration is therefore a convenient way to study whether collision is inelastic. Figure 35 shows several contour cuts of the 3D field line evolution. Initially the fields are compressed around $t = 6$, and then bounce back around $t = 12$. Later strong collision-driven reconnections on the contact surface efficiently dissipate the compressed magnetic energy and reduce the magnetic pressure in the center. This prevents further bouncing back and reorganizes the field configuration to make the two blobs merge into one larger blob with a new field configuration with a "∞" shape at the final quasi-steady stage. This suggests that the two blobs merge to one entity after the collision.

[2]This can be also derived directly by writing energy and momentum conservations in center-of-mass rest frame.

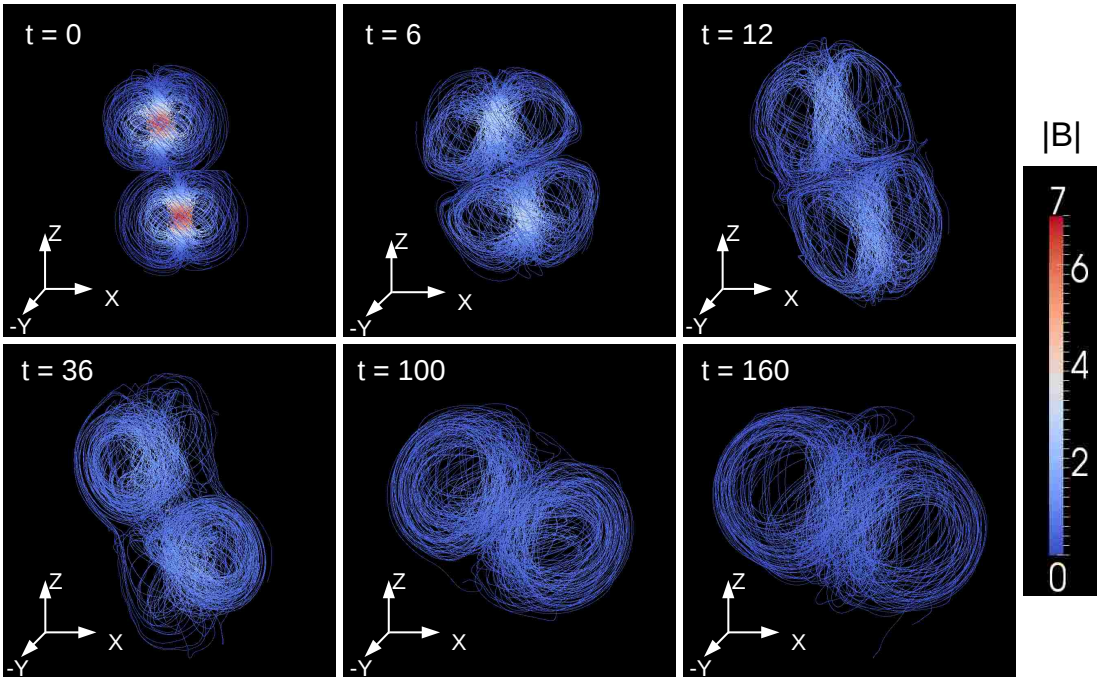

Figure 35 The evolution of the field lines during the collision process. The two blobs merge into one larger blob, forming a "∞"-shaped field line configuration at the final quasi-steady stage of the evolution. The color contour denotes the value of magnetic field strength $|B|$.

Due to the mis-alignment in X direction of the two blobs, the collision would induce rotation during the merging process. This would render the collision process not completely inelastic. In order to investigate how important the rotation effect is, we calculate the ratio between the rotation energy ($E_{\rm rot}$) and the initial kinetic energy ($E_{\rm k,i}$). The rotation energy of the two blobs can be estimated as $E_{\rm rot} = 2 \times (\frac{1}{2} I\omega^2)$, where the moment of inertia of one blob can be estimated as $I = \frac{2}{5}mr^2 + mr^2$, where the first term denotes the moment of inertia of an idea sphere, and the second term denote the displacement from the rotation axis. Since the blobs expand with time, the size of the blob and its displacement increase with time. We estimate that after the merging process, r is about three times of $r_0 = L_0 = 1$. We therefore derive $I \sim \frac{63}{5} m L_0^2 = \frac{63}{5} m$. For the angular velocity ω, we can estimate it from Figure 35, which shows a roughly $\pi/4$ angular change within $\Delta t = 90 L_0/c = 90$. As a result, one can estimate $\omega \sim \pi/360$, so that $E_{\rm rot} = 10^{-3} m$. The ratio between $E_{\rm rot}$ and $E_{\rm k,i}$ is therefore

$$\frac{E_{\rm rot}}{E_{\rm k,i}} = \frac{10^{-3} m}{2 \times \frac{1}{2} m V_{\rm b,z}^2} \approx 10^{-2}. \tag{3.21}$$

So the rotation energy is only a small fraction of the initial kinetic energy, which means that the collision is very close to completely inelastic collision for this example case with $x_s = 0.5$. While even if $E_{\rm rot}$ becomes a larger fraction of $E_{\rm k,i}$ when the mis-alignment x_s increases, it would only reduce the kinetic energy dissipation efficiency, but would have little direct effect on the $E_{\rm em}$ dissipation efficiency that is our primary concern[3]. Due to the initial high-σ property of the blobs, the contribution from the $E_{\rm k,i}$ dissipation to the total dissipation efficiency is only a minor fraction when $E_{\rm em}$ has significant dissipation, as we have found above.

With the above preparation, we can achieve a physical understanding of the high efficiency obtained from our simulation. Based on Eq.(3.20), we can derive the ex-

[3]However, the misalignment x_s itself does have a direct effect on the $E_{\rm em}$ dissipation efficiency due to the different field configurations around the initial contact surface. See details in Section §3.4.2.

pected efficiency. From the initial condition, we derive $\Gamma = 1.05$. From simulation results, we can also calculate $\sigma_{\rm b,f}$. Since $\sigma_{\rm b,f}$ has a complex spatial distribution, we perform a spatial average for all the positions with $\sigma_{\rm b,f} > 1$ and also perform a time average from $t = 90$ to $t = 120$ to get the $\sigma_{\rm b,f} \approx 1.16$. As a result, we derive $\eta \approx 35.7\%$ based on the analytical calculation (Eq.(3.20)). This is well consistent with the $E_{\rm em}$ dissipation efficiency calculated directly from the energy evolution of the simulations using Eq.(3.13), as shown in Figure 29.

3.3.6 Summary for this section

In this section, we revealed a collision-induced strong reconnection process with the EMF energy dissipation efficiency about 35%, which is resolution insensitive. The outflow can locally become super-Alfvénic during the initial strong compression stage. The outflow velocity can potentially become relativistic in higher resolution simulations and generate multi-orientation mini-jets in a global PFD jet.

3.4 Extended Parameter Space Studies

In Section §3.3, we find significant EMF energy dissipation (about 35%) facilitated by collision-driven magnetic reconnection. Based on the above analyses, we expect that some parameters may affect the results. First, the σ_b evolution controls the $E_{\rm em}$ dissipation efficiency. The simulation results may then depend on the initial value $\sigma_{\rm b,i}$. Second, the initial misalignment x_s gives different magnetic field configurations around the contact surface which may control the fraction of the free energy that can be released due to the reconnection processes. Next, different initial relative speed (kinetic energy) between the two blobs define the strengths of the initial collision-driven effect, so that it may be another factor to effect the conclusion. In addition, the initial displacement z_d controls the delay of the collision. It is also interesting to investigate whether results depend on this parameter. Furthermore, the blobs undergo

a significant expansion during the early "self adjustment" phase before establishing a balance between the magnetic pressure force and the gas pressure force. Different background pressures and densities are therefore interesting input parameters that may affect the results. Finally, it is unknown whether the toroidal-to-poloidal ratio parameter, α, plays a role to define the dissipation efficiency.

In this section, we perform a series of extended parameter studies to investigate the role of above-mentioned various parameters in defining the $E_{\rm em}$ dissipation efficiency and reconnection outflow properties. From the resolution study in Section §3.3.4, we find that the $E_{\rm em}$ dissipation efficiency is similar when the resolution is $\geqslant 256^3$. Since we are exploring a large parameter space, in order to reduce the simulation time, we use the 256^3 resolution in all the simulations presented in this section. The general approach is that we only modify one parameter from the example simulation in each subsection, in order to explore the effects of that parameter. Below we explore the effect of following parameters in turn: the initial σ value inside the blobs ($\sigma_{\rm b,i}$), the initial misalignment between the center of two blobs in X direction (x_s), the initial velocity ($V_{\rm b,z}$) or relative Lorentz factor ($\Gamma_{\rm rel}$) of two blobs in Z direction, the initial distance between the center of two blobs in Z direction (z_d), the uniform gas pressure (P), the background density ($\rho_{\rm bkg}$), the toroidal-to-poloidal magnetic field ratio α, and the adiabatic index ($\hat{\gamma}$).

3.4.1 Initial $\sigma_{\rm b,i}$ of the blobs

The $\sigma_{\rm b,i}$ parameter affects the σ_b evolution and the initial expansion of the blobs, so in this subsection we study the effect on the $E_{\rm em}$ energy evolution and dissipation efficiency for different $\sigma_{\rm b,i}$ values. We set a higher $\sigma_{\rm b,i}$ value by increasing the normalization parameter $B_{\rm b,0}$. The parameters we used are listed in Table 3. Here the parameters besides $\sigma_{\rm b,i}$ and $B_{\rm b,0}$ are the same as the example model. We choose three different $\sigma_{\rm b,i}$ values. Here, due to the more significant expansion with a increasing

$\sigma_{\rm b,i}$, we enlarge our simulation box to 30^3 and also increase the resolution to 384^3 to ensure the same absolute spatial resolution as the following sub-sections. The upper panel of Figure 36 shows the $E_{\rm em}$ evolution of these three models. Similar to the example model, we also show the non-collision case for each model to calculate the $E_{\rm em}$ dissipation efficiency. We find that with a higher $\sigma_{\rm b,i}$ value, the initial steep decay of $E_{\rm em}$ caused by the expansion is more significant due to the stronger outward magnetic pressure force. The $E_{\rm em}$ dissipation efficiency in the final quasi-steady phase, on the other hand, is rather similar for different $\sigma_{\rm b.i}$ values (lower panel of Figure 36). In order to understand this result, we also calculate the $\sigma_{\rm b,f}$ values in the quasi-steady phase, and use Eq.(3.20) to calculate η independently (see the method in Section §3.3.5). The results are shown in Table 4. The calculated efficiencies have no obvious difference among different cases, since a larger $\sigma_{\rm b,i}$ corresponds to a slightly larger $\sigma_{\rm b,f}$, so that η does not change significantly according to Eq.(3.20). This result is consistent with the efficiency calculated directly from the energy evolution of the simulations in the lower panel of Figure 36.

Model name	$\sigma_{\rm b,i}$	$B_{\rm b,0}$	α	$\lvert V_{\rm b,z}\rvert$	P	$\rho_{\rm bkg}$	z_d	x_s
Model:$\sigma_{\rm b,i}$8	8	$\sqrt{4\pi}$	3	0.3c	10^{-2}	10^{-1}	4.4	1.0
Model:$\sigma_{\rm b,i}$16	16	$\sqrt{8\pi}$	3	0.3c	10^{-2}	10^{-1}	4.4	1.0
Model:$\sigma_{\rm b,i}$24	24	$\sqrt{12\pi}$	3	0.3c	10^{-2}	10^{-1}	4.4	1.0

Table 3 The $\sigma_{\rm b,i}$-varying models

One interesting result is that $\sigma_{\rm b,i}$ and $\sigma_{\rm b,f}$ values show a good linear relationship (Figure 37), which can be fitted by

$$\sigma_{\rm b,f} = 0.02\sigma_{\rm b,i} + 1.0. \tag{3.22}$$

Physically, this equation does not apply for $\sigma_{\rm b,i} < 1$. Right now the range of the $\sigma_{\rm b,i}$ is relatively small limited by the code capability. It is valuable to perform a more detailed study for a larger range of $\sigma_{\rm b,i}$ in the future to test this interesting and

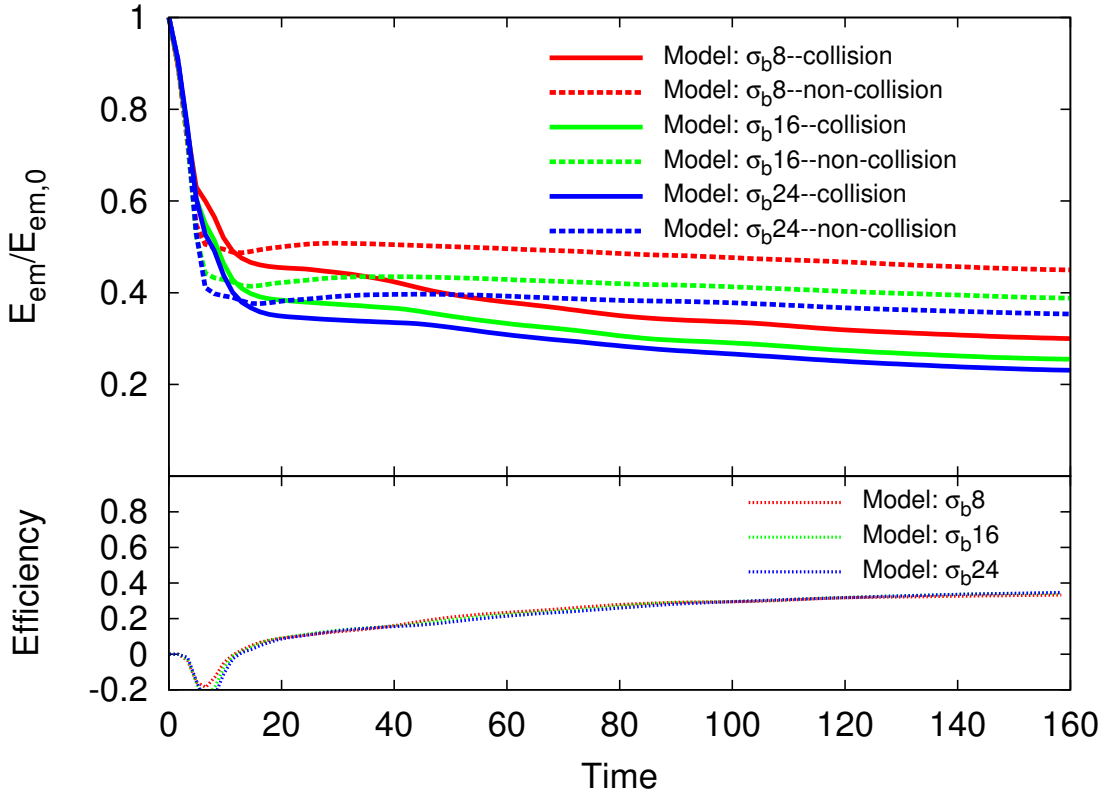

Figure 36 The $E_{\rm em}$ evolution of three $\sigma_{\rm b,i}$ models: $\sigma_{\rm b,i} = 8$ (red group), $\sigma_{\rm b,i} = 16$ (green group), and $\sigma_{\rm b,i} = 24$ (blue group). As the example model, we also show the non-collision cases corresponding to each of them to calculate the $E_{\rm em}$ dissipation efficiency. The $E_{\rm em}$ dissipation efficiency in the final quasi-steady phase is similar.

$\sigma_{b,i}$	$\sigma_{b,f}$	Efficiency (analytical)	Efficiency (numerical)
8	1.16	35.7%	33.3%
16	1.33	37.3%	34.4%
24	1.49	36.4%	34.7%

Table 4 $\sigma_{b,f}$ - $\sigma_{b,i}$ relation and the analytical vs. numerical efficiencies.

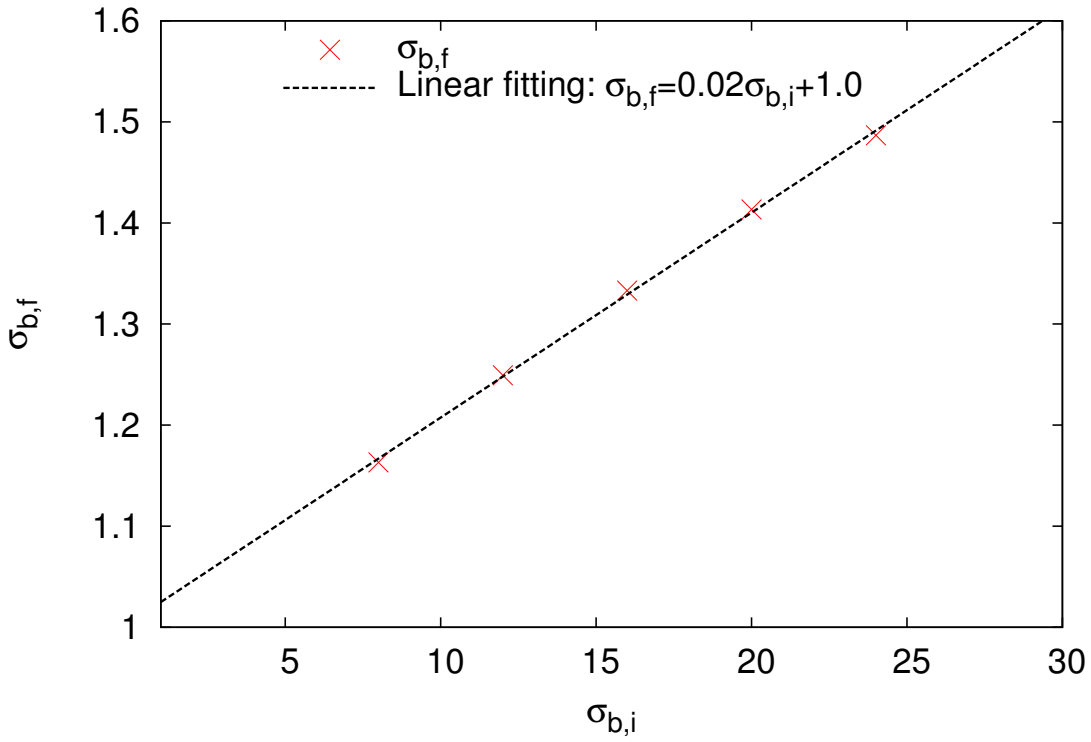

Figure 37 The relationship between $\sigma_{b,f}$ and $\sigma_{b,i}$. The red cross points are the calculated results of $\sigma_{b,f}$ corresponding to different $\sigma_{b,i}$ from our simulations. The black dashed line is the linear fitting result.

important relationship and to study the physical mechanism of this behavior.

3.4.2 Initial misalignment between two blobs (x_s)

The initial misalignment affects the magnetic field configuration around the contact surface during the collision and also the rotation property, so in this subsection we study the effect of x_s on the E_{em} energy evolution and dissipation efficiency. The parameters we used are listed in Table 5. Besides x_s, other parameters are the same as the example model. From the analyses in Section §3.3.5, the typical radius of

one blob after expansion is $r \approx 3r_0 = 3.0$. In order to make a relatively significant collision, x_s should be smaller than $2r \approx 6$. We choose seven different values of x_s in the simulations (Table 5). Among these models, "Model:x_s1.0" is the same as the example model with resolution 256^3.

The upper panel of Figure 38 shows the $E_{\rm em}$ evolution of these seven models. We find that, with increasing x_s, the $E_{\rm em}$ dissipation efficiency first increases, and then decreases after reaching the maximum efficiency around $x_s \approx 3.0$. Such a behavior can be understood using the two lower panels in Figure 28. The 2D cuts of B_x, B_y show the directions and strength distributions of these two components of the magnetic field. Due to the initial expansion, the actual size of these configuration during collision would become about three times larger than the initial cuts. We consider the anti-parallel regions as the free energy source for reconnection-induced dissipation. When $x_s = 0$, only the B_x component can be reconnected. With an increasing x_s from 0 to 3.0, the anti-parallel region of B_x becomes smaller while the anti-parallel region of B_y increases. Since the strength of B_y is larger than B_x, the total dissipated magnetic energy becomes larger, which increases the dissipation efficiency to a higher value. When $x_s = 3.0$, the anti-parallel region of B_y reaches the maximum so that the maximum efficiency is achieved. After this critical point, the anti-parallel region of B_y decreases with increasing x_s, which leads to a decrease in efficiency. Finally, when x_s becomes larger than the size of the two blobs (6.0), the $E_{\rm em}$ evolution is nearly the same as the non-collision case due to the lack of significant collision between the two blobs.

Another important feature is that the change of efficiency as a function of x_s is not linear. In fact, in our studied the cases only the two extreme cases $x_s = 0$ and $x_s = 7.0$ have significantly lower efficiencies compared with the other cases. Even if there is a very small misalignment, e.g. $x_s = 0.002$, the efficiency could become significantly larger than the $x_s = 0$ case. Inspecting the energy evolution plot (Fig.38), one can see

that the main difference comes from the "normal decay" phase. A smaller x_s would delay the "normal decay" phase to a later time, whereas there is no "normal decay" phase if $x_s = 0$. In order to understand this feature, we draw Figure 39. The three panels in the first row are the 2D contour cuts of $B^2/4\pi$ in the XZ-plane (y=0), corresponding to $t = 0$, $t = 80$, and $t = 120$ for "Model:x_s0.0", respectively. The following two panels in the second row are the 2D contour cuts of the y-component of the outflow velocity (V_y) in the YZ-plane (x=0), corresponding to $t = 80$ and $t = 120$ for "Model:x_s0.0". The following five panels are the corresponding cuts for the "Model:x_s0.002". One can see that for the complete alignment case ("Model:x_s0.0"), the two blobs merge together and enter the quasi-steady phase without an obvious reconnection feature. For "Model:x_s0.002", on the other hand, the merged blobs start to rotate at $t \sim 80$, which just corresponds to the starting time in the energy evolution plot (Fig.38) when the two models become distinctly different. The last panel of V_y in Figure 39 shows the feature of the reconnection-driven outflows during the "normal decay" phase of "Model:x_s0.002", which is not seen in "Model:x_s0.0[4]. From these analyses, we can draw conclusion that, besides the initial anti-parallel region caused by x_s, the collision-triggered rotation is another important process to change the magnetic field configuration and dissipate more magnetic energy. This rotation-driven dissipation seems to correspond to the "normal decay" phase in the energy evolution plot.

Model name	$\sigma_{\rm b,i}$	$B_{\rm b,0}$	α	$\lvert V_{\rm b,z}\rvert$	P	$\rho_{\rm bkg}$	z_d	x_s
Model:x_s0.0	8	$\sqrt{4\pi}$	3	0.3c	10^{-2}	10^{-1}	4.4	0
Model:x_s0.002	8	$\sqrt{4\pi}$	3	0.3c	10^{-2}	10^{-1}	4.4	0.002
Model:x_s0.02	8	$\sqrt{4\pi}$	3	0.3c	10^{-2}	10^{-1}	4.4	0.1
Model:x_s0.1	8	$\sqrt{4\pi}$	3	0.3c	10^{-2}	10^{-1}	4.4	1.0
Model:x_s1.0	8	$\sqrt{4\pi}$	3	0.3c	10^{-2}	10^{-1}	4.4	3.0
Model:x_s1.6	8	$\sqrt{4\pi}$	3	0.3c	10^{-2}	10^{-1}	4.4	5.0
Model:x_s1.6	8	$\sqrt{4\pi}$	3	0.3c	10^{-2}	10^{-1}	4.4	7.0

Table 5 The x_s-varying models

[4]The outflows look like asymmetric on that 2D cut, since the 3D configuration is more complex.

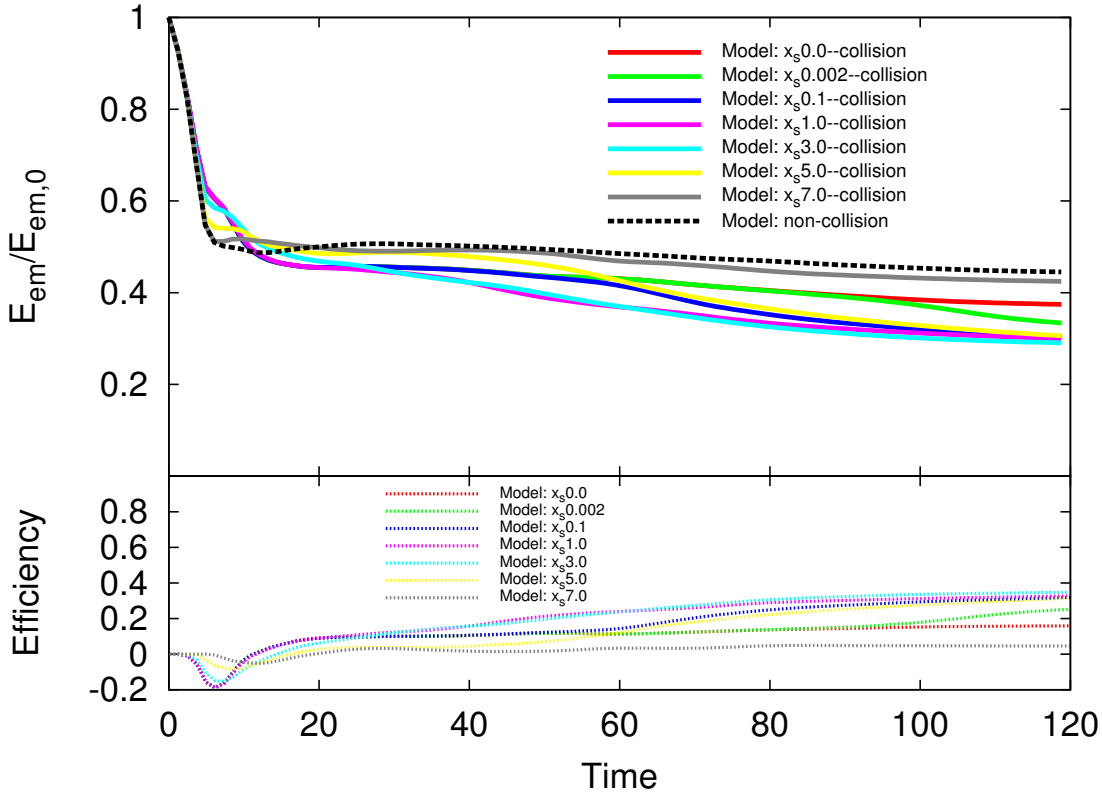

Figure 38 The $E_{\rm em}$ evolution of seven x_s models: $x_s = 0$ (red), $x_s = 0.002$ (green), $x_s = 0.1$ (blue), $x_s = 1.0$ (magenta), $x_s = 3.0$ (cyan), $x_s = 5.0$ (yellow), and $x_s = 7.0$ (gray). Similar to the example model, we also show the non-collision cases for each model to calculate the $E_{\rm em}$ dissipation efficiency. Since the non-collision case does not depend on x_s, there is only one non-collision evolution case (dashed line). Besides the $x_s7.0$ model which no collision is observed, Only the "$x_s0.0$" model has obvious difference in $E_{\rm em}$ dissipation efficiency, which is only about half of the other models in the final quasi-steady phase.

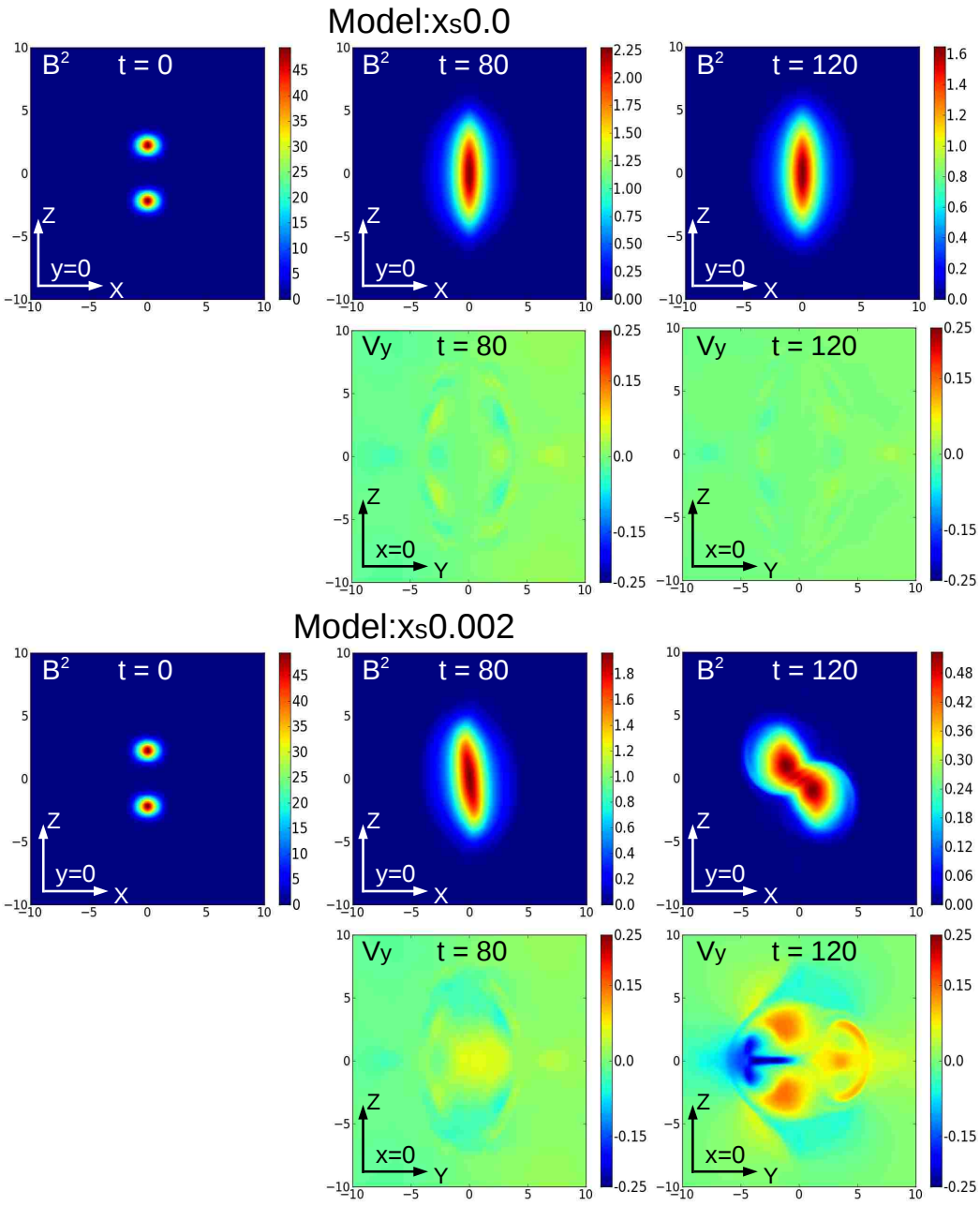

Figure 39 Selected cuts for model "Model:x_s0.0" (first two rows) and "Model:x_s0.002" (last two rows). For each model, we draw the 2D contour cuts of B^2 in the XZ-plane (y=0) at $t = 0$, $t = 80$ and $t = 120$ (higher row) and the 2D contour cuts of the y-component of outflow velocity (V_y) in the YZ-plane (x=0) at $t = 80$ and $t = 120$ (lower row). The results show that even if there is a very small misalignment, the merged blobs would start to rotate at some critical point and trigger additional reconnection-facilitated magnetic dissipation with significant outflow feature at late time.

3.4.3 Initial relative Lorentz factor ($\Gamma_{\rm rel}$) between the two blobs

A larger initial velocity $V_{\rm b,z}$ means a larger initial kinetic energy of the two blobs, which would provide a larger driving force initially and also effectively decrease $\sigma_{\rm b,i}$. In this subsection, we study the effect of $V_{\rm b,z}$ in detail. Since we are testing $V_{\rm b,z}$ in the relativistic regime, we adopt the relative Lorentz factor ($\Gamma_{\rm rel}$) between two blobs as the varying parameter. The relative Lorentz factor can be calculated as

$$\Gamma_{\rm rel} = 2\Gamma_{\rm b,z}^2 - 1, \tag{3.23}$$

where $\Gamma_{\rm b,z} = (1 - V_{\rm b,z}^2/c^2)^{-1/2}$ is the Lorentz factor of each blob.

The parameters we used are listed in Table 6. The parameters except $\Gamma_{\rm rel}$ and $\sigma_{\rm b,i}$ are the same as the example model. The effective change of $\sigma_{\rm b,i}$ is a consequence of changing $\Gamma_{\rm rel}$, since we keep B as observed in the center-of-mass frame as constant. We choose three different $\Gamma_{\rm rel}$ values. With an increasing $\Gamma_{\rm rel}$, the fraction of the initial kinetic energy becomes larger, so that $\sigma_{\rm b,i}$ effectively decreases. The upper panel of Figure 40 shows the $E_{\rm em}$ evolution of these three models. As $\Gamma_{\rm rel}$ increases, due to the stronger dynamic process, the initial "self adjustment" phase becomes more significant. In particular, for $\Gamma_{\rm rel} = 18.8$, the fast motion generates a strong shock into the surrounding medium. The shock compresses the magnetic field even further, so that $E_{\rm em}$ reaches an even higher value initially. In addition, from the lower panel of Figure 40, we find that the $E_{\rm em}$ dissipation efficiency in the final quasi-steady phase increases with increasing $\Gamma_{\rm rel}$. This is because a higher initial $\Gamma_{\rm rel}$ carries a larger kinetic energy and gives a stronger initial collision-induced compression and reconnection-induced dissipation.

Model name	$\sigma_{\rm b,i}$	$B_{\rm b,0}$	α	$\Gamma_{\rm rel}$	P	$\rho_{\rm bkg}$	z_d	x_s
Model:Γ_{rel}1.2	9	$\sqrt{4\pi}$	3	1.2	10^{-2}	10^{-1}	4.4	1.0
Model:Γ_{rel}5.6	6	$\sqrt{4\pi}$	3	5.6	10^{-2}	10^{-1}	4.4	1.0
Model:Γ_{rel}18.8	3	$\sqrt{4\pi}$	3	18.8	10^{-2}	10^{-1}	4.4	1.0

Table 6 The $\Gamma_{\rm rel}$-varying models

3.4.4 Initial distance between two blobs (z_d)

The initial distance between the center of two blobs in z direction (z_d) controls the delay of the collision. In our example case, z_d is relatively small and the collision happens around the middle stage of the initial expansion. It is valuable to study the effect on the $E_{\rm em}$ energy evolution and dissipation efficiency when we set a larger z_d to delay the collision time to a later stage. The parameters we used are listed in Table 7. Here the parameters except z_d are the same as the example model. We choose three different z_d values. The "Model:z_d4.4" uses $z_d = 4.4$ which is the same as the example model with resolution 256^3, and the other two models, "Model:z_d6" and "Model:z_d8", have $z_d = 6, 8$, respectively. The upper panel of Figure 41 shows the $E_{\rm em}$ evolution of these three models. The collision times of these three different z_d models are designated to be around the middle and late stages of initial expansion as well as after the initial expansion, respectively. We find that the reconnection-triggered $E_{\rm em}$ dissipation process is systematically delayed when z_d becomes larger. However, the efficiency at the final quasi-steady phase reaches a similar value (lower panel of Figure 41) in all three models. This result suggests that the dissipation efficiency does not sensitively depend on the stage of blob evolution.

3.4.5 Background gas pressure (P)

The blobs undergo a significant initial expansion to establish a balance between the magnetic pressure and the ambient gas pressure. Different background pressure (P) and density ($\rho_{\rm bkg}$) would affect these processes. In this and next subsections, we study the effect of P and $\rho_{\rm bkg}$ on the $E_{\rm em}$ energy evolution and dissipation efficiency. The

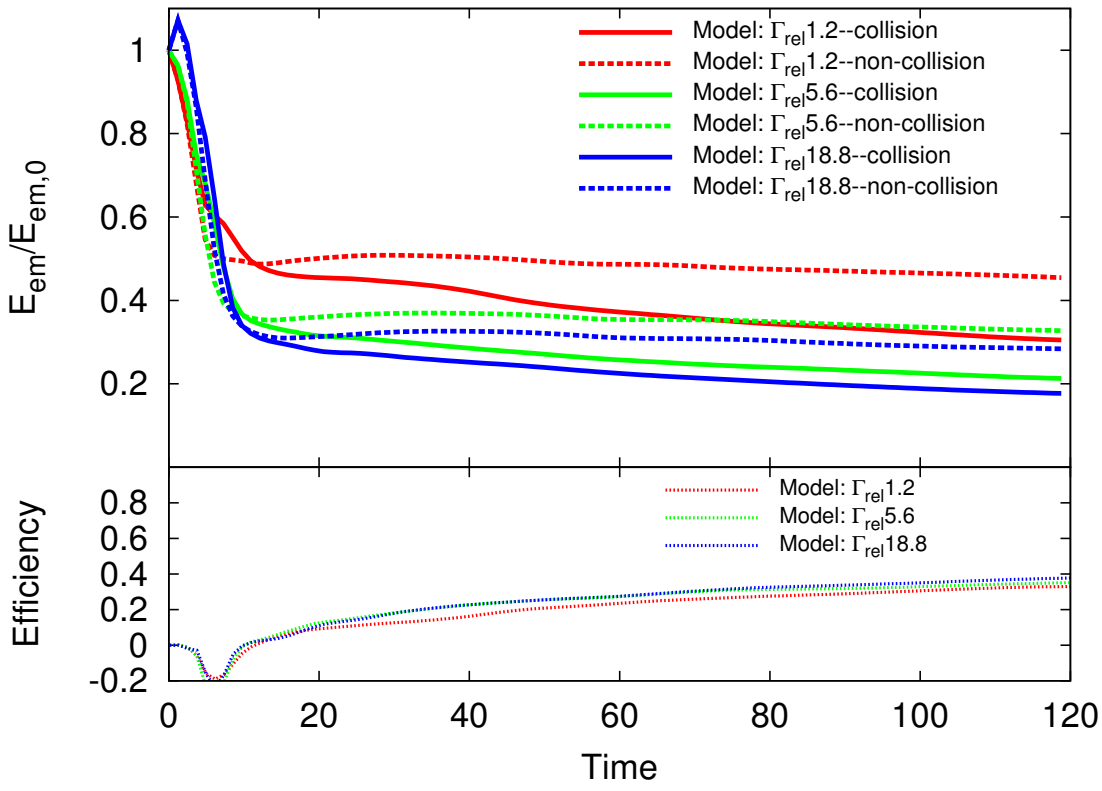

Figure 40 The $E_{\rm em}$ evolution of four $\Gamma_{\rm rel}$ models: $\Gamma_{\rm rel} = 1.2$ (red), $\Gamma_{\rm rel} = 5.6$ (green), and $\Gamma_{\rm rel} = 18.8$ (blue). Similar to the example model, for each model, we also show the non-collision case (dashed) to calculate the $E_{\rm em}$ dissipation efficiency. the $E_{\rm em}$ dissipation efficiency is larger for the model with a larger $\Gamma_{\rm rel}$.

Model name	$\sigma_{\rm b,i}$	$B_{\rm b,0}$	α	$\lvert V_{\rm b,z}\rvert$	P	$\rho_{\rm bkg}$	z_d	x_s
Model:z_d4.4	8	$\sqrt{4\pi}$	3	0.3c	10^{-2}	10^{-1}	4.4	1.0
Model:z_d6	8	$\sqrt{4\pi}$	3	0.3c	10^{-2}	10^{-1}	6	1.0
Model:z_d8	8	$\sqrt{4\pi}$	3	0.3c	10^{-2}	10^{-1}	8	1.0

Table 7 The z_d-varying models

parameters for the P-varying models are listed in Table 8. Here the parameters other than P are the same as the example model. We choose three pressure values. The "Model:P-2" is the same as the example model with resolution 256^3, and the other two models have a lower (Model:P-1) or higher (Model:P-3) pressure. The upper panel of Figure 42 shows the $E_{\rm em}$ evolution of these three models. The initial "self adjustment" phase due to the expansion is more significant when pressure becomes lower, since for a lower background pressure it takes longer for the magnetic blob to expand before reaching a balance with the ambient gas, and vice versa. Even with very different blob dynamics for different pressure values, the difference of $E_{\rm em}$ dissipation efficiency in the final quasi-steady phase is not so large as the $E_{\rm em}$ evolution itself (lower panel of Figure 42), which means that the efficiency is relatively insensitive to the expansion process. This is probably due to the fact that the initial expansion phase with different background pressure values affects the evolution of both the collision and non-collision cases to similar degrees, so that the relative difference (efficiency) does not have a significant change.

3.4.6 Background density ($\rho_{\rm bkg}$)

The parameters for $\rho_{\rm bkg}$-varying models are listed in Table 9. Here most of the parameters are similar to the example model. However, in order to make the code stable when applying a smaller background density, we have to increase the uniform gas pressure value to 10^{-1}. We choose two density values. The upper panel of Figure 43 shows the $E_{\rm em}$ evolution of these two models. There is no significant difference between these two models. This is understandable. Since the force balance is mainly

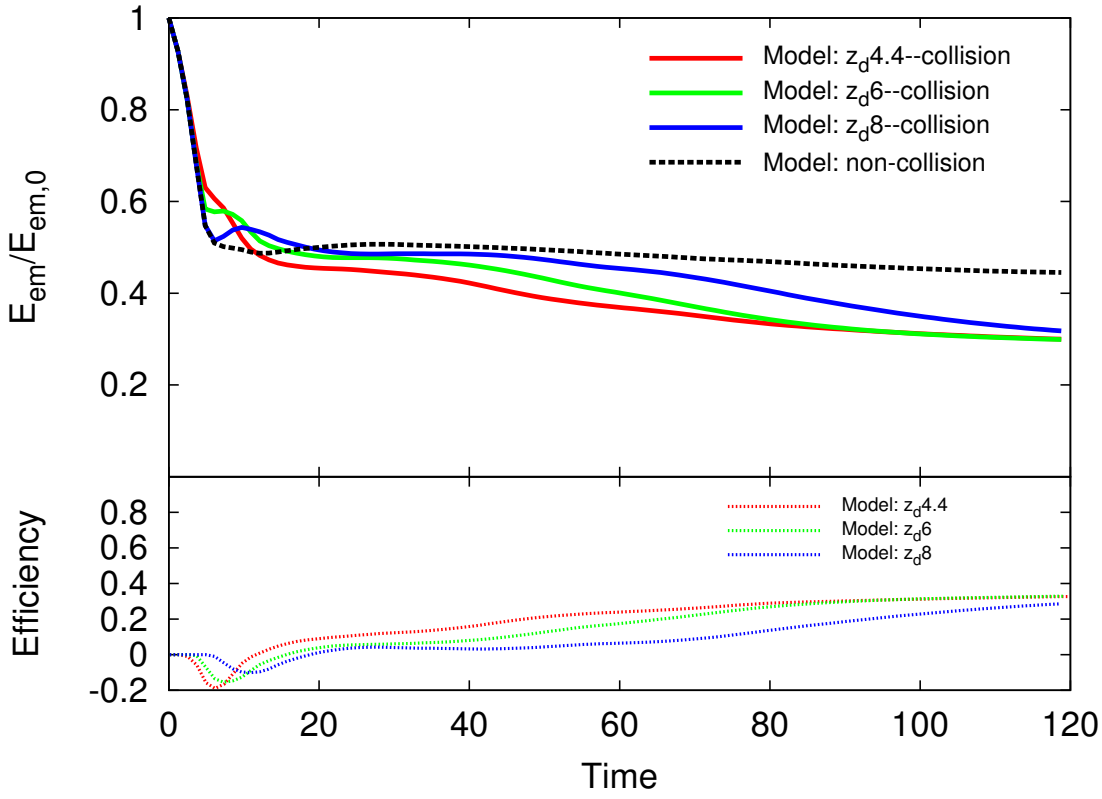

Figure 41 The $E_{\rm em}$ evolution of three z_d models: $z_d = 4.4$ (red), $z_d = 6$ (green), and $z_d = 8$ (blue), which correspond to the collision happening at different stage of the blob evolution. Similar to the example model, the non-collision case (black dashed, the same for all three models) is plotted for comparison. Although the reconnection facilitated dissipation is delayed when z_d increases, the energy level and the $E_{\rm em}$ dissipation efficiency in the final quasi-steady phase are similar.

Model name	$\sigma_{\rm b,i}$	$B_{\rm b,0}$	α	$\lvert V_{\rm b,z}\rvert$	P	$\rho_{\rm bkg}$	z_d	x_s
Model:P-1	8	$\sqrt{4\pi}$	3	0.3c	10^{-1}	10^{-1}	4.4	1.0
Model:P-2	8	$\sqrt{4\pi}$	3	0.3c	10^{-2}	10^{-1}	4.4	1.0
Model:P-3	8	$\sqrt{4\pi}$	3	0.3c	10^{-3}	10^{-1}	4.4	1.0

Table 8 The P-varying models

controlled by the background gas pressure rather than density, varying the background density does not lead to significant change in the result.

3.4.7 α value

The α parameter (introduced in Eq.(3.9)) controls the ratio between the toroidal and poloidal components of the initial magnetic field configuration. In the example model, we adopted $\alpha = 3$, which means that the toroidal flux roughly equals to the poloidal flux. On the other hand, the central engine of GRBs (and probably AGNs as well) is likely rapidly rotating, so that the toroidal flux may be (much) larger than the poloidal flux and $\alpha > 3$. In this subsection we study the effect of α on the $E_{\rm em}$ energy evolution and dissipation efficiency. The parameters we used are listed in Table 10. Here the parameters other than α are the same as the example model. We choose two α values (3 and 8). The upper panel of Figure 44 shows the $E_{\rm em}$ evolution of these two models. The initial "self adjustment" phase due to the expansion is more significant when α becomes higher, since the net magnetic pressure becomes larger when α increases (Li et al., 2006). This requires more expansion of the blobs before reaching the pressure balance with the ambient gas. The lower panel of Figure 44 shows the $E_{\rm em}$ dissipation efficiency of these two models. The model with a higher α value has a slightly higher efficiency. This is probably because the reconnections mainly come from the toroidal component. If α is much greater than 3 in realistic astrophysical systems (e.g. in GRBs and AGNs), the efficiency derived here can be regarded as a safe lower limit.

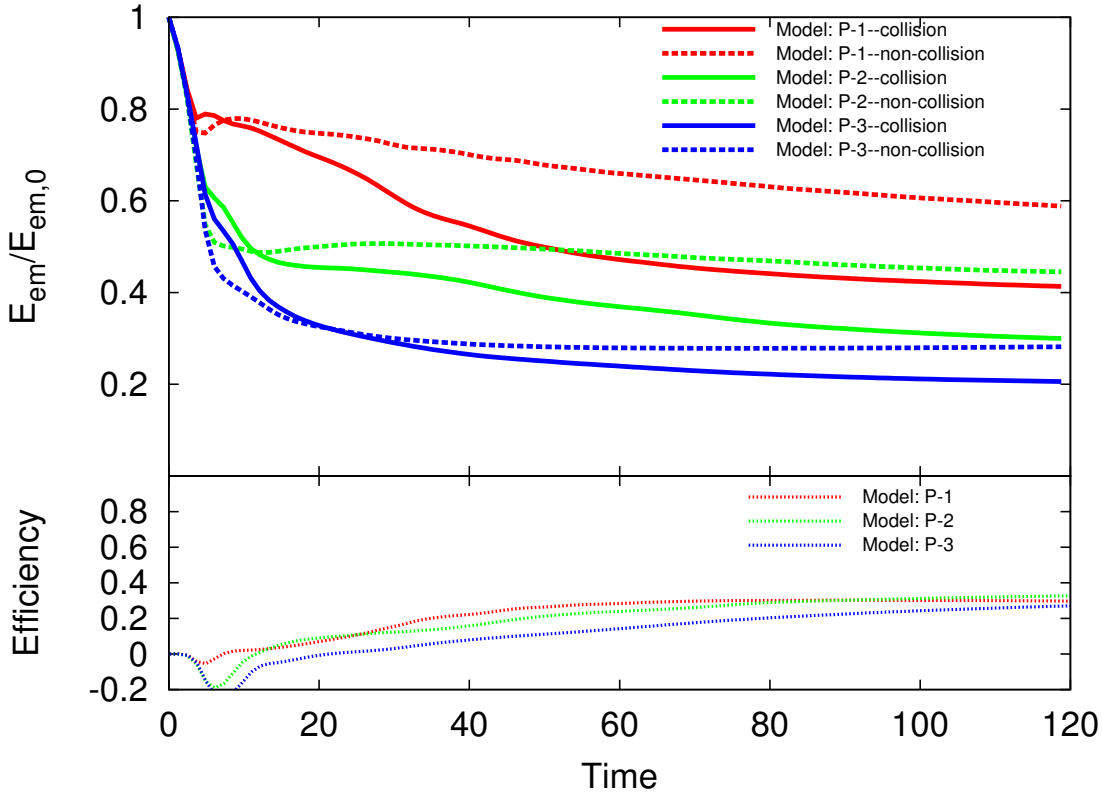

Figure 42 The $E_{\rm em}$ evolution of three pressure models: $P = 10^{-1}$ (red), $P = 10^{-2}$ (green) and $P = 10^{-3}$ (blue). Similar to the example model, we also show the non-collision cases (dashed lines) corresponding to each pressure model to calculate the $E_{\rm em}$ dissipation efficiency. Although the initial "self adjustment" phase due to the expansion becomes more significant when the pressure goes to lower values, the difference of efficiency in the final quasi-steady phase is relative small.

Model name	$\sigma_{\rm b,i}$	$B_{\rm b,0}$	α	$\lvert V_{\rm b,z}\rvert$	P	$\rho_{\rm bkg}$	z_d	x_s
Model:$\rho_{\rm bkg}$-1	8	$0.8\sqrt{4\pi}$	3	0.4c	10^{-1}	10^{-1}	4.4	1.0
Model:$\rho_{\rm bkg}$-3	8	$0.8\sqrt{4\pi}$	3	0.4c	10^{-1}	10^{-3}	4.4	1.0

Table 9 The $\rho_{\rm bkg}$-varying models

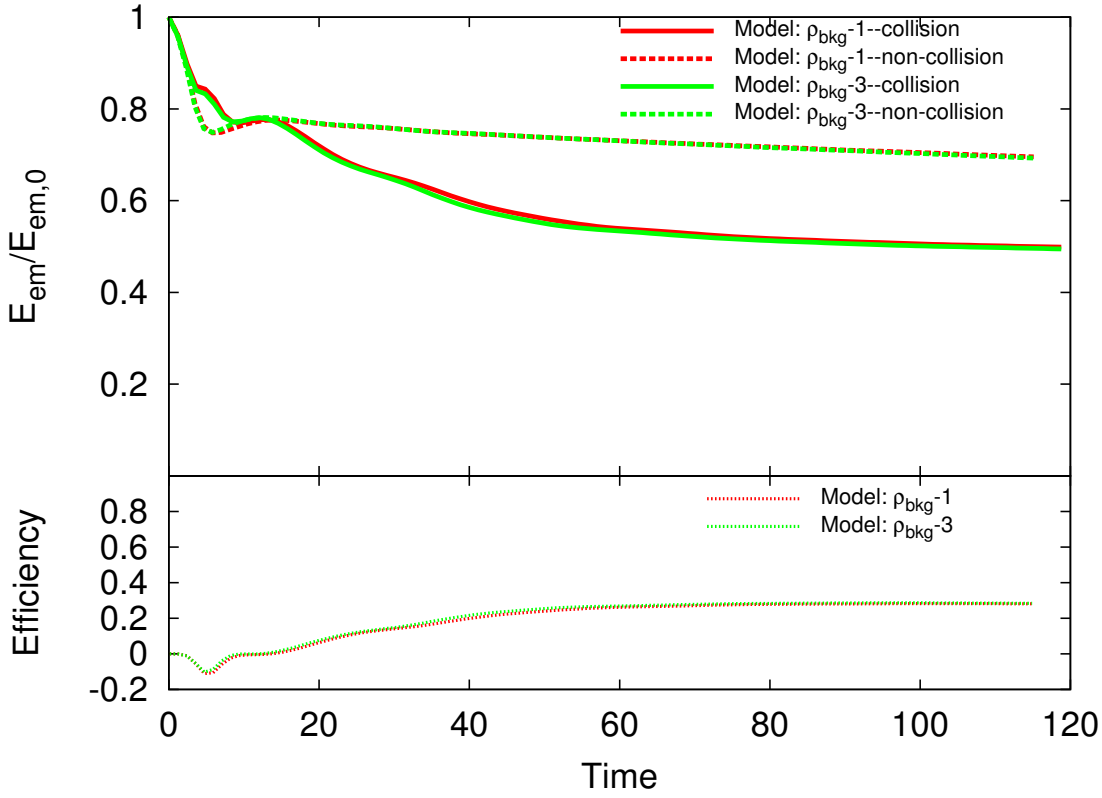

Figure 43 The $E_{\rm em}$ evolution of two density models: $\rho_{\rm bkg} = 10^{-1}$ (red), and $\rho_{\rm bkg} = 10^{-3}$ (green). Similar to the example model, the non-collision cases are also plotted (dashed). There is essentially no difference between the two models.

Model name	$\sigma_{\rm b,i}$	$B_{\rm b,0}$	α	$\lvert V_{\rm b,z}\rvert$	P	$\rho_{\rm bkg}$	z_d	x_s
Model:α3	8	$\sqrt{4\pi}$	3	0.3c	10^{-2}	10^{-1}	4.4	1.0
Model:α8	8	$\sqrt{4\pi}$	8	0.3c	10^{-2}	10^{-1}	4.4	1.0

Table 10 The α-varying models

3.4.8 Adiabatic index

Finally, in all above simulations we have used a simple uniform adiabatic index $\hat{\gamma} = 5/3$, since most of the regimes are at most mildly relativistic. Nonetheless, in some high temperature regimes in the reconnection outflows, the adiabatic index may be close to the relativistic limit $\hat{\gamma} = 4/3$. In principle, for a more accurate

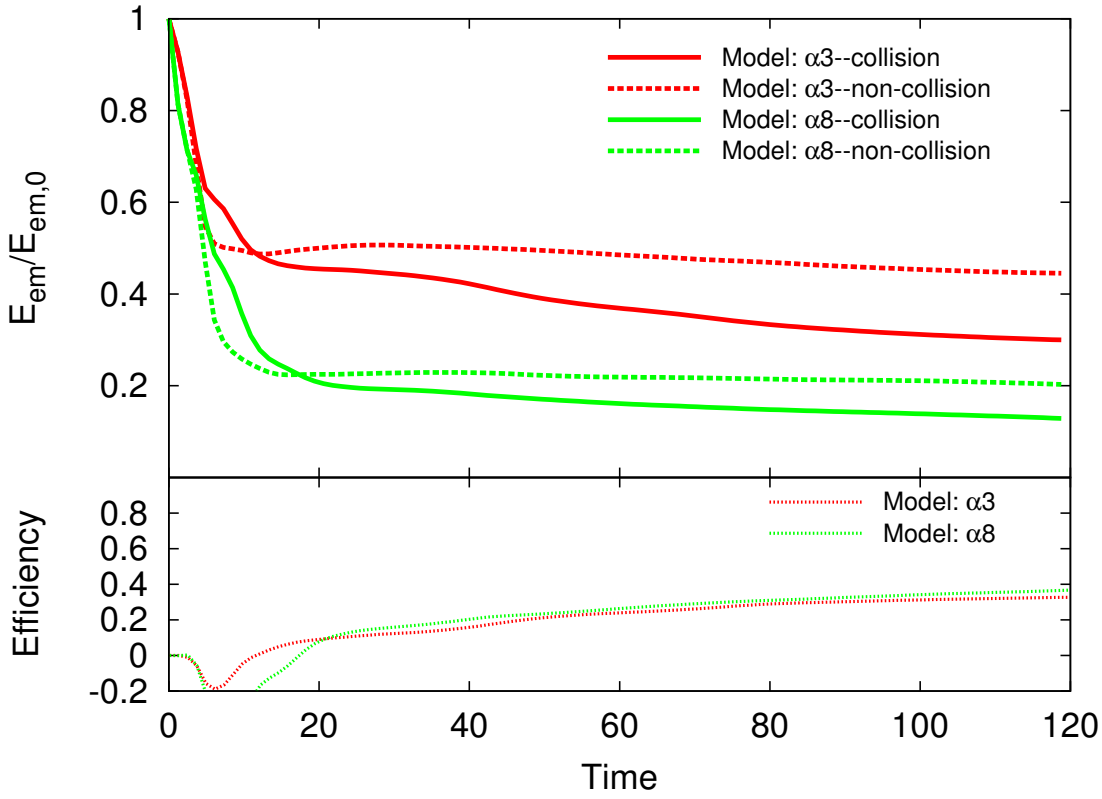

Figure 44 The $E_{\rm em}$ evolution of two α models: $\alpha = 3$ (red) and $\alpha = 8$ (green). Similar to the example model, the non-collision cases for each model (dashed) are also plotted. The $E_{\rm em}$ dissipation efficiency is slightly larger for the model with a larger α.

study, we need to calculate the adiabatic index between 5/3 to 4/3 based on the temperature distribution and time evolution cell by cell. In this subsection, based on the simplified uniform adiabatic index model, we compare the difference between these two limits: $\hat{\gamma} = 5/3$ and 4/3. We name them as "Model:adi 5/3" and "Model:adi 4/3", respectively. The parameters that we used are listed in Table 11. The "Model:adi 5/3" is just the example case with resolution 256^3. The upper panel of Figure 45 shows the $E_{\rm em}$ evolution of these two models. Similar to the example model, we also show the non-collision case for "Model:adi 4/3". We find that there is only a slight difference between these two models. We therefore conclude that the simple uniform adiabatic index model with $\hat{\gamma} = 5/3$ catches the essence of the collision and magnetic dissipation physics discussed in this Chapter.

Model name	$\hat{\gamma}$	$\sigma_{\rm b,i}$	$B_{\rm b,0}$	α	$\lvert V_{\rm b,z}\rvert$	P	$\rho_{\rm bkg}$	z_d	x_s
Model:adi 5/3	5/3	8	$\sqrt{4\pi}$	3	0.3c	10^{-2}	10^{-1}	4.4	1.0
Model:adi 4/3	4/3	8	$\sqrt{4\pi}$	3	0.3c	10^{-2}	10^{-1}	4.4	1.0

Table 11 Two $\hat{\gamma}$ models

3.4.9 Summary for this section

In this section, we have done a series of extended parameter studies. We find that the $E_{\rm em}$ dissipation efficiency is relatively insensitive to the variations of most parameters compared with the $E_{\rm em}$ evolution itself. We conclude that the two conclusions drawn in Section §3.3, namely, a high collision-triggered magetic dissipation efficiency and the existence of reconnection-facilitated outflow minijets, are robust.

3.5 Multiple Collisions

So far we have only studied collisions between two high-σ blobs. In reality, multiple collisions between several or even tens of blobs may occur in GRB/AGN jets, so that a much more complex configuration in the collision regions with multiple re-

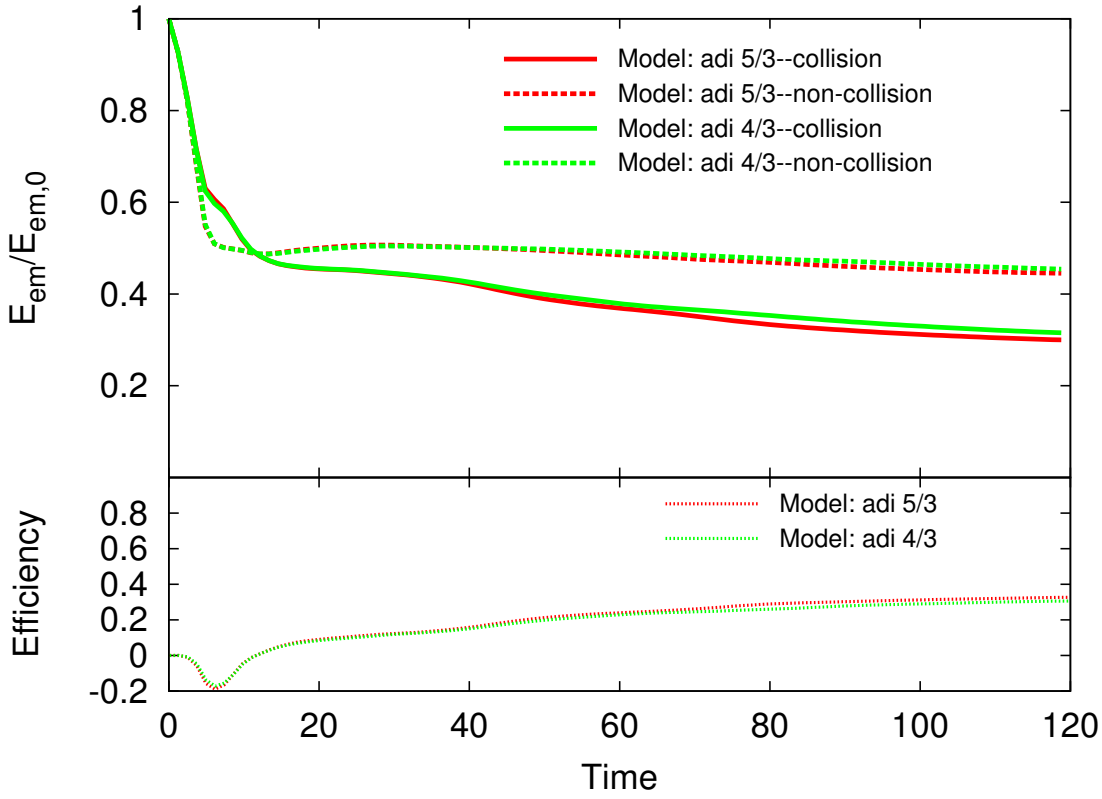

Figure 45 The $E_{\rm em}$ evolution of two $\hat{\gamma}$ models: $\hat{\gamma} = 5/3$ (red) and $\hat{\gamma} = 4/3$ (green). The non-collision cases (dashed) for both models are also shown. The $E_{\rm em}$ evolution and dissipation efficiency are similar for these two models.

connection layers and outflows can be achieved (as envisaged in the ICMART model, Zhang & Yan 2011). Simulating multiple collisions with random blobs are technically heavy duty and require extended simulation efforts. Nonetheless, in this section, we present a preliminary four-blob interaction simulation as the first step towards a more realistic/complicated study of multiple-blob collisions.

The size of the simulation box is $20 \times 20 \times 40$ with resolution $256 \times 256 \times 512$, which means that the grid size is the same as the example case of two blobs with resolution 256^3 in Section §3.3. The parameters used in the simulation are listed in Table 12. Here most of the parameters are the same as the example model. The different ones include the initial velocities of the four blobs and the distances between blobs. For the four blobs along the $+Z$ direction (bulk motion direction of the global jet) in the simulation frame (center-of-mass frame of the blobs), the velocities are $0.8c$, $0.3c$, $-0.3c$, and $-0.8c$, respectively. The initial distances between them are 5, 15, and 5, respectively, which means that the inner two blobs would collide with their nearby outer neighbors first to form two merged knots, before the two knots collide again. Figure 46 shows the 3D contour plots of the current, and the corresponding 2D contour cuts of the y-component of the outflow velocity(V_y) in the YZ-plane (x=0). At $t = 28$ the first collisions between the two pairs of outside blobs form two strong reconnection regions which are similar to the example model in §3.3. At later times, these two post-collision knots collide again and form a third strong reconnection region in the middle, and the original two reconnection regions also continuously evolve with time. These three reconnection regions form a more complex configuration than the collision with only two blobs as studied in §3.3.

The upper panel of Figure 47 shows the $E_{\rm em}$ evolution of this case. For comparison, we also show the non-collision case and the two-blob collision case (with same resolution), and calculate the $E_{\rm em}$ dissipation efficiency. We find that the $E_{\rm em}$ dissipation efficiency in the final quasi-steady phase is around 40%, which is higher

than the example two-blob case with resolution 256^3 (lower panel of Figure 47). This suggests that multiple collisions can facilitate further reconnection-triggered magnetic dissipations, making the system reaching a higher $E_{\rm em}$ dissipation efficiency.

Model name	$\sigma_{\rm b,i}$	$B_{\rm b,0}$	α	$V_{\rm b,z}$	P	$\rho_{\rm bkg}$	z_d	x_s
Model: 4 blobs	8	$\sqrt{4\pi}$	3	0.8c/0.3c/-0.3c/-0.8c	10^{-2}	10^{-1}	5/15/5	1.0

Table 12 The four-blob collision model

3.6 Conclusions and Astrophysical Applications

In this Chapter, using a 3D SRMHD code, we carried out a series of simulations to study collisions between high-σ magnetic blobs. Through a detailed example simulation and an extended parameter space survey, we have reached the following robust results:

- Collisions trigger significant EMF energy dissipation. Detailed analyses of the numerical data during different stages of the collision process suggest that such dissipation is facilitated by collision-induced magnetic reconnection. The efficiency of $E_{\rm em}$ dissipation in our simulations is around 35%, which is insensitive to the numerical resolution and several initial condition parameters, such as $\sigma_{\rm b,i}$, $\Gamma_{\rm rel}$, z_d, P, and $\rho_{\rm bkg}$. It depends on the impact parameter x_s, which defines the area of the anti-parallel regions in the contact surface of the two blobs. As long as a small offset exists, significant dissipation is facilitated.

- Our simulations suggest that the collision process is essentially inelastic. Even though there is some kind of bouncing back in the early stage of the collision evelution, the strong reconnection effect in the contact surface efficiently dissipates the magnetic energy and reduces the magnetic pressure. As a result, the two high-σ blobs merge into one larger blob with a "∞"-shaped magnetic configuration (see more details in Section §3.3.5). Assuming complete inelas-

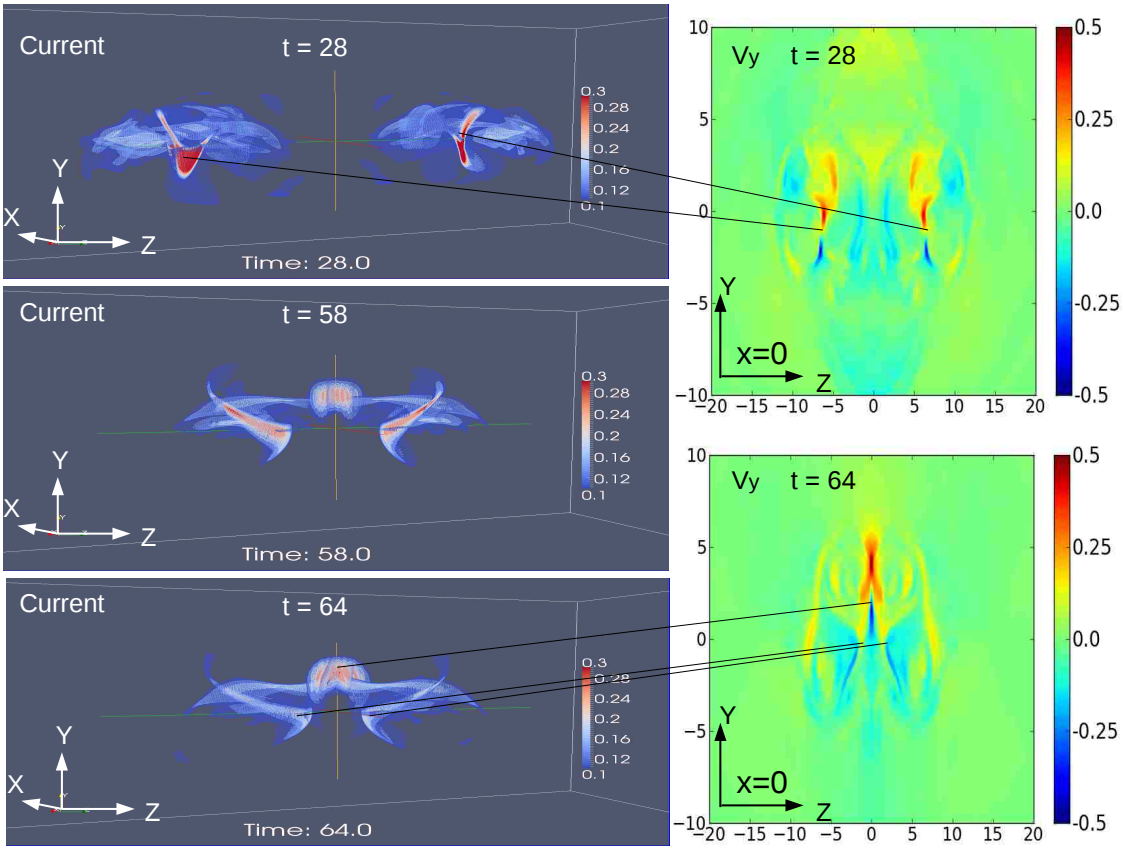

Figure 46 Some results of the four-blob collision simulation. The three left panels are the 3D contour plots of the currents at $t = 28$, $t = 58$ and $t = 64$, respectively. The two right panels are the corresponding 2D contour cuts of V_y in the YZ-plane (x=0) at $t = 28$ and $t = 64$, which are shrunk in z direction. The black lines indicate the corresponding positions of strong current layers and outflows. At least three strong reconnection layers with different directions are formed during the collision process.

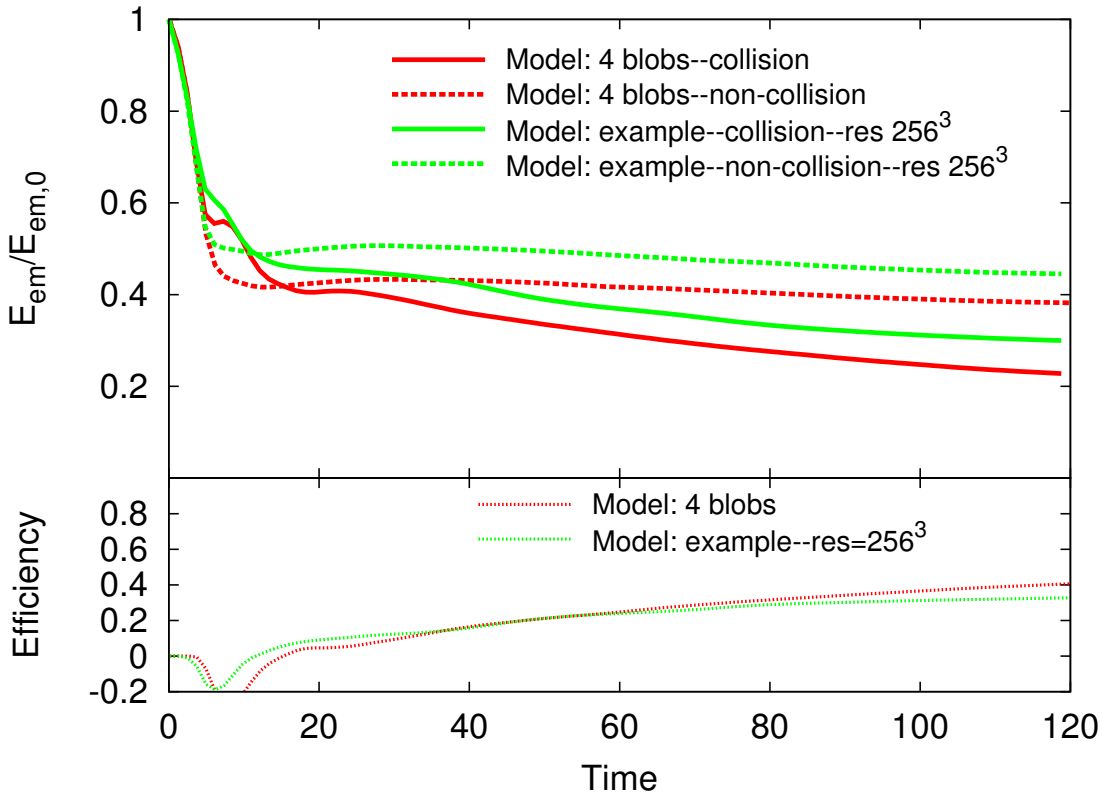

Figure 47 The $E_{\rm em}$ evolution of four-blob model compared with the two-blob model at resolution 256^3. For comparison, the non-collision model is also shown. The $E_{\rm em}$ dissipation efficiency in the final quasi-steady phase for the four-blob model is significantly higher than that of the two-blob model.

tic collision, an estimated dissipation efficiency (Zhang & Yan, 2011) is found consistent with the efficiency derived from the numerical data.

- From our simulations, we find that magnetic reconnection events can induce relativistic, multi-orientation outflows. Even in two-blob simulations, as long as an offset exists ($x_s \neq 0$), 3D outflows are formed. For four-blob collisions, significant outflows exist in three distinct regions. These outflows would mimic "mini-jets" as invoked in the astrophysical models of GRBs and AGNs. The maximum outflow velocity ($V_{\rm out}$) in our simulations is only $0.75c$. However, due to the significant resolution-dependence behavior as described in Section §3.3.4, we still have not reached the convergence for the outflow velocity, so that that value is only the lower limit of $V_{\rm out}$. In the simulations, we found that $\Gamma_{\rm out}$ can reach and even exceed local $\Gamma_{\rm A}$ and $\Gamma_{\rm ms}$ (§3.3.3), both are relativistic numbers if $\sigma > 1$. Also a larger $\Gamma_{\rm rel}$ tends to give a larger $V_{\rm out}$ value. In principle, with a high-resolution simulation and for a large $\sigma_{\rm b,i}$ and $\Gamma_{\rm rel}$, an even larger mini-jet Lorentz factor is achievable.

- We found an interesting linear relationship between the initial ($\sigma_{\rm b,i}$) and the finial ($\sigma_{\rm b,f}$) values of the σ parameter of the blob (Eq.(3.22)). The range of $\sigma_{\rm b,i}$ we have explored is not very large due to the code capability constraint. It is valuable to study this intriguing behavior in a larger range of $\sigma_{\rm b,i}$ in the future.

- Our preliminary simulations of multiple collisions among multiple high-σ blobs suggest that the collisions would give rise to more complex configurations of the reconnection layers and multi-orientation outflows, with a higher EMF energy dissipation efficiency. This suggests that the multiple collisions of many high-σ blobs can potentially generate many mini-jets with relatively random directions, as required by some theoretical models of astrophysical jets.

These numerical simulations have profound implications to understand astrophysical jets, such as GRBs, AGNs, X-ray binaries, Crab nebula, and so on. In the following, we discuss their direct applications to GRB and AGN models.

3.6.1 GRBs

As we mentioned in the introduction section, Zhang & Yan (2011) proposed the ICMART model to interpret the prompt emission of GRBs. This model invokes collision-induced magnetic dissipation of moderately high-σ blobs, which is the motivation of our simulations. The ICMART model was suggested to have several salient features that can potentially interpret various observations not easy to interpret within the MDF internal shock models. Our simulations verified several assumptions/speculations adopted in the original model of Zhang & Yan (2011).

First, Zhang & Yan (2011) claimed that ICMART processes should have a significantly higher energy dissipation efficiency than internal shocks, which is more consistent with the GRB observations (Panaitescu & Kumar, 2002; Zhang et al., 2007). They assumed that once ICMART is triggered, the two colliding shells would merge completely in an inelastic collision. The σ values of the two shells/blobs drop significantly from an initial value to a much lower final value. Energy and momemtum conservations suggest that the energy dissipation efficiency is high, up to 10s of percent, depending on the final σ value of the merged blob. If $\sigma_{\rm b,f} \sim 1$, they found that the efficiency is close to 50%. Our detailed simulations verified all these assumptions/speculations. Indeed significant magnetic dissipation occurs due to collision-induced magnetic reconnection. The collision process is essentially inelastic, and the energy dissipation efficiency is indeed high, which is $\sim 35\%$ for two-blob collisions and $\sim 40\%$ for four-blob collisions. One surprising result is that the final value $\sigma_{\rm b,f}$ is linearly correlated with the intial value $\sigma_{\rm b,i}$ (Eq.(3.22)), so that the efficiency does not sensitively depend on $\sigma_{\rm b,f}$. More studies are needed to reveal the underlying physics

of this correlation.

Second, the ICMART model invokes the central engine activities to interpret the broad pulses in the GRB light curves, but requires the existence of mini-jets to account for the rapid variability component. Zhang & Zhang (2014) used this concept to perform a series of Monte Carlo simulations and reproduced a range of highly variable light curves with both slow and fast components as seen in observational data (Gao et. al., 2012). The required Lorentz factor of the mini-jets is in the range of 2-15 (Zhang & Zhang, 2014). In our simulations, the outflows of reconnection layers can reach mildly relativistic speed. From the orientation point of view, one major reconnection current layer between two colliding blobs already generates multi-orientation outflows (see Figure 30), in addition to systematical global rotation and twist due to the slightly initial misalignment. Furthermore, by invoking four-blob collisions, we clearly find three major reconnection layers with different directions. Each of them has their own 3D outflow systems similar to two-blob collision cases, which gives a more complex space-time distribution of the outflow directions. In realistic systems, collisions of tens of blobs would lead to more complicated 3D mini-jet structure, which would account for observed GRB light curves. It is possible in much smaller scales not resolved by the current simulations, perturbations may induce turbulent reconnections, which may make even smaller mini-jets in the current outflows. Dedicated local simulations are needed to verify or refute such a speculation. With the current global simulations, one is confident that even without turbulence, collision-induced reconnection layers can already generate large-scale mini-jets in the bulk jet of a GRB, which would give interesting variability features in the light curves.

Finally, our simulations show significant evolution of the magnetic field configuration during one ICMART event. From Figure 35, we can see that during the early collision-driven reconnection phase (e.g. the "plateau" phase), the strengths of B_x and B_y components decrease, which significantly changes the magnetic field config-

uration while still keeping a relative ordered magnetic configuration in a relatively short time duration. The behavior may potentially interpret the significant change of the polarization angle during the prompt emission phase observed in GRB 100826A (Yonetoku et al., 2011).

3.6.2 AGNs

Some blazars show very fast TeV flares whose durations are only several minutes (Aharonian et al., 2007; Albert et al., 2007). This duration is much shorter than the light crossing time for the entire system, which means that emission comes from a small local region. The requirement of emitting TeV photons also demand a much larger Lorentz factor in the emission region (greater than 50, Begelman et al. 2008; Mastichiadis & Moraitis 2008) than what is inferred for the bulk motion (typically smaller than 10, Giroletti et al. 2004; Piner & Edwards 2004). A successful model to interpret the observations is the "jets in a jet" model proposed by Giannios et al. (2009). This model invokes current-instability triggered local magnetic reconnections in a global, Poynting-flux-dominated jet. These local reconnections generate local outflows or mini-jets with a comoving Lorentz factor around a few. Our simulations give an alternative process to trigger the local reconnections by considering ICMART events, i.e. collisions among magnetic knots/blobs inside the global jet. Since the knots in AGNs have already been observed (Marscher et al., 2002; Chatterjee et al., 2009; Doi et al., 2011), the collisions would very likely happen, which trigger the local reconnections and generate the mini-jets as needed in their model.

We can also roughly estimate the time scale using our simulation results and the parameters in the model of Giannios et al. (2009). They estimated that the typical size of the blob in the rest frame of the blob is around 10^{14}cm. Since the Lorentz factor of the blob in the comoving frame of the global jet is equal to 10 (assuming $\sigma = 100$), the size of the global jet in the comoving frame is about 10^{13}cm, which

can be treated as L_0 in our Table 1. Thus one time unit in our simulations can be normalized as $t_0 = L_0/c \sim 3 \times 10^2$s. The duration of the reconnection-facilitated energy dissipation is about 50 time units in our example case (see Figure 29 from t=30 to t=80), which can be translated to about 10^4s in the rest frame of the global jet. The duration in the observer frame is $\sim 10^4\text{s}/\Gamma_j \sim 10^4\text{s}/10 = 10^3$s, which is very close to the observed durations of the flares.

Appendix

The following is the expanded full expression of Eq.(2.35).

Plugging in $P(\nu,T)$, $\hat{P}(r,\Omega)$ in Equation (2.35), one gets

$$\begin{aligned}
\hat{F}_\nu(\nu,t,\hat{t}) &= \frac{\dot{N}_0}{4\pi d_{\rm L}^2}\int\int \hat{P}(r,\Omega)\cdot\frac{n_\gamma(\nu,T)}{16\pi(\frac{kT}{hc})^3\cdot\zeta(3)}\cdot h\nu \\
&\quad\cdot\delta\left(t-\hat{t}-(\frac{ru}{\beta c}-t_0)\right)d\Omega dr \\
&= \frac{\dot{N}_0}{4\pi d_{\rm L}^2}\int_{\rm r_{min}}^{\rm r_{max}}\int\int_0^{2\pi}\frac{\sigma_{\rm T}n'\Gamma\frac{\mathcal{D}^2}{4\pi}e^{-\tau({\rm r},\mu,{\rm r_{out}})}}{A}\cdot\frac{n_\gamma(\nu,T)}{16\pi(\frac{kT}{hc})^3\cdot\zeta(3)}\cdot h\nu \\
&\quad\cdot\delta\left(t-\hat{t}-(\frac{ru}{\beta c}-t_0)\right)d(-\mu)d\phi dr \\
&= \frac{\dot{N}_0}{4\pi d_{\rm L}^2}\int_{\rm r_{min}}^{\rm r_{max}}\int\frac{\sigma_{\rm T}n'\Gamma\frac{\mathcal{D}^2}{2}e^{-\tau({\rm r},\mu,{\rm r_{out}})}}{A}\cdot\frac{n_\gamma(\nu,T)}{16\pi(\frac{kT}{hc})^3\cdot\zeta(3)}\cdot h\nu \\
&\quad\cdot\delta\left(t-\hat{t}-(\frac{ru}{\beta c}-t_0)\right)d(-\mu)dr \\
&= \frac{\dot{N}_0}{4\pi d_{\rm L}^2}\int_{\rm r_{min}}^{\rm r_{max}}\int\frac{\sigma_{\rm T}n'\Gamma\frac{1}{2\beta(\Gamma u)^2}e^{-\tau({\rm r},\mu,{\rm r_{out}})}}{A}\cdot\frac{\frac{8\pi\nu^2}{c^3}\frac{1}{\exp(\frac{h\nu}{kT})-1}}{16\pi(\frac{kT}{hc})^3\cdot\zeta(3)}\cdot h\nu \\
&\quad\cdot\delta\left(u-\frac{\beta c(t-\hat{t}+t_0)}{r}\right)\frac{\beta c}{r}dudr \qquad (u=1-\beta\mu) \\
&= \frac{\dot{N}_0}{4\pi d_{\rm L}^2}\int_{\rm r_{min}}^{\rm r_{max}}\int\frac{\sigma_{\rm T}n'\Gamma\frac{1}{2\beta(\Gamma u)^2}e^{-\tau({\rm r},\mu,{\rm r_{out}})}}{A}\cdot\frac{\frac{8\pi\nu^2}{c^3}(\exp(\frac{h\nu\Gamma u}{kT'})-1)^{-1}}{16\pi(\frac{kT'}{hc\Gamma u})^3\cdot\zeta(3)}\cdot h\nu \\
&\quad\cdot\delta\left(u-\frac{\beta c(t-\hat{t}+t_0)}{r}\right)\frac{\beta c}{r}dudr \qquad (T=\frac{T'}{\Gamma u}) \\
&= \frac{\dot{N}_0}{4\pi d_{\rm L}^2}\int_{\rm r_{min}}^{\rm r_{max}}\frac{\sigma_{\rm T}n'\Gamma\frac{r^2}{2\beta(\Gamma\beta c(t-\hat{t}+t_0))^2}e^{-\tau({\rm r},\mu,{\rm r_{out}})}}{A}\cdot\frac{\frac{2\nu^2}{c^3}(\exp(\frac{h\nu\Gamma\beta c(t-\hat{t}+t_0)}{kT'r})-1)^{-1}}{4(\frac{kT'r}{hc\Gamma\beta c(t-\hat{t}+t_0)})^3\cdot\zeta(3)}\cdot h\nu\frac{\beta c}{r}dr.
\end{aligned} \tag{3.24}$$

The limits of integration can be calculated from the formula of equal arrival time surface, $t-\hat{t}=\frac{ru}{\beta c}$, i.e. $r=\frac{\beta c(t-\hat{t})}{u}$. With $\theta_{\rm min}=0$ and $\theta_{\rm max}=\pi/2$, we get $r_{\rm min}=\max[\beta c(t-\hat{t}),r_0]$ and $r_{\rm max}=\max[\frac{\beta c(t-\hat{t})}{1-\beta},r_0]=\max[\Gamma^2(1+\beta)\beta c(t-\hat{t}),r_0]$.

REFERENCES

Abbasi, R., Abdou, Y., Abu-Zayyad, T., et al. 2012, Nature, 484, 351

Abdo, A. A., Ackermann, M., Arimoto, M., et al. 2009a, Science, 323, 1688

Abdo, A. A., Ackermann, M., Ajello, M., Asano, K., Atwood, W. B., Axelsson, M., Baldini, L., Ballet, J., Barbiellini, G., Baring, M. G., et al., Nov. 2009b. Fermi Observations of GRB 090902B: A Distinct Spectral Component in the Prompt and Delayed Emission. ApJ706, L138–L144.

Abdo, A. A., Ackermann, M., Ajello, M., Asano, K., Atwood, W. B., Axelsson, M., Baldini, L., Ballet, J., Barbiellini, G., Baring, M. G., et al., Nov. 2009c. A limit on the variation of the speed of light arising from quantum gravity effects. Nature462, 331–334.

Abramowicz, M. A., Novikov, I. D., & Paczynski, B. 1991, ApJ, 369, 175

Ackermann, M., Ajello, M., Asano, K., et al. 2011, ApJ, 729, 114

Ackermann, M., Asano, K., Atwood, W. B., Axelsson, M., Baldini, L., Ballet, J., Barbiellini, G., Baring, M. G., Bastieri, D., Bechtol, K., et al., Jun. 2010. Fermi Observations of GRB 090510: A Short-Hard Gamma-ray Burst with an Additional, Hard Power-law Component from 10 keV TO GeV Energies. ApJ716, 1178–1190.

Aharonian, F., Akhperjanian, A. G., Bazer-Bachi, A. R., et al. 2007, ApJ, 664, L71

Albert, J., Aliu, E., Anderhub, H., et al. 2007, ApJ, 669, 862

Asano, K., & Terasawa, T. 2009, ApJ, 705, 1714

Asano, K., & Mészáros, P. 2013, JCAP, 9, 8

Axelsson, M., Baldini, L., Barbiellini, G., et al. 2012, ApJ, 757, L31

Balsara, D. S., & Spicer, D. S. 1999, Journal of Computational Physics, 149, 270

Band, D., Matteson, J., Ford, L., et al. 1993, ApJ, 413, 281

Begelman, M. C., Fabian, A. C., & Rees, M. J. 2008, MNRAS, 384, L19

Beloborodov, A. M., Aug. 2000. On the Efficiency of Internal Shocks in Gamma-Ray Bursts. ApJ539, L25–L28.

Beloborodov, A. M. 2010, MNRAS, 407, 1033

—. 2011, ApJ, 737, 68

Beloborodov, A. M., Feb. 2013. Regulation of the Spectral Peak in Gamma-Ray Bursts. ApJ764, 157.

Beloborodov, A. M., Stern, B. E., & Svensson, R. 1998, ApJ, 508, L25

Blandford, R. D., McKee, C. F., Aug. 1976. Fluid dynamics of relativistic blast waves. Physics of Fluids 19, 1130–1138.

Bošnjak, Ž., Daigne, F., Dubus, G., May 2009. Prompt high-energy emission from gamma-ray bursts in the internal shock model. A&A498, 677–703.

Bošnjak, Ž., Götz, D., Bouchet, L., Schanne, S., Cordier, B., Sep. 2013. The spectral catalogue of INTEGRAL gamma-ray bursts: results of the joint IBIS/SPI spectral analysis. ArXiv e-prints.

Bošnjak, Ž., Götz, D., Bouchet, L., Schanne, S., & Cordier, B. 2014, A&A, 561, A25

Briggs, M. S., Band, D. L., Kippen, R. M., Preece, R. D., Kouveliotou, C., van Paradijs, J., Share, G. H., Murphy, R. J., Matz, S. M., Connors, A., Winkler, C., McConnell, M. L., Ryan, J. M., Williams, O. R., Young, C. A., Dingus, B., Catelli, J. R., Wijers, R. A. M. J., Oct. 1999. Observations of GRB 990123 by the Compton Gamma Ray Observatory. ApJ524, 82–91.

Burgess, J. M., Preece, R. D., Baring, M. G., et al. 2011, ApJ, 741, 24

Bykov, A. M., Mészáros, P. 1996, ApJ, 461, L37

Campana, S., Mangano, V., Blustin, A. J., Brown, P., Burrows, D. N., Chincarini, G., Cummings, J. R., Cusumano, G., Della Valle, M., Malesani, D., Mészáros, P., Nousek, J. A., Page, M., Sakamoto, T., Waxman, E., Zhang, B., Dai, Z. G., Gehrels, N., Immler, S., Marshall, F. E., Mason, K. O., Moretti, A., O'Brien, P. T., Osborne, J. P., Page, K. L., Romano, P., Roming, P. W. A., Tagliaferri, G., Cominsky, L. R., Giommi, P., Godet, O., Kennea, J. A., Krimm, H., Angelini, L., Barthelmy, S. D., Boyd, P. T., Palmer, D. M., Wells, A. A., White, N. E., Aug. 2006. The association of GRB 060218 with a supernova and the evolution of the shock wave. Nature442, 1008–1010.

Chatterjee, R. et al. 2009, ApJ, 704, 1689

Coburn, W., Boggs, S. E., May 2003. Polarization of the prompt γ-ray emission from the γ-ray burst of 6 December 2002. Nature423, 415–417.

Colella, P., & Woodward, P. R. 1984, Journal of Computational Physics, 54, 174

Costa, E., Frontera, F., Heise, J., Feroci, M., in't Zand, J., Fiore, F., Cinti, M. N., Dal Fiume, D., Nicastro, L., Orlandini, M., Palazzi, E., Rapisarda#, M., Zavattini, G., Jager, R., Parmar, A., Owens, A., Molendi, S., Cusumano, G., Maccarone, M. C., Giarrusso, S., Coletta, A., Antonelli, L. A., Giommi, P., Muller, J. M., Piro, L., Butler, R. C., Jun. 1997. Discovery of an X-ray afterglow associated with the γ-ray burst of 28 February 1997. Nature387, 783–785.

Daigne, F., Bošnjak, Ž., & Dubus, G. 2011, A&A, 526, A110

Daigne, F., & Mochkovitch, R. 1998, MNRAS, 296, 275

Daughton, W., & Karimabadi, H. 2007, Physics of Plasmas, 14, 072303

Deng, W., & Zhang, B. 2014, ApJ, 785, 112

Deng, W., Li, H., Zhang, B., & Li, S. 2015, arXiv:1501.07595

Doi, A. et al. 2011, arXiv:1106.2930

Fan, Y., Piran, T., Jun. 2006b. Gamma-ray burst efficiency and possible physical processes shaping the early afterglow. MNRAS369, 197–206.

Fender, R., & Belloni, T. M., 2004, ARA&A, 42, 317

Fishman, G. J., Meegan, C. A., 1995. Gamma-Ray Bursts. Annual Review of Astronomy and Astrophysics33, 415–458.

Ford, L. A., Band, D. L., Matteson, J. L., et al. 1995, ApJ, 439, 307

Frail, D. A., Kulkarni, S. R., Nicastro, L., Feroci, M., Taylor, G. B., Sep. 1997. The radio afterglow from the γ-ray burst of 8 May 1997. Nature389, 261–263.

Frontera, F., Amati, L., Farinelli, R., Dichiara, S., Guidorzi, C., Landi, R., Titarchuk, L., Nov. 2013. Comptonization signatures in the prompt emission of Gamma Ray Bursts. ArXiv e-prints.

Gao, H., Lei, W.-H., Zou, Y.-C., Wu, X.-F., Zhang, B., Dec. 2013b. A complete reference of the analytical synchrotron external shock models of gamma-ray bursts. New Astron. Rev.57, 141–190.

Gao, H., & Mészáros, P. 2015, ApJ, 802, 90

Gao, H., & Zhang, B. 2015, ApJ, 801, 103

Gao, H., Zhang, B.-B., Zhang, B. 2012, ApJ, 748, 134

Ghirlanda, G., Celotti, A., & Ghisellini, G. 2002, A&A, 393, 409

Ghirlanda, G., Celotti, A., & Ghisellini, G. 2003, A&A, 406, 879

Ghirlanda, G., Bosnjak, Z., Ghisellini, G., Tavecchio, F., & Firmani, C. 2007, MNRAS, 379, 73

Ghirlanda, G., Nava, L., & Ghisellini, G. 2010, A&A, 511, A43

Ghirlanda, G., Ghisellini, G., Nava, L., & Burlon, D. 2011, MNRAS, 410, L47

Ghirlanda, G., Ghisellini, G., & Nava, L. 2011, MNRAS, 418, L109

Ghirlanda, G., Pescalli, A., & Ghisellini, G. 2013, MNRAS, 432, 3237

Ghisellini, G., & Celotti, A. 1999, ApJ, 511, L93

Ghisellini, G., Celotti, A., & Lazzati, D. 2000, MNRAS, 313, L1.

Ghisellini, G., Ghirlanda, G., Nava, L., Celotti, A., Apr. 2010. GeV emission from gamma-ray bursts: a radiative fireball? MNRAS403, 926–937.

Giannios, D. 2008, A&A, 480, 305

Giannios, D., Uzdensky, D. A., & Begelman, M. C. 2009, MNRAS, 395, L29

Giroletti, M., Giovannini, G., Feretti, L., et al. 2004, ApJ, 600, 127

Golenetskii, S. V., Mazets, E. P., Aptekar, R. L., Ilinskii, V. N., Dec. 1983. Correlation between luminosity and temperature in gamma-ray burst sources. Nature306, 451–453.

Granot, J., Komissarov, S. S., Spitkovsky, A., Feb. 2011. Impulsive acceleration of strongly magnetized relativistic flows. MNRAS411, 1323–1353.

Gruber, D., Goldstein, A., Weller von Ahlefeld, V., et al. 2014, ApJ, 211, 12

Guan, X., Li, H., & Li, S. 2014, ApJ, 781, 48

Guidorzi, C., Margutti, R., Amati, L., et al. 2012, MNRAS, 422, 1785

Guiriec, S., Connaughton, V., Briggs, M. S., et al. 2011, ApJ, 727, LL33

Guiriec, S., Daigne, F., Hascoët, R., et al. 2013, ApJ, 770, 32

Guo, F., Li, H., Daughton, W., & Liu, Y.-H. 2014, Physical Review Letters, 113, 155005

Hakkila, J., & Preece, R. D. 2011, ApJ, 740, 104

Hjellming, R. M. & Rupen, M. P. 1995, Nat, 375, 464

Ioka, K. 2010, Progress of Theoretical Physics, 124, 667

Kalemci, E., Boggs, S. E., Kouveliotou, C., Finger, M., Baring, M. G., Mar. 2007. Search for Polarization from the Prompt Gamma-Ray Emission of GRB 041219a with SPI on INTEGRAL. ApJ169, 75–82.

Klebesadel, R. W., Strong, I. B., Olson, R. A., Jun. 1973. Observations of Gamma-Ray Bursts of Cosmic Origin. ApJ182, L85.

Kobayashi, S., Piran, T., Sari, R., Nov. 1997. Can Internal Shocks Produce the Variability in Gamma-Ray Bursts? ApJ490, 92–+.

Kobayashi, S., Piran, T., & Sari, R. 1999, ApJ, 513, 669

Kobayashi, S., Sari, R., Apr. 2001. Ultraefficient Internal Shocks. ApJ551, 934–939.

Kouveliotou, C., Meegan, C. A., Fishman, G. J., Bhat, N. P., Briggs, M. S., Koshut, T. M., Paciesas, W. S., Pendleton, G. N., Aug. 1993. Identification of two classes of gamma-ray bursts. ApJ413, L101–L104.

Krimm, H. A., Granot, J., Marshall, F. E., et al. 2007, ApJ, 665, 554

Kumar, P. 1999, ApJ, 523, L113.

Kumar, P., Barniol Duran, R., Nov. 2009. On the generation of high-energy photons detected by the Fermi Satellite from gamma-ray bursts. MNRAS400, L75–L79.

Kumar, P., & Narayan, R. 2009, MNRAS, 395, 472

Kumar, P., & Panaitescu, A. 2008, MNRAS, 391, L19

Kumar, P., & Zhang, B. 2013, Phys. Rep., submitted

Kumar, P., & Zhang, B. 2014, arXiv:1410.0679

Lazzati, D., & Begelman, M. C. 2010, ApJ, 725, 1137

Lazzati, D., Morsony, B. J., Begelman, M. C., Jul. 2009. Very High Efficiency Photospheric Emission in Long-Duration γ-Ray Bursts. ApJ700, L47–L50.

Lazzati, D., Morsony, B. J., Margutti, R., & Begelman, M. C. 2013, ApJ, 765, 103

Lei, W.-H., Zhang, B., & Liang, E.-W. 2013, ApJ, 765, 125

Li, H., Lapenta, G., Finn, J. M., Li, S., & Colgate, S. A. 2006, ApJ, 643, 92

Li, L.-X. 2000, ApJ, 531, L111

Li, S.,& Li,H., 2003, Los Alamos National Lab. Tech. Rep. LA-UR-03-8935

Li, C., & Sari, R. 2008, ApJ, 677, 425

Liang, E., & Kargatis, V. 1996, Nature, 381, 49

Liang, E.-W., Yi, S.-X., Zhang, J., et al. 2010, ApJ, 725, 2209

Liang, E. W., Zhang, B., O'Brien, P. T., Willingale, R., Angelini, L., Burrows, D. N., Campana, S., Chincarini, G., Falcone, A., Gehrels, N., Goad, M. R., Grupe, D., Kobayashi, S., Mészáros, P., Nousek, J. A., Osborne, J. P., Page, K. L., Tagliaferri, G., Jul. 2006a. Testing the Curvature Effect and Internal Origin of Gamma-Ray Burst Prompt Emissions and X-Ray Flares with Swift Data. ApJ646, 351–357.

Lloyd, N. M., & Petrosian, V. 2000, ApJ, 543, 722

Lü, J., Zou, Y.-C., Lei, W.-H., et al. 2012, ApJ, 751, 49

Lu, R.-J., Hou, S.-J., & Liang, E.-W. 2010, ApJ, 720, 1146

Lu, R.-J., Wei, J.-J., Liang, E.-W., et al. 2012, ApJ, 756, 112

Lundman, C., Pe'er, A., & Ryde, F. 2013, MNRAS, 428, 2430

Lyutikov, M., & Blandford, R. 2003, arXiv:astro-ph/0312347

Marscher, A. P. et al. 2002, Nat, 417, 625

Mastichiadis, A., & Moraitis, K. 2008, A&A, 491, L37

Maxham, A., & Zhang, B. 2009, ApJ, 707, 1623

McGlynn, S., Clark, D. J., Dean, A. J., Hanlon, L., McBreen, S., Willis, D. R., McBreen, B., Bird, A. J., Foley, S., May 2007. Polarisation studies of the prompt gamma-ray emission from GRB 041219a using the spectrometer aboard INTEGRAL. A&A466, 895–904.

McKinney, J. C., Uzdensky, D. A., Jan. 2012. A reconnection switch to trigger gamma-ray burst jet dissipation. MNRAS419, 573–607.

Mészáros, P., Laguna, P., & Rees, M. J. 1993, ApJ, 415, 181

Mészáros, P., Ramirez-ruiz, E., Rees, M. J., & Zhang, B. 2002, ApJ, 578, 812

Mészáros, P., Rees, M. J., Feb. 1997a. Optical and Long-Wavelength Afterglow from Gamma-Ray Bursts. ApJ476, 232.

Mészáros, P., Rees, M. J. & Wijers, R. A. M. J. 1998, ApJ, 499, 301

Mészáros, P., & Rees, M. J. 2000, ApJ, 530, 292

Mészáros, P., Rees, M. J., & Papathanassiou, H. 1994, ApJ, 432, 181

Mirabel, I. F., Rodriguez, L. F. 1994, Nature, 371, 46

Mizuno, Y., Lyubarsky, Y., Nishikawa, K.-I., Hardee, P. E. 2009, ApJ, 700, 684

Mizuta, A., Nagataki, S., Aoi, J. 2011, ApJ, 732, 26

Mundell, C. G., Kopač, D., Arnold, D. M., et al. 2013, Nature, 504, 119

Narayan, R., & Kumar, P. 2009, MNRAS, 394, L117

Nava, L., Ghirlanda, G., Ghisellini, G., & Celotti, A. 2011, A&A, 530, A21

Norris, J. P., Nov. 2002. Implications of the Lag-Luminosity Relationship for Unified Gamma-Ray Burst Paradigms. ApJ579, 386–403.

Norris, J. P., Bonnell, J. T., Kazanas, D., Scargle, J. D., Hakkila, J., Giblin, T. W., Jul. 2005. Long-Lag, Wide-Pulse Gamma-Ray Bursts. ApJ627, 324–345.

Norris, J. P., Marani, G. F., Bonnell, J. T., May 2000. Connection between Energy-dependent Lags and Peak Luminosity in Gamma-Ray Bursts. ApJ534, 248–257.

Norris, J. P., Share, G. H., Messina, D. C., Dennis, B. R., Desai, U. D., Cline, T. L., Matz, S. M., Chupp, E. L., Feb. 1986. Spectral evolution of pulse structures in gamma-ray bursts. ApJ301, 213–219.

Paczýnski, B., & Xu, G. 1994, ApJ, 427, 708.

Page, K. L., Willingale, R., Osborne, J. P., Zhang, B., Godet, O., Marshall, F. E., Melandri, A., Norris, J. P., O'Brien, P. T., Pal'shin, V., Rol, E., Romano, P., Starling, R. L. C., Schady, P., Yost, S. A., Barthelmy, S. D., Beardmore, A. P., Cusumano, G., Burrows, D. N., De Pasquale, M., Ehle, M., Evans, P. A., Gehrels, N., Goad, M. R., Golenetskii, S., Guidorzi, C., Mundell, C., Page, M. J., Ricker, G., Sakamoto, T., Schaefer, B. E., Stamatikos, M., Troja, E., Ulanov, M., Yuan, F., Ziaeepour, H., Jul. 2007. GRB 061121: Broadband Spectral Evolution through the Prompt and Afterglow Phases of a Bright Burst. ApJ663, 1125–1138.

Panaitescu, A., & Kumar, P. 2002, ApJ, 571, 779

Panaitescu, A., Spada, M., & Mészáros, P. 1999, ApJ, 522, L105.

Pe'er, A. 2008, ApJ, 682, 463

Pe'er, A., Mészáros, P., & Rees, M. J. 2006, ApJ, 642, 995

Pe'er, A., & Ryde, F. 2011, ApJ, 732, 49

Pe'er, A., & Zhang, B. 2006, ApJ, 653, 454

Pe'er, A., Zhang, B.-B., Ryde, F., McGlynn, S., Zhang, B., Preece, R. D., Kouveliotou, C. 2012, MNRAS, 420, 468

Piner, B. G., & Edwards, P. G. 2004, ApJ, 600, 115

Piran, T., Shemi, A., & Narayan, R. 1993, MNRAS, 263, 861

Preece, R. D., Briggs, M. S., Mallozzi, R. S., et al. 2000, ApJ, 126, 19

Rees, M. J., & Mészáros, P. 1994, ApJ, 430, L93.

Rees, M. J., & Mészáros, P. 2005, ApJ, 628, 847

Romano, P., Moretti, A., Banat, P. L., Burrows, D. N., Campana, S., Chincarini, G., Covino, S., Malesani, D., Tagliaferri, G., Kobayashi, S., Zhang, B., Falcone, A. D., Angelini, L., Barthelmy, S., Beardmore, A. P., Capalbi, M., Cusumano, G., Giommi, P., Goad, M. R., Godet, O., Grupe, D., Hill, J. E., Kennea, J. A., La Parola, V., Mangano, V., Mészáros, P., Morris, D. C., Nousek, J. A., O'Brien, P. T., Osborne, J. P., Parsons, A., Perri, M., Pagani, C., Page, K. L., Wells, A. A., Gehrels, N., Apr. 2006. X-ray flare in XRF 050406: evidence for prolonged engine activity. A&A450, 59–68.

Rossi, E., Lazzati, D., & Rees, M. J. 2002, MNRAS, 332, 945

Ruffini, R., Siutsou, I. A., & Vereshchagin, G. V. 2013, ApJ, 772, 11

Rutledge, R. E., Fox, D. B., Jun. 2004. Re-analysis of polarization in the γ-ray flux of GRB 021206. MNRAS350, 1288–1300.

Ryde, F. 2005, ApJ, 625, L95

Ryde, F., & Pe'er, A. 2009, ApJ, 702, 1211

Ryde, F., Axelsson, M., Zhang, B. B., et al. 2010, ApJ, 709, L172

Sari, R., Piran, T., Narayan, R., Apr. 1998. Spectra and Light Curves of Gamma-Ray Burst Afterglows. ApJ497, L17+.

Shemi, A., Piran, T., Dec. 1990. The appearance of cosmic fireballs. ApJ365, L55–L58.

Shen, R., & Zhang, B. 2009, MNRAS, 398, 1936.

Sironi, L., & Spitkovsky, A. 2014, ApJ, 783, L21

Steele, I. A., Mundell, C. G., Smith, R. J., Kobayashi, S., & Guidorzi, C. 2009, Nature, 462, 767

Tavani, M. 1996, ApJ, 466, 768

Thompson, C. 1994, MNRAS, 270, 480

Thompson, C., Mészáros, P., & Rees, M. J. 2007, ApJ, 666, 1012

Thompson, C., & Gill, R. 2013, ApJ, submitted (arXiv:1310.2480)

Toma, K., Wu, X.-F., & Mészáros, P. 2011, MNRAS, 415, 1663

Uhm, Z. L., & Zhang, B. 2014, Nature Physics, 10, 351

van Paradijs, J., Groot, P. J., Galama, T., Kouveliotou, C., Strom, R. G., Telting, J., Rutten, R. G. M., Fishman, G. J., Meegan, C. A., Pettini, M., Tanvir, N., Bloom, J., Pedersen, H., Nørdgaard-Nielsen, H. U., Linden-Vørnle, M., Melnick, J., van der Steene, G., Bremer, M., Naber, R., Heise, J., in't Zand, J., Costa, E., Feroci, M., Piro, L., Frontera, F., Zavattini, G., Nicastro, L., Palazzi, E., Bennet, K., Hanlon, L., Parmar, A., Apr. 1997. Transient optical emission from the error box of the γ-ray burst of 28 February 1997. Nature386, 686–689.

Veres, P., Zhang, B.-B., & Mészáros, P. 2012, ApJ, 761, L18

Vurm, I., Beloborodov, A. M., & Poutanen, J. 2011, ApJ, 738, 77

Vurm, I., Lyubarsky, Y., & Piran, T. 2013, ApJ, 764, 143

Wang, X., Li, Z., Dai, Z., & Mészáros, P. 2009, ApJ, 698, L98

Willis, D. R., Barlow, E. J., Bird, A. J., Clark, D. J., Dean, A. J., McConnell, M. L., Moran, L., Shaw, S. E., Sguera, V., Aug. 2005. Evidence of polarisation in the prompt gamma-ray emission from GRB 930131 and GRB 960924. A&A439, 245–253.

Yonetoku, D., Murakami, T., Gunji, S., et al. 2011, ApJ, 743, LL30

Yonetoku, D., Murakami, T., Gunji, S., et al. 2012, ApJ, 758, LL1

Yuan, F., Lin, J., Wu, K., & Ho, L. 2009, MNRAS, 395, 2183

Yuan, F., & Zhang, B. 2012, ApJ, 757, 56

Yuan, Q., Yin, P.-F., Wu, X.-F., Bi, X., Liu, S. & Zhang, B. 2011, ApJ, 730, L15

Zhang, B. 2014, International Journal of Modern Physics D, 23, 1430002

Zhang, B. 2015, Cambridge University Press, in preparation

Zhang, B., Dai, X., Lloyd-Ronning, M., & Mészáros, P. 2004, ApJ, 601, L119

Zhang, B., Fan, Y. Z., Dyks, J., et al. 2006, ApJ, 642, 354

Zhang, B., & Kumar, P. 2013, Physical Review Letters, 110, 121101

Zhang, B., Liang, E., Page, K. L., et al. 2007, ApJ, 655, 989

Zhang, B., Lu, R.-J., Liang, E.-W., & Wu, X.-F. 2012, ApJ, 758, L34

Zhang, B., & Mészáros, P. 2002a, ApJ, 581, 1236

Zhang, B., & Mészáros, P. 2002b, ApJ, 571, 876

Zhang, B., & Pe'er, A. 2009, ApJ, 700, L65

Zhang, B., & Yan, H. 2011, ApJ, 726, 90

Zhang, B., & Zhang, B. 2014, ApJ, 782, 92

Zhang, B.-B., Zhang, B., Liang, E.-W., et al. 2011, ApJ, 730, 141

Zhang, J., Liang, E.-W., Sun, X.-N., et al. 2013, ApJ, 774, L5

Zhao, X. H., Li, Z., Liu, X. et al. 2014, ApJ, 780, 12

VITA

Graduate College
University of Nevada, Las Vegas

Wei Deng

Degrees:

Bachelor of Science, Atmospheric Science, 2007
Nanjing University

Master of Science, Astrophysics, 2010
Nanjing University

Publications:

[4] **Wei Deng**, Hui Li, Bing Zhang, Shengtai Li, *Relativistic MHD simulations of collision-induced magnetic dissipation in Poynting-flux-dominated jets/outflows*, The Astrophysical Journal, in press (arXiv:1501.07595).

[3] **Wei Deng**, Bing Zhang, *Low Energy Spectral Index and Ep Evolution of Quasi-thermal Photosphere Emission of Gamma-Ray Bursts*, The Astrophysical Journal 785,112, 2014

[2] **Wei Deng**, Bing Zhang, *Cosmological Implications of Fast Radio Burst/Gamma-Ray Burst Associations*, The Astrophysical Journal Letters 783,35, 2014

[1] **Wei Deng**, YongFeng Huang, SiWei Kong, *Measuring the beaming angle of GRB 030329 by fitting the rebrightenings in its multiband afterglow*, Research in Astronomy and Ast

Dissertation Title:

STUDY THE MECHANISM OF THE PROMPT EMISSION OF GAMMA-RAY BURSTS

Dissertation Examination Committee:

Chairperson, Bing Zhang, Ph.D.
Committee Member, Daniel Proga, Ph.D.
Committee Member, Stephen Lepp, Ph.D.
Graduate Faculty Representative, Pengtao Sun, Ph.D.